

Diss. ETH No. 23679

**CHARACTERIZATION OF
NONSTOICHIOMETRIC METAL OXIDES FOR
SOLAR THERMOCHEMICAL REDOX CYCLING**

A thesis submitted to attain the degree of
DOCTOR OF SCIENCES of ETH ZURICH

(Dr. sc. ETH Zurich)

presented by

MICHAEL TAKACS

MSc ETH ME

born on 30.03.1988

citizen of Goldach (SG)

accepted on the recommendation of

Prof. Dr. Aldo Steinfeld, examiner

Prof. Dr. Jonathan R. Scheffe, co-examiner

Dr. Martin Roeb, co-examiner

2016

Abstract

Solar-driven thermochemical redox cycles utilizing nonstoichiometric metal oxides are capable of splitting H_2O and CO_2 to produce H_2 and CO (syngas), the precursors to the catalytic synthesis of conventional liquid fuels. Ceria (CeO_2) is currently considered a state-of-the-art material because it displays rapid oxidation and reduction kinetics and is morphologically stable over a range of temperatures and reduction extents. Since the reduction extent of ceria is generally lower than those obtained by other appropriate redox materials (*e.g.* ferrite, zinc oxide), its specific fuel production per mass is low. This has a direct implication on efficiencies because they are largely dictated by the ratio of fuel produced to that of the thermal energy required to heat the oxide between oxidation and reduction steps. Therefore, one part of this thesis evaluates the potential of nonstoichiometric metal oxides exhibiting larger reduction extents compared to ceria to be used as reactive intermediates for solar H_2O and CO_2 splitting.

In the first part, a thermodynamic characterization and critical evaluation of Zr^{4+} doped ceria is shown. As a case study, 5 mol% Zr^{4+} doped ceria is examined and oxygen nonstoichiometry measurements are presented at elevated temperatures ranging from 1573 K to 1773 K and oxygen partial pressures ranging from 4.62×10^{-3} bar to 2.3×10^{-4} bar, yielding higher reduction extents compared to those of pure ceria under all conditions investigated, especially at the lower temperature range and at higher p_{O_2} . In

contrast to pure ceria, a simple ideal solution model accounting for the formation of isolated oxygen vacancies and localized electrons accurately describes the defect chemistry. Thermodynamic properties were determined, namely: partial molar enthalpy, entropy, and Gibbs free energy. In general, partial molar enthalpy and entropy values of Zr^{4+} doped ceria are lower. The equilibrium hydrogen yields were subsequently extracted as a function of the redox conditions for dopant concentrations as high as 20%. Although reduction extents increase greatly with dopant concentration, the oxidation of Zr^{4+} doped ceria is thermodynamically less favorable compared to pure ceria. This leads to substantially larger temperature swings between reduction and oxidation steps, ultimately resulting in lower theoretical solar energy conversion efficiencies compared to ceria under most conditions.

The thermodynamic study was then expanded to doped lanthanum manganite perovskites, namely $La_{0.6}A_{0.4}Mn_{1-y}Al_yO_3$ ($A = Ca, Sr$ and $y = 0, 0.4$). Oxygen nonstoichiometry measurements in the temperature range $T = 1573\text{ K} - 1773\text{ K}$ and oxygen partial pressure range $p_{O_2} = 4.5066 \times 10^{-2}\text{ bar} - 9.9 \times 10^{-5}\text{ bar}$ are presented. For a given T and p_{O_2} , oxygen nonstoichiometry was found to be higher when replacing the divalent dopant Sr in $La_{0.6}Sr_{0.4}MnO_3$ by the divalent Ca but also increases significantly when additionally doping 40 mol% Al to the Mn-site. $La_{0.6}Ca_{0.4}Mn_{0.6}Al_{0.4}O_3$ revealed the highest mass specific oxygen release, 0.290 mol O_2 per kg metal oxide at $T = 1773\text{ K}$ and $p_{O_2} = 2.360 \times 10^{-3}\text{ bar}$ and 0.039 mol kg^{-1} at $T = 1573\text{ K}$ and $p_{O_2} = 4.5066 \times 10^{-2}\text{ bar}$. It is shown that the chemical defect equilibrium of all four perovskites can be accurately described by the two simultaneous redox couples Mn^{4+}/Mn^{3+} and Mn^{3+}/Mn^{2+} . Partial molar enthalpy, entropy and Gibbs free energy were consequently extracted from the defect models. Partial molar enthalpy decreases with increasing oxygen nonstoichiometry for the Al-doped perovskites whereas the opposite trend is observed for the others. The enthalpy falls within the range 260 - 300 $kJ\ mol^{-1}$ for all the

perovskites investigated. Equilibrium hydrogen yields upon oxidation with H₂O were determined as a function of redox conditions. Although reduction extents of the perovskites are greater compared to CeO₂, oxidation with H₂O and CO₂ is thermodynamically less favorable. This leads to lower mass specific fuel productivity compared to CeO₂ under most conditions relevant for solar thermochemical cycles.

Thermochemical splitting of CO₂ via a ceria-based redox cycle was tested in a solar-driven thermogravimetric analyzer, in which the solid reactants are directly exposed to high-flux irradiation while their mass change is continuously monitored during the redox cycling. For enhanced heat and mass transport, reticulated porous ceramic (RPC) structures made of undoped, 10 and 20 mol% Zr⁴⁺ doped ceria were fabricated with single-scale porosity in the mm range and with dual-scale porosity containing additional pores within the struts in the μm range. The RPC samples, along with commercially available ceria fibers, were irradiated under a solar flux concentration ratio of 1280 suns and endothermally reduced in the temperature range 1200 K - 1950 K, while their exothermal re-oxidation with CO₂ to generate CO was performed in the range 950 K - 1400 K. The highest heating rate was measured for the ceria RPC with the largest pores (8 ppi) due to its lowest optical thickness and, hence, efficient volumetric radiative absorption, resulting in a lower requirement of solar radiative energy input. In contrast, the sample with 10 ppi exhibited a higher volume-specific oxygen release during reduction and, consequently, higher fuel yield per cycle because of its relatively higher sample density. As for the oxidation, the rates are faster for the RPC with dual-scale porosity, but the absolute CO yield is higher for the RPC with single-scale porosity because of the higher mass loading. Zr⁴⁺ doped ceria shows increasing reduction extents with increasing dopant concentration but could not surpass the

specific CO yield of pure ceria under the conditions investigated due to unfavorable oxidation thermodynamics and slower kinetics.

Long term chemical and morphological stability of reticulated porous ceramic (RPC) structures made of ceria (CeO_2) was tested in a fast heating infrared furnace setup. RPCs with single and dual-scale porosity were redox cycled for a varying number of times between reduction at temperatures $T = 1673$ and 1773 K and oxidation with H_2O at $T = 873$ K whereas heating and cooling rates were set to 600 K min^{-1} . It was found that cracks within ceria grains form within the first reduction at $T = 1773$ K due to chemical expansion of reduced ceria, resulting in relatively fast oxidation rates with H_2O due to the increased surface area. Over time, sintering of the cracks results in a decrease in surface area and hence slower H_2 production rates. A first cycling study with reduction at $T = 1773$ K showed that H_2 rates decreased by 75% and 50% over 100 cycles at $\delta = 0.02$ for the dual-scale RPC with small and large μm sized pores, respectively, whereas it decreased by 90% at $\delta = 0.025$ over 59 cycles for the single-scale RPC. When reducing at $T = 1673$ K, morphology and H_2 rates were rather constant. Long term cycling of a dual-scale RPC with small pores at reduction temperature > 1773 K revealed that H_2 production rate decreased by around 60% at $\delta = 0.031$ over the first 200 cycles but levels at $2 \text{ mL min}^{-1} \text{ g}^{-1}$. H_2 yield mirrors the decreasing H_2 rates whereas rather constant O_2 yield indicate chemical stability of the ceria RPC.

Zusammenfassung

Solar-thermochemische Redoxprozesse basierend auf nichtstöchiometrischen Metalloxiden können aus H_2O und CO_2 , H_2 und CO (Synthesegas) produzieren, die Ausgangsstoffe für die katalytische Synthese von konventionellen flüssigen Treibstoffen. Ceriumdioxid (CeO_2) wird zurzeit als das Standardmaterial betrachtet aufgrund der schnellen Oxidations- und Reduktionskinetik und der morphologischen Stabilität über einen Bereich von Temperaturen und Reduktionszuständen. Da der Reduktionszustand von Ceriumdioxid typischerweise kleiner ist als bei anderen geeigneten Metalloxiden (z.B. Eisenoxid, Zinkoxid), ist dessen Massenspezifische Treibstoffproduktivität relativ klein. Dies hat einen direkten Einfluss auf die Prozesseffizienz, da diese grösstenteils bestimmt wird durch das Verhältnis von produzierter Menge an Treibstoff und Menge an thermischer Energie die benötigt wird zum Heizen des Metalloxids zwischen Oxidations- und Reduktionsschritt. Deshalb untersucht ein Teil dieser Arbeit das Potential von nichtstöchiometrischen Metalloxiden, welche im Vergleich zu Ceriumdioxid grössere Reduktionszustände aufweisen, um als reaktive Zwischenprodukte für die solare Spaltung von H_2O und CO_2 eingesetzt zu werden.

Im ersten Teil wird die thermodynamische Charakterisierung und kritische Analyse von Zr^{4+} dotiertem Ceriumdioxid behandelt. Als Fallstudie wurde 5 mol% Zr^{4+} dotiertes Ceriumdioxid untersucht. Sauerstoffnonstöchiometrie-

messungen werden bei erhöhten Temperaturen im Bereich 1573 K zu 1773 K und Sauerstoffpartialdrücken von 4.56×10^{-3} bar bis 2.3×10^{-4} bar präsentiert. Zr^{4+} dotiertes Ceriumdioxid besitzt grössere Reduktionszustände über den gesamten gemessenen Temperatur- und p_{O_2} -Bereich im Vergleich zu undotiertem Ceriumdioxid, aber vor allem in Richtung tieferer Temperaturen und höherem p_{O_2} . Es wird gezeigt, dass ein einfaches Defektmodell, welches die Formation von isolierten Sauerstoffleerstellen und lokalisierten Elektronen berücksichtigt, die Defektchemie von Zr^{4+} dotiertem Ceriumdioxid genau beschreiben kann, jedoch aber nicht die von undotiertem Ceriumdioxid. Thermodynamische Eigenschaften wurden bestimmt. Dies sind namentlich: partielle molare Enthalpie, Entropie und Gibbs freie Energie. Im Allgemeinen ist der Betrag der partiellen molaren Enthalpie und Entropie von Zr^{4+} dotiertem Ceriumdioxid kleiner. Die Wasserstoffproduktivität im chemischen Gleichgewicht wurde aufgrund der thermodynamischen Eigenschaften und als Funktion der Redoxbedingungen für Dotierungskonzentrationen von bis zu 20% bestimmt. Obwohl der Reduktionszustand stark zunimmt mit steigender Dotierungskonzentration, nimmt das thermodynamische Oxidationspotential von Zr^{4+} dotiertem im Vergleich zu undotiertem Ceriumdioxid ab. Dies führt zu einem signifikant grösseren Temperaturunterschied zwischen Reduktions- und Oxidationsschritt, was folglich zu einer tieferen theoretischen Solarenergieumwandlungseffizienz im Vergleich zu undotiertem Ceriumdioxid führt. Dies ist der Fall für die meisten relevanten Prozessbedingungen.

Die thermodynamische Studie wurde dann erweitert zu dotierten Lanthanmanganiten; namentlich $La_{0.6}A_{0.4}Mn_{1-y}Al_yO_3$ ($A = Ca, Sr$ und $y = 0, 0.4$). Sauerstoffnonstöchiometriemessungen im Temperaturbereich $T = 1573$ K - 1773 K und Sauerstoffpartialdruckbereich $p_{O_2} = 4.5066 \times 10^{-2}$ bar - 9.9×10^{-5} bar werden gezeigt. Bei gegebener Temperatur und gegebenem p_{O_2}

ist die Sauerstoffnonstöchiometrie grösser wenn das divalente Dotierungsmaterial Sr in $\text{La}_{0.6}\text{Sr}_{0.4}\text{MnO}_3$ ausgetauscht wird durch divalentes Ca. Diese wird aber zudem signifikant vergrössert wenn zusätzlich 40 mol% Al auf die Mn-Seite dotiert wird. $\text{La}_{0.6}\text{Ca}_{0.4}\text{Mn}_{0.6}\text{Al}_{0.4}\text{O}_3$ weist die grösste massenspezifische Sauerstofffreisetzung auf: 0.290 mol O_2 pro kg Metalloxid bei $T = 1773$ K und $p_{\text{O}_2} = 2.360 \times 10^{-3}$ bar und 0.039 mol kg^{-1} bei $T = 1573$ K und $p_{\text{O}_2} = 4.5066 \times 10^{-2}$ bar. Es wird gezeigt, dass das chemische Defektgleichgewicht aller vier Perovskite durch die simultanen Redoxpaare $\text{Mn}^{4+}/\text{Mn}^{3+}$ und $\text{Mn}^{3+}/\text{Mn}^{2+}$ beschrieben werden kann. Partielle molare Enthalpie, Entropie und Gibbs freie Energie wurden aufgrund der Defektmodelle bestimmt. Der Betrag der partiellen molaren Enthalpie nimmt ab mit steigender Sauerstoffnonstöchiometrie für die Al dotierten Perovskite, wobei der gegenläufige Trend beobachtet wurde für die anderen. Die Enthalpie fällt in den Bereich 260 - 300 kJ mol^{-1} für all die untersuchten Perovskite. Wasserstoffproduktivität im chemischen Gleichgewicht aufgrund der Oxidation mit H_2O wurden bestimmt als Funktion der Redoxbedingungen. Obwohl die Reduktionszustände der Perovskite grösser sind im Vergleich zu Ceriumdioxid, ist dessen Oxidation mit H_2O und CO_2 thermodynamisch weniger favorisiert. Dies führt zu einer geringerer massenspezifischer Treibstoffproduktivität im Vergleich zu Ceriumdioxid unter den meisten relevanten Bedingungen für Solarthermochemische Zyklen.

Die thermochemische Spaltung von CO_2 wurde experimentell getestet in einem solarbetriebenen Thermogravimeter, wo die Reaktanden direkt mit konzentrierter Strahlung bestrahlt werden und ihr Gewicht kontinuierlich aufgezeichnet wird während den Redoxzyklen. Aufgrund des guten Wärme- und Massetransports wurden netzartige, poröse Keramikstrukturen (RPCs) aus undotiertem, 10 und 20 mol% Zr^{4+} dotiertem Ceriumdioxid gefertigt, welche Poren im mm-Bereich besitzen aber auch zusätzlich Poren im μm -

Bereich innerhalb der Netzstreben. Die RPC-Proben und kommerziell erhältliche Faserstrukturen aus Ceriumdioxid wurden mit einer simulierten konzentrierten Solarstrahlung von 1280 Sonnen bestrahlt und endothermisch reduziert in Ar bei Temperaturen im Bereich 1200 K – 1950 K. Die exotherme Rückoxidation mit CO₂ folgte im Temperaturbereich 950 – 1400 K um CO zu produzieren. Die höchste Heizrate wurde gemessen für den Ceriumdioxid–RPC mit den grössten Poren (8 Poren pro Zoll). Dies aufgrund seiner tiefen optischen Dichte und deshalb effizienter volumetrischer Absorption von Strahlung, was zu einer tieferen solaren Strahlungszufuhr führt. Jedoch besitzt die Probe mit 10 Poren pro Zoll eine höhere volumenspezifische Sauerstofffreisetzung während der Reduktion und somit eine höhere Treibstoffproduktion pro Zyklus aufgrund ihrer höheren Probendichte. Die Oxidationsraten sind schneller für die RPC-Strukturen mit Poren im mm- und μm -Bereich im Vergleich mit den Strukturen welche nur Poren im mm-Bereich besitzen. Jedoch ist die absolute CO Produktivität des RPCs mit Poren nur im mm-Bereich grösser aufgrund der grösseren Masse. Zr⁴⁺ dotiertes Ceriumdioxid weist ansteigende Reduktionszustände mit steigender Dotierungskonzentration auf, kann aber die spezifische CO-Produktivität von undotiertem Ceriumdioxid nicht übertreffen innerhalb der untersuchten Bedingungen. Der Grund sind ungünstigere Oxidationsthermodynamik und langsamere Reaktionskinetik.

Die chemische und morphologische Langzeitstabilität von RPC-Strukturen aus Ceriumdioxid wurde in einem schnell heizenden Infrarotofen getestet. RPCs mit ein- und zweistufiger Porosität wurden mehrmals reduziert und oxidiert wobei die Reduktion bei Temperaturen von $T = 1673$ und 1773 K und die Oxidation mit H₂O bei $T = 873$ K ablief. Die Heiz- und Kühlrate wurde auf 600 K min^{-1} festgesetzt. Es wurde gezeigt, dass während der ersten Reduktion bei $T = 1773$ K, Risse innerhalb der Ceriumdioxidkörner

entstehen, dies aufgrund der chemischen Ausdehnung von reduziertem Ceriumdioxid. Dies führt zu schnelleren Oxidationsraten mit H_2O aufgrund der vergrößerten Oberfläche. In den weiteren Zyklen sintern die Risse zusammen, was zu einer Verkleinerung der Oberfläche führt und deshalb langsameren H_2 Produktionsraten. Eine erste Studie mit Reduktion bei $T = 1773 \text{ K}$ zeigte, dass die H_2 Raten des zweistufig porösen RPC mit kleinen und grossen Poren im μm -Bereich um 75% und 50%, respektive, sinken während 100 Zyklen. Die H_2 Raten des einstufig porösen RPC sinken hingegen um 90% während 59 Zyklen. Bei einer Reduktion bei $T = 1673 \text{ K}$ bleiben die Morphologie und die H_2 Raten mehrheitlich konstant. Das Langzeitzyklieren eines zweistufig porösen RPC zeigte, dass die H_2 Produktionsraten bei $\delta = 0.031 \text{ um}$ ungefähr 60% sinken während den ersten 200 Zyklen aber sich dann einpendeln bei $2 \text{ mL min}^{-1} \text{ g}^{-1}$. Die H_2 Produktion widerspiegelt die sinkenden H_2 Raten. Die relativ konstante Sauerstofffreisetzung zeigt die chemische Stabilität des Ceriumdioxid-RPC.

Acknowledgements

First, I would like to thank Prof. Dr. Aldo Steinfeld for giving me the opportunity to conduct my doctoral thesis under his supervision and for the opportunity to work in such an outstanding research environment at the Professorship of Renewable Energy Carriers (PREC) at ETH Zurich. His expertise, support and the confidence in my work were major sources of motivation throughout my doctoral thesis.

Special thanks go to Prof. Dr. Jonathan R. Scheffe, head of the Solar Thermochemical Energy Conversion Laboratory at University of Florida and former Postdoctoral Researcher and Senior Research Associate in the PREC group at ETH Zurich, for his great supervision during my doctoral thesis including valuable scientific advice, critical feedback, interesting discussions and also for acting as a co-examiner of this thesis.

I am very grateful to Dr. Martin Roeb, Institute of Solar Research at the National Aeronautics and Space Research Center in Germany (DLR), for serving as co-examiner of my thesis and for all the fruitful discussions within the Virtual Institute SolarSynGas.

I would like to express my thanks to my friends, colleagues and all past and present members of the PREC laboratory at ETH Zurich and the Solar Technologies Laboratory at the Paul Scherrer Institute (PSI). Special thanks go to Dr. Zoran Jovanovic, Dr. Martina Neises-von Puttkamer and Philipp

Haueter for all their support, fruitful discussions and for convincing me to conduct a doctoral study at PREC, it was a fantastic and valuable time. Personal thanks go to my colleagues Dr. Simon Ackermann, Dr. Thomas Cooper, Dr. Philipp Furler, Miriam Ezbiri, Daniel Marxer and Michael Welte for all the fruitful discussions about the solar reactors, cerium dioxide and perovskites and for all their help. Further thanks go to Dominik Herrmann for all his support in the PREC laboratory and for manufacturing many parts for all the experimental setups and to Alwin Frei for his support in all the analysis instruments located at PSI.

I gratefully acknowledge all the work performed within the Master Theses (MT) and Semester Projects (SP) that I have supervised throughout the course of my thesis (listed alphabetically): Michael Böckli (MT), Thomas Brunner (SP), Marco Caduff (SP), Marie Hoes (MT) and Carlo Speckert (MT).

Special thanks go to Roger Jacot and Prof. Dr. Greta Patzke at University of Zurich as well as to Dr. Alexander Bonk and Prof. Dr. Ulrich F. Vogt at EMPA Dubendorf for their help in material synthesis and sample characterization.

I gratefully acknowledge the financial support by the Swiss Federal Office of Energy (SI/501213-01), the Swiss Competence Center Energy & Mobility, the Helmholtz-Gemeinschaft Deutscher Forschungszentren (Virtuelles Institut SolarSyngas), and the European Research Council under the European Union's ERC Advanced Grant (SUNFUELS – no. 320541).

Finally, I would like to express my deepest gratitude to my family and friends, especially to Doris, Peter, Simon, Aline and Larissa. This thesis is dedicated to them.

Contents

Abstract	i
Zusammenfassung.....	v
Acknowledgements	xi
Nomenclature	xvii
1 Introduction.....	1
1.1 Two-step solar thermochemical H ₂ O/CO ₂ splitting	2
1.1.1 Ceria.....	5
1.2.2 Doped ceria.....	12
1.2.3 Perovskites.....	14
1.2 Thesis goals and outline.....	17
1.2.1 Thermodynamic characterization	17
1.2.2 Overall rates of metal oxide structures under solar conditions..	18
1.2.3 Morphological and thermochemical stability	19
2 Thermodynamic characterization of ceria and Zr doped ceria	21
2.1 Experimental section.....	22
2.1.1 Synthesis technique and sample characterization	22
2.1.2 Thermal analysis.....	25

2.2. Oxygen nonstoichiometry.....	26
2.3 Defect modeling.....	30
2.4 Thermodynamic properties.....	34
2.5 Water splitting.....	39
2.6 Efficiency analysis.....	41
2.7 Conclusions.....	46
3 Thermodynamic characterization of La-Mn based perovskites.....	49
3.1 Experimental section.....	50
3.1.1 Synthesis technique and sample characterization.....	50
3.1.2 Thermal analysis.....	55
3.2 Oxygen nonstoichiometry.....	55
3.3 Defect modeling.....	61
3.4 Thermodynamic properties.....	68
3.5 Water splitting.....	74
3.6 Conclusions.....	83
4 Overall rates of metal oxide structures under solar conditions.....	87
4.1 Experimental section.....	88
4.1.1 Sample preparation and characterization.....	88
4.1.2 Experimental set-up.....	89
4.2 Results and discussion.....	93
4.2.1 Optical thickness.....	95
4.2.2 Single- versus dual-scale porosity.....	101
4.2.3 Ceria versus Zr doped ceria.....	103

4.3 Conclusions.....	106
5 Long term cycling stability of ceria RPCs.....	107
5.1 Experimental section.....	108
5.1.1 Synthesis technique and sample characterization.....	108
5.1.2 Experimental setup	108
5.2 Results and discussion	112
5.2.1 H ₂ rate dependence on temperature	113
5.2.2 Influence of pore size on cycling stability	115
5.2.3 Investigation of cracks within ceria grains	120
5.2.4 Long term cycling.....	125
5.3 Conclusions.....	128
6 Outlook and research recommendations.....	129
A Appendix: Derivation of defect model for perovskites.....	135
B Appendix: Solar-TG measurements.....	141
B.1 XRD patterns of samples for solar-TG measurements.....	141
B.2 Radiative flux distribution.....	142
List of figures	143
List of tables.....	155
Bibliography	157
Curriculum vitae	167
List of publications.....	169

Nomenclature

Abbreviations

a.u.	arbitrary units
CZO_5	5 mol% Zr ⁴⁺ doped CeO ₂
CZO_10	10 mol% Zr ⁴⁺ doped CeO ₂
CZO_20	20 mol% Zr ⁴⁺ doped CeO ₂
DLR	German National Aeronautics and Space Research Centre
DS-RPC	reticulated porous ceramic with dual-scale porosity
ETH	ETH Zurich
fcc	single phase face centered cubic
FT	Fischer-Tropsch
GGE	gallon of gasoline energy equivalent
HFSS	high flux solar simulator
ICP-MS	inductively coupled plasma mass spectrometry
ICP-OES	inductively coupled plasma-atomic emission spectroscopy
IR	infrared
L	standard liters (at 273.15 K and 1 atm)
LCM40	La _{0.6} Ca _{0.4} MnO ₃
LCMA	La _{0.6} Ca _{0.4} Mn _{0.6} Al _{0.4} O ₃
LSM40	La _{0.6} Sr _{0.4} MnO ₃
LSMA	La _{0.6} Sr _{0.4} Mn _{0.6} Al _{0.4} O ₃
min.	minimum

MO	metal oxide
MS	mass spectrometer
Mtoe	million tons of oil equivalent
P	pressure sensor
ppi	pores per inch
PREC	Professorship of Renewable Energy Carriers
PSI	Paul Scherrer Institute
RPC	reticulated porous ceramic
SEM	scanning electron microscope
SSA	mass specific surface area
SS-RPC	reticulated porous ceramic with single-scale porosity
std.	standard
T or TC	thermocouple
TG	thermogravimetric analyzer
TGA	thermogravimetric analyzer (identical to TG)
USD	US dollar
XRD	X-ray diffraction

Symbols

C	flux concentration ratio of incident radiation	-
c_p	specific heat capacity	$\text{J mol}^{-1} \text{K}^{-1}$
$\Delta_r G_{\text{CO}_2}^\circ$	std. Gibbs free energy change of CO_2 formation reaction	J mol^{-1}
$\Delta_r G_{\text{H}_2\text{O}}^\circ$	std. Gibbs free energy change of H_2O formation reaction	J mol^{-1}
$\Delta_r G_{\text{ox}}^\circ$	std. Gibbs free energy change of MO oxidation with O_2	J mol^{-1}
$\Delta \bar{g}_\text{O}^\circ$	std. partial molar Gibbs free energy of reduction	J mol^{-1}
Δg_{red}	min. work for lowering p_{O_2} in reduction reaction of MO	J mol^{-1}
$\Delta h_{\text{H}_2\text{O}}$	energy required to heat and evaporate water	J mol^{-1}
HHV_{H_2}	higher heating value of H_2	J mol^{-1}
$\Delta \bar{h}_\text{O}^\circ$	standard partial molar enthalpy of reduction	J mol^{-1}
Δh_{red}	enthalpy change of reduction	J mol^{-1}

Δh_1°	enthalpy of Mn ⁴⁺ to Mn ³⁺ defect reaction	J mol ⁻¹
Δh_2°	enthalpy of Mn ⁴⁺ to Mn ²⁺ defect reaction	J mol ⁻¹
I	normal beam insolation	W m ⁻²
K_1	equilibrium constant for 1 st defect reaction	-
K_2	equilibrium constant for 2 nd defect reaction	-
K_f	CO ₂ formation equilibrium constant	-
K_W	H ₂ O dissociation equilibrium constant	-
M_O	molar mass of atomic oxygen	g mol ⁻¹
m_s	mass of reactive sample	g
M_S	molar mass of reactive sample	g mol ⁻¹
Δm_s	relative mass change of reactive sample	-
n_g	equilibrium molar amount of species g	mol
$n_{g,i}$	initial molar amount of species g	mol
n_{O_2}'	mass specific oxygen release	mol kg ⁻¹
p_g	partial pressure of gas g	bar
p_{tot}	total pressure	bar
p°	standard pressure (1 bar)	bar
$Q_{input,min}$	minimum amount of input energy to produce H ₂	J mol ⁻¹
R	universal gas constant	J mol ⁻¹ K ⁻¹
$\Delta \bar{s}_O^\circ$	standard partial molar entropy	J mol ⁻¹ K ⁻¹
T	temperature	K
\bar{T}	mean temperature	K
T_{ox}	oxidation temperature	K
T_{red}	reduction temperature	K
t	time	s
V_g	volume of gas g	L
V_S	volume of reactive sample	m ³
X	molar dopant concentration of Zr ⁴⁺	-
x	A-site molar dopant concentration	-
x	Zr ⁴⁺ dopant concentration	-

y	B-site molar dopant concentration	-
z	distance below sample top surface	m

Greek characters

α	stoichiometric coefficient of H ₂ O	-
β	stoichiometric coefficient of CO ₂	-
δ	degree of oxygen nonstoichiometry	-
δ_{ox}	degree of oxygen nonstoichiometry after oxidation	-
δ_{red}	degree of oxygen nonstoichiometry after reduction	-
$\eta_{\text{absorption}}$	solar absorption efficiency	-
η_{Carnot}	Carnot efficiency	-
$\eta_{\text{solar-to-fuel}}$	solar-to-fuel energy conversion efficiency	-
θ	angle XRD measurement	°
ξ_1	reaction coordinate of perovskite oxidation with O ₂	-
ξ_2	reaction coordinate of H ₂ O dissociation	-
σ	Stefan-Boltzmann constant	W m ⁻² K ⁻⁴

Defect chemistry

$\text{Ce}_{\text{Ce}}^{\times}$	tetravalent cerium on cerium lattice site
Ce'_{Ce}	trivalent cerium on cerium lattice site
$(\text{Ce}'_{\text{Ce}} \text{V}_{\text{O}}'' \text{Ce}'_{\text{Ce}})^{\times}$	oxygen vacancy-polaron association
Mn'_{Mn}	divalent manganese on manganese lattice site
$\text{Mn}^{\times}_{\text{Mn}}$	trivalent manganese on manganese lattice site
$\text{Mn}^{\bullet}_{\text{Mn}}$	tetravalent manganese on manganese lattice site
$\text{O}^{\times}_{\text{O}}$	oxygen atom on oxygen lattice site
$\text{V}_{\text{O}}^{\bullet}$	doubly ionized oxygen vacancy

Subscripts

i	initial
min	minimum

ox	oxidized/oxidation
red	reduced/reduction
S	reactive sample
set	set point
tot	total
W	water

Superscripts

eq	equilibrium
°	standard condition (for pressure 1 bar)

Chapter 1

Introduction

In 2013, the world's primary energy demand reached around 13'600 million tons of oil equivalent (Mtoe) whereas fossil fuels covered around 81%.¹ By 2040, the demand is expected to increase to 15'200 – 19'600 Mtoe, depending on the extrapolation scenario,¹ mainly due to global growth in population and expanding economic activity. Concerns about long term coverage of the increasing energy demand and about environmental issues, as for example greenhouse gas emissions, drive the search for sustainable alternative fuel and electricity production. The substitution of conventional crude oil based fuels would be of particular interest, due to its limited availability and its related CO₂ emissions during combustion. Regarding electricity production, substitution might be realized by using renewable sources such as wind, biomass, geothermal and solar power. However, for the transportation sector a high energy density is crucial. Therefore, synthetic liquid hydrocarbon fuels such as synthetic diesel, kerosene, or methanol derived from biomass or directly from H₂O and CO₂ might be more advantageous compared to, for example, hydrogen or batteries. Additionally, synthetic hydrocarbon fuels are compatible with our existing transportation infrastructure.

The production of synthetic hydrocarbon fuels from H₂O and CO₂ usually proceeds via the highly endothermic dissociation of H₂O and CO₂ to H₂,

CO and O₂. Then, in a second step, the mixture of H₂ and CO (called synthesis gas or syngas) is converted into liquid hydrocarbon fuels by conventional industrially implemented catalytic processes, such as Fischer-Tropsch process.^{2, 3} The dissociation of H₂O and/or CO₂ can be achieved using a wide range of technologies^{4, 5} including photoelectrochemical,⁶⁻⁸ electrolysis,^{9, 10} and thermochemical processes^{11,12}.

1.1 Two-step solar thermochemical H₂O/CO₂ splitting

Using concentrated solar irradiation to drive the endothermic dissociation of H₂O and CO₂ is of special interest due to the abundance of solar energy. H₂O could be directly dissociated into H₂ and O₂, towards high temperatures,¹³⁻¹⁵ however, in order to obtain a high conversion of H₂O into H₂, relatively high temperatures are required. Thermodynamically, at atmospheric pressure, temperatures above 2100 K and 2800 K are required to obtain a H₂ mole fraction of 0.01 and 0.1, respectively.¹⁴ Direct thermolysis of H₂O by using concentrated solar irradiation has been experimentally demonstrated^{13, 14} but the success of this process is limited by engineering challenges due to the high process temperatures, the high temperature separation of H₂ and O₂ or the rapid quenching of the product gas mixture in order to avoid recombination.

Compared to the direct splitting of H₂O and CO₂ in one step, two-step solar thermochemical splitting of H₂O and/or CO₂ offers the advantage of lower the maximum process temperature and to avoid separation of fuel (CO and/or H₂) and oxygen. Contrary to photochemical processes, solar thermochemical processes utilize the entire solar spectrum and thus offer a thermodynamically favorable path towards fuel production. The two-step solar thermochemical cycle is schematically shown in Figure 1.1. In the 1st step, the endothermic reduction, a generic metal oxide (MO_{ox}) is

reduced at elevated temperatures, typically under an atmosphere of low oxygen partial pressure (p_{O_2}), where the process heat is delivered by concentrated solar energy. In the exothermic 2nd step, the reduced metal oxide (MO_{red}) is exothermally re-oxidized with H_2O and/or CO_2 at lower temperatures to produce H_2 and/or CO . The oxidized metal oxide is then recycled to the 1st step. As the metal oxide is not consumed within the thermochemical cycle, the net inputs are simply H_2O and/or CO_2 and solar

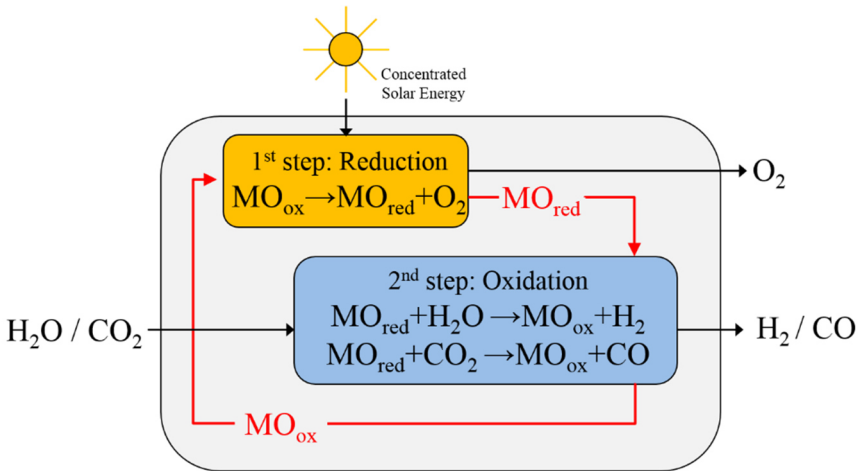


Figure 1.1. Schematic of the two-step solar thermochemical cycle based on a generic reactive metal oxide MO . In the endothermic 1st step, the metal oxide is reduced from the oxidized state MO_{ox} to the reduced state MO_{red} by using concentrated solar energy as the process heat. In the exothermic 2nd step, the reduced metal oxide is oxidized with H_2O and/or CO_2 to its initial state and H_2 and/or CO is produced. The metal oxide is then recycled to the 1st step.

energy, whereas the outputs are O_2 , H_2 and/or CO . The synthesis gas (H_2 and CO) can then be further processed to synthetic liquid hydrocarbon fuels by catalytic processes, such as Fischer-Tropsch process^{2,3} which can be then used in our transportation infrastructure. By combining this process with direct CO_2 capture from air,¹⁶⁻²⁰ the CO_2 from fuel

combustion could be captured and recycled to the solar thermochemical process and thus resulting in a carbon neutral process.

A variety of metal oxides have theoretically and experimentally been investigated as reactive intermediates for two-step solar thermochemical H_2O and CO_2 splitting.²¹⁻²⁴ Among the most promising ones are iron oxide,²⁵⁻²⁹ ferrites,³⁰⁻³² zinc oxide,³³⁻³⁷ ceria,³⁸⁻⁴³ doped ceria,⁴⁴⁻⁴⁹ and perovskites.⁵⁰⁻⁵⁸ The solar thermochemical cycles based on metal oxides can be broadly categorized into volatile and non-volatile cycles. Non-volatile redox cycles use reactive intermediates which remain in the solid state during reduction (*e.g.* iron oxide, ceria, perovskites), whereas volatile cycles are based on metal oxides that undergo gas-solid phase transitions (*e.g.* zinc oxide – zinc).²³ Typically, volatile reactions exhibit larger oxygen exchange capacity compared to non-volatile reactions, meaning that they release more oxygen and thus produce more fuel per mass of metal oxide. However, the volatile products must be quenched rapidly to avoid recombination which adds an energy penalty to the process. Non-volatile cycles can be subdivided into stoichiometric and non-stoichiometric reactions. Stoichiometric metal oxides typically form solid solutions upon reduction such as $\text{Fe}_3\text{O}_4(\text{s}) \rightarrow \text{FeO}-\text{Fe}_3\text{O}_4(\text{s})$ where Fe^{3+} is partially reduced to Fe^{2+} .^{23, 25} Non-stoichiometric metal oxides remain crystallographically stable while the lattice accommodates changes in anion or cation vacancies concentrations, such as $\text{CeO}_2(\text{s}) \rightarrow \text{CeO}_{2-\delta}(\text{s})$.^{23, 38} Non-stoichiometric reactions typically show smaller oxygen exchange capacity than stoichiometric reactions, but on the other hand feature relatively fast reaction kinetics and morphological stability over a wide range of temperatures and reduction extents.^{23, 38}

The efficiency of a solar thermochemical cycle is typically defined by the solar-to-fuel energy conversion efficiency $\eta_{\text{solar-to-fuel}}$,^{24, 39, 40, 42} defined as:

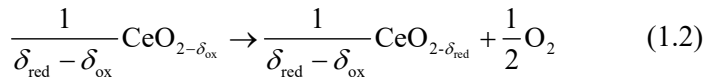
$$\eta_{\text{solar-to-fuel}} = \frac{\text{HHV}_{\text{fuel}} n_{\text{fuel}}}{Q_{\text{solar}} + Q_{\text{aux}}} \quad (1.1)$$

where HHV_{fuel} is the higher heating value of the fuel, n_{fuel} the amount of fuel being produced, Q_{solar} the solar energy input to the process and Q_{aux} additional energy penalties such as for vacuum pumping or inert gas consumption to promote the reduction reaction. Therefore, $\eta_{\text{solar-to-fuel}}$ strongly depends on the amount of fuel capable of being produced per amount of heat needed to heat up and reduce the metal oxide.

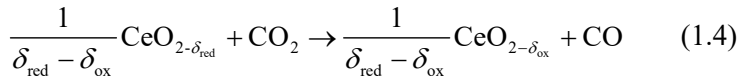
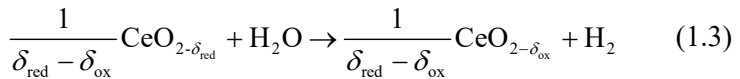
1.1.1 Ceria

Ceria (CeO_2) is currently considered a state-of-the-art material because it displays rapid oxidation⁵⁹ and reduction^{60, 61} kinetics, favorable oxidation thermodynamics^{50, 62, 63} and is morphologically stable over a range of temperatures and reduction extents.³⁸ The two-step thermochemical cycle using CeO_2 as reactive intermediate is represented by:

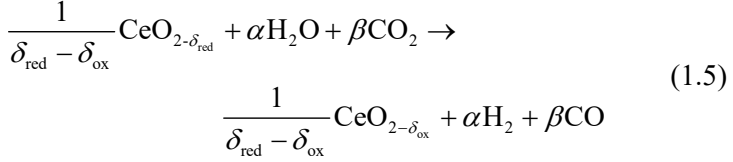
Reduction at T_{red} :



Oxidation at T_{ox} with H_2O or CO_2 :



or the oxidation with the combination of H_2O and CO_2 :



where δ_{red} and δ_{ox} are the oxygen nonstoichiometry of ceria after reduction and oxidation, respectively, and $\alpha + \beta = 1$. In the endothermic first step, Eq.(1.2), ceria is typically reduced under an atmosphere of low oxygen partial pressure (p_{O_2}) at elevated temperatures, generally $T_{\text{red}} > 1573$ K, where the process heat is delivered by concentrated solar energy. In the exothermic second step, Eq.(1.3) - (1.5), the reduced ceria is re-oxidized with H_2O and/or CO_2 at lower temperatures, generally $T_{\text{ox}} < 1573$ K, to produce H_2 and/or CO . The oxygen nonstoichiometry achieved after reduction and oxidation strongly depends on temperature and p_{O_2} in the system.^{64, 65} The maximum amount of H_2/CO capable of being produced per cycle and per mole of ceria is $\Delta\delta = \delta_{\text{red}} - \delta_{\text{ox}}$. As ceria is not consumed within the process, the net reactions are $\text{H}_2\text{O} \rightarrow \text{H}_2 + \frac{1}{2}\text{O}_2$ and $\text{CO}_2 \rightarrow \text{CO} + \frac{1}{2}\text{O}_2$ when performing oxidation either with H_2O or CO_2 or $\alpha \text{H}_2\text{O} + \beta \text{CO}_2 \rightarrow \alpha \text{H}_2 + \beta \text{CO} + \frac{1}{2}\text{O}_2$ when using a combination of H_2O and CO_2 .

Thermodynamics – The equilibrium oxygen nonstoichiometry δ measured by Panlener *et al.*⁶⁴ is shown in Figure 1.2 *versus* partial pressure of oxygen p_{O_2} for various temperatures. As an example, $\delta = 0.05$ is obtained when exposing ceria to $p_{\text{O}_2} \approx 1 \times 10^{-4}$ bar at $T = 1773$ K but also when exposing to $p_{\text{O}_2} \approx 1 \times 10^{-21}$ bar at $T = 1073$ K. In general, δ increases with increasing temperature and decreasing p_{O_2} . When conducting reduction under $p_{\text{O}_2} \approx 1 \times 10^{-4}$ bar at $T = 1773$ K and oxidation at $T = 1073$ K in CO_2 or H_2O , the molar yield of CO or H_2 per cycle per mol of ceria is $\Delta\delta \approx 0.05$ (assuming thermodynamic equilibrium in both reaction steps). Thermodynamically, δ_{red} is defined by the reduction temperature and the

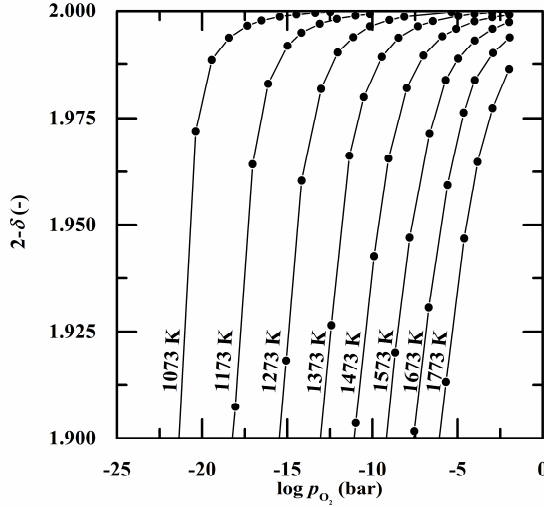


Figure 1.2. Equilibrium oxygen nonstoichiometry δ of ceria *versus* partial pressure of oxygen p_{O_2} for various temperatures between 1073 and 1773 K.⁶⁴

p_{O_2} of the sweep gas and/or the total pressure in the system. δ_{ox} is defined by the oxidation temperature and the resulting p_{O_2} of the CO/CO₂ or H₂/H₂O gas mixture. Thermodynamically, δ_{ox} is not affected by the total pressure under most conditions relevant for two-step solar thermochemical cycles, which is discussed in more detail in Chapter 3.5. The solar reduction of CeO₂ to Ce₂O₃ at temperatures above 2273 K has also been investigated but turned out to be impractical due to melting and vaporization of the redox material.⁶⁶

Figure 1.3 shows $\log r$ as a function of $\log p_{O_2}$ for $T = 1073$ and 1773 K, whereas $r = p_{H_2}/p_{H_2O}$ and $r = p_{CO}/p_{CO_2}$ for a mixture of H₂/H₂O and CO/CO₂, respectively. For H₂O (but similar for CO₂), r is calculated according to

$$r = \frac{p_{H_2}}{p_{H_2O}} = \frac{K_S}{p_{O_2}^{0.5}} \quad (1.6)$$

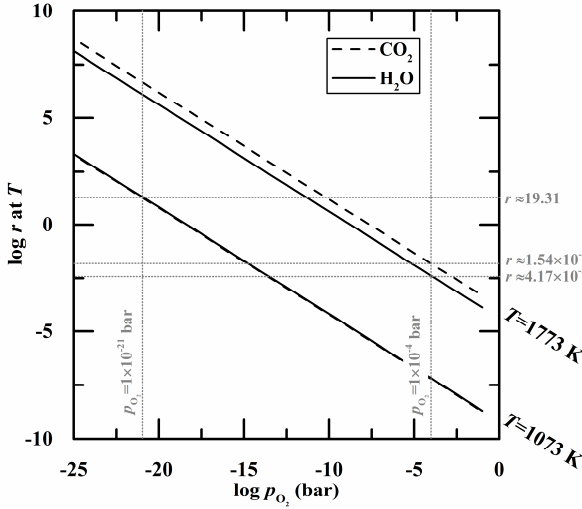


Figure 1.3. $\log r$ as a function of $\log p_{O_2}$ for $T = 1073$ and 1773 K, whereas $r = p_{H_2}/p_{H_2O}$ and $r = p_{CO}/p_{CO_2}$ for a mixture of H_2/H_2O and CO/CO_2 , respectively. Data is obtained from NIST-JANAF thermochemical tables.

where K_S is the equilibrium constant for the H_2O dissociation reaction, obtained from NIST-JANAF thermochemical tables. Assuming reduction reaction results in $\delta = 0.05$, p_{O_2} must be greater than 1×10^{-21} bar at $T = 1073$ K in order to oxidize ceria and hence produce fuel (*cf.* Figure 1.2). According to Figure 1.3, this implies a maximum $r \approx 19.31$ that can be thermodynamically attained during oxidation reaction (similar for H_2/H_2O and CO/CO_2 at $T = 1073$ K). This is equal to a maximum fuel concentration of around 95%. By conducting oxidation reaction isothermally at $T = 1773$ K, p_{O_2} must be greater than 1×10^{-4} bar. This results in maximum $r \approx 1.54 \times 10^{-2}$ and 4.17×10^{-3} for a CO/CO_2 and H_2/H_2O mixture, respectively. This implies a maximum fuel concentration of approximately 1.5% for CO/CO_2 and 0.4% for H_2/H_2O . As a conclusion, in order to attain high fuel concentrations, oxidation reaction of ceria (Eq. (1.3) - (1.5)) must be conducted at relatively lower temperatures (*e.g.* $T = 1073$ K). This is discussed in more detail in Chapter 2.5 and 3.5 for ceria,

doped ceria and for perovskites, respectively. Whether this limit in fuel concentration can be attained in a solar reactor also depends on the material's reaction kinetics.

Kinetics – Furler *et al.*⁶⁷ showed that the oxidation rates of porous ceria structures scale with their specific surface area (SSA). Therefore a reticulated porous ceramic (RPC) made of ceria with dual-scale porosity featuring pores in the mm- and μm -range ($0.095 \text{ m}^2 \text{ g}^{-1}$ SSA) exhibits a CO evolution one order of magnitude higher compared to a single-scale RPC with only pores in the mm-range ($1.45 \times 10^{-4} \text{ m}^2 \text{ g}^{-1}$ SSA).⁶⁷ Chueh *et al.*³⁸ showed almost fivefold increase in rates for H₂ production of Sm doped ceria when depositing Rh to the surface. Based on this result, it was concluded that the surface must be rate-limiting.³⁸ Ackermann *et al.*⁵⁹ performed a detailed kinetic analysis of the oxidation reaction of reduced ceria with CO₂. It was shown that oxidation rates increase with increasing temperature up to $T \approx 793 \text{ K}$, but also increase with increasing CO₂ concentration. For $\delta_{\text{red}} < 0.06$, it was found that oxidation rates increase with increasing δ_{red} , which is attributed to the formation of defect clusters or changes in morphology (formation of cracks) due to chemical expansion.⁵⁹ The oxygen diffusion within the ceria bulk is reported to be relatively fast.^{60, 61} For a characteristic length scale of 0.4 mm, reaction from $\delta = 0.017$ to 0.015 is predicted to be completed within a few seconds.⁶⁰ Due to the relatively fast oxygen bulk diffusion of ceria, the reduction reaction in a solar reactor is typically limited by heat transfer or by the p_{O_2} in the system.⁴²

Material structures and long term stability – Various porous ceria structures have been investigated such as 3D ordered macroporous CeO₂,⁶⁸ electrospun fibers,⁶⁹ porous monoliths,³⁹ porous felts,⁷⁰ and reticulated porous ceramics (RPC).⁶⁷ Although structures with submicron-sized pores exhibited relatively fast oxidation rates, they lacked

morphological stability as sintering occurred at elevated temperatures.⁶⁸ Furthermore, optically thick structures inhibited penetration of concentrated solar irradiation, resulting in non-uniform heating and non-uniform temperature distribution.⁴⁰ In contrast, the foam-type RPC structures offered enhanced heat and mass transport properties for high-temperature processing⁷¹ and have been developed with interconnected single-scale porosity (SS-RPC)⁴⁰ as well as with interconnected dual-scale porosity (DS-RPC)^{42, 67}. The larger mm-sized pores enabled efficient volumetric solar radiation absorption during reduction (Eq. (1.2)) due to appropriate optical thickness, while the smaller μm -sized pores within the struts enabled fast reaction rates during oxidation with CO_2 and H_2O (Eq. (1.3) – (1.5)) due to an increased specific surface area. RPCs with 76% overall porosity and 18% strut porosity (obtained by 30 vol% carbon pore forming agent) offer a trade-off between large specific surface area ($0.066 \text{ m}^2 \text{ g}^{-1}$) for fast oxidation kinetics and high mass loading per unit volume for large specific fuel yield,⁶⁷ while being morphologically stable over more than 200 redox cycles in a solar reactor at $T_{\text{red}} = 1773 \text{ K}$ and $T_{\text{ox}} = 1023 \text{ K}$.⁴² Chueh *et al.*^{38, 39} tested the reaction stability of porous ceria bricks in a differential reactor system over 500 redox cycles between $T_{\text{red}} = 1773 \text{ K}$ and $T_{\text{ox}} = 1073 \text{ K}$. Hydrogen production rate decreased by around 50% over the first 100 cycles, but then maintained a stable value of $1.3 \text{ ml min}^{-1} \text{ g}^{-1}$ for the remaining 400 cycles.³⁸ The H_2 and O_2 yield mirror the decreasing rate in H_2 productivity. The decrease in H_2 rate is attributed to a loss in surface by coarsening of the microstructure over time.³⁸ Rhodes *et al.*⁷² cycled a porous ceria structure in CO_2 and reported that the fuel production dropped by less than 14% over 2000 cycles.

Solar reactors – Several solar reactor concepts that use a temperature swing process based on nonstoichiometric ceria, have been investigated theoretically and experimentally, such as cavity-receivers with rotating

ring structures,⁷³ aerosol flow reactors,⁴³ moving packed bed reactors⁷⁴ and cavity receivers with stationary ceria structures^{39, 40, 42, 67, 70}. Isothermal redox cycling of ceria has also been investigated thermodynamically⁷⁵ and experimentally^{41, 76}. Isothermal processes offer a more simple operation because of avoiding cyclic heating and cooling of the ceria structure and therefore excluding solid-solid heat recovery. However, in order to attain high fuel outputs, large amounts of H₂O and/or CO₂ have to be delivered during oxidation (at least for $T \leq 1773$ K), which makes the isothermal process inefficient if heat from the product gas stream is not recovered.^{41, 75, 77} Depending on the downstream process (*e.g.* Fischer-Tropsch process), additional energy penalties have to be considered due to product gas separation (*e.g.* separation of CO and CO₂).

Energy conversion efficiency – Thermodynamic efficiency analyses predict that even in the absence of heat recovery, $\eta_{\text{solar-to-fuel}} = 20\%$ could be approached.^{38, 63, 77, 78} When including recovery of the sensible heat, $\eta_{\text{solar-to-fuel}}$ can even exceed 30%.^{63, 77, 78} However, it should be considered that $\eta_{\text{solar-to-fuel}}$ might strongly depend on the boundary conditions of the efficiency calculation, such as assumptions on gas and solid heat recovery effectiveness, pumping efficiency when including vacuum pumping, solar concentration ratio, work for product gas separation, energy penalty for inert gas cleaning and upper temperature limit of the redox material. So far, the highest demonstrated solar-to-fuel energy conversion efficiency for CO₂ splitting has been reported to be 1.72%.⁶⁷ A techno-economic evaluation of the production of methanol from CO₂ and H₂O using solar-thermal energy⁷⁹ showed that a solar-to-methanol energy conversion efficiency of 11.7% is feasible, assuming a solar reactor's energy conversion efficiency of 20%. When assuming production of liquid fuels *via* Fischer-Tropsch (FT) process, energy efficiency would be 11.3%. This

would result in a minimum selling price of 6.73 USD per GGE for methanol production and 7.01 USD per GGE for FT products.⁷⁹

1.2.2 Doped ceria

Since the reduction extent of ceria is generally lower than those obtained by other appropriate redox materials (*e.g.* ferrites, zinc oxide), its specific fuel production per mass is low.^{23, 38} This has a direct implication on efficiencies because they are largely dictated by the ratio of fuel produced to that of the thermal energy required to heat the oxide between oxidation and reduction steps.⁶³ Therefore, in an attempt to increase reduction extents, 4+ valence dopants such as Zr^{4+} ^{44, 47-49, 80} and Hf^{4+} ^{46, 47} are often introduced into the ceria lattice. Cycling studies of Zr^{4+} doped ceria have shown favorable reduction extents during reduction, but slower re-oxidation kinetics with CO_2 ^{47, 48} or H_2O ⁴⁵ have been observed compared to pure ceria. Scheffe *et al.*⁴⁷ showed that reduction extents of Zr^{4+} and Hf^{4+} doped ceria increase with increasing dopant concentration up to 15 mol% whereas re-oxidation is generally slower than for pure ceria but appeared to be strongly dependent on available surface area. Call *et al.*⁴⁸ concluded that reduction extents increase for dopant concentrations up to 22.5 mol%. Le Gal *et al.*⁴⁵ observed increasing oxygen release up to dopant concentrations of 25 mol% Zr^{4+} but the reduced forms could not be completely re-oxidized with steam at $T = 1323$ K. In summary, most of the above studies report consistent results, namely increasing reduction extents with 4+ valence dopant concentration but at the same time slower oxidation kinetics. Comparison between different works is difficult because the detailed experimental conditions (*e.g.* particle size) are generally not reported or controlled, and it is not clear from these studies whether thermodynamic limitations or inherent kinetics hinder the rates.

Thermodynamic studies have been performed at temperatures below the range of interest for thermochemical cycles. For example, Kuhn *et al.*⁸⁰ reported oxygen nonstoichiometric measurements of Zr^{4+} doped ceria at $T \leq 1273$ K and dopant concentrations between 5 and 80 mol%. Shah *et al.*⁸¹ reported measurements for Zr^{4+} concentrations of 19 and 75 mol% at $T \leq 1173$ K and $p_{O_2} \leq 10^{-10}$ bar. Recently, Hao *et al.*⁴⁹ published nonstoichiometric measurements at higher temperatures for Zr^{4+} dopant concentrations up to 20 mol% in the range $T = 873$ K to 1763 K and $p_{O_2} \approx 10^{-27}$ bar to 1 bar. All three studies^{49, 80, 81} indicate higher oxygen nonstoichiometry for doped ceria compared to undoped ceria, which increases with increasing dopant concentration up to 20 mol%, and derive partial molar enthalpy and entropy values slightly lower than those for undoped ceria.^{64, 65, 82, 83} The oxygen nonstoichiometry of 5 mol% Zr^{4+} doped ceria measured by Kuhn *et al.*⁸⁰ is shown in Figure 1.4 (triangles) and compared to the measurements of pure ceria⁶⁴ (circles). 5 mol% Zr^{4+}

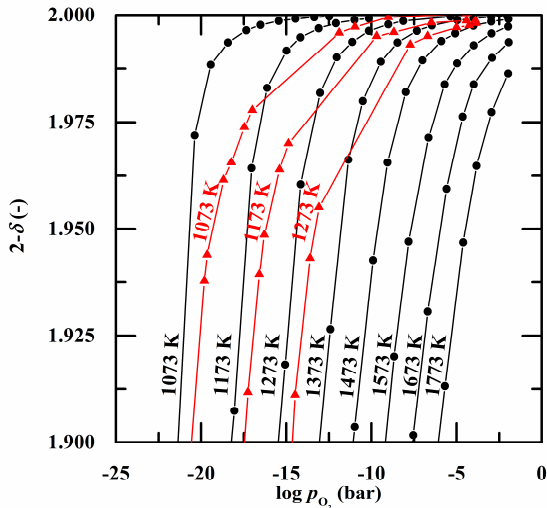


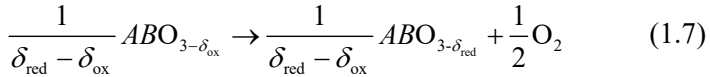
Figure 1.4. Equilibrium oxygen nonstoichiometry δ of ceria⁶⁴ (circles) and 5 mol% Zr^{4+} doped ceria⁸⁰ (triangles) versus partial pressure of oxygen p_{O_2} for various temperatures.

doped ceria shows significantly larger reduction extents compared to pure ceria especially towards smaller δ values. For example, at $T = 1273$ K and $p_{\text{O}_2} \approx 1 \times 10^{-13}$ bar, $\delta = 0.018$ for ceria and $\delta = 0.045$ for 5 mol% Zr^{4+} doped ceria meaning that under these conditions, the doped ceria reduces almost 150% more compared to undoped ceria.

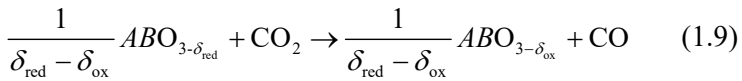
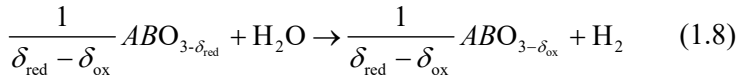
1.2.3 Perovskites

Perovskite oxides have recently been proposed as promising alternative reactive intermediate for solar thermochemical $\text{H}_2\text{O}/\text{CO}_2$ splitting because of potentially increasing the energy conversion efficiency by lowering the reduction temperature or increasing the mass specific fuel yield.^{50-56, 58, 84, 85} Similarly to the ceria based cycle, the two-step solar thermochemical cycle based on a generic perovskite (ABO_3) is represented by

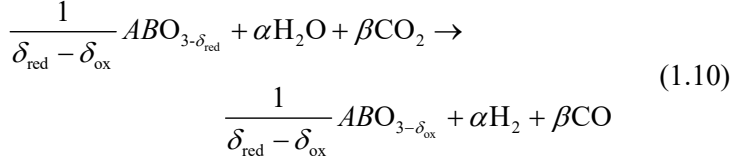
Reduction at T_{red} :



Oxidation at T_{ox} with H_2O or CO_2 :



or the oxidation with the combination of H_2O and CO_2 :



where Eq. (1.7) represents the high-temperature endothermic reduction and Eq. (1.8) - (1.10) the lower temperature exothermic oxidation with H₂O or CO₂ or the combination with H₂O and CO₂. δ_{red} and δ_{ox} represent the oxygen nonstoichiometry after reduction and oxidation, respectively, whereas the difference $\Delta\delta = \delta_{\text{red}} - \delta_{\text{ox}}$ is the molar amount of fuel produced per cycle per mole of metal oxide. Scheffe *et al.*⁵⁰ considered strontium-doped lanthanum manganites La_{1-x}Sr_xMnO₃ ($x = 0.30, 0.35, 0.40$) and reported reduction extents of La_{0.6}Sr_{0.4}MnO₃ to be nearly 6.5 times larger than those of ceria at 1600 K and twice larger at 1800 K, both for $p_{O_2} = 10^{-5}$ bar. However, it was shown that their theoretical solar-to-fuel energy conversion efficiency is lower compared to that of ceria because of the thermodynamically less favorable oxidation with CO₂ and H₂O. Based on measurements of Mizusaki *et al.*⁸⁴, Yang *et al.*⁵² concluded higher reduction extents and, consequently, higher fuel yields with increasing x for La_{1-x}Sr_xMnO₃ ($0 \leq x \leq 0.5$), while H₂O-to-H₂ conversion rate decreased with increasing x . This led to the conclusion that intermediate doping levels may be optimal for solar-to-fuel energy conversion. McDaniel *et al.*⁵¹ showed even higher CO and H₂ yields when additionally doping Al to the B-site of La_{1-x}Sr_xMnO₃ while maintaining fast oxidation rates with CO₂ and H₂O. Dey *et al.*⁵³ showed increasing reduction extents and fuel productivity when replacing the divalent A-site dopant Sr in La_{1-x}Sr_xMnO₃ with Ca and obtained best results for $x = 0.5$. In another recent work,⁵⁴ they investigated two series of perovskites oxides, Ln_{0.5}Sr_{0.5}MnO₃ and Ln_{0.5}Ca_{0.5}MnO₃ (Ln = La, Nd, Sm, Gd, Dy, and Y) and concluded highest O₂ release for the manganite with the smallest A-site cation radii (in this

case Y). A comparison between $\text{La}_x\text{Sr}_{1-x}\text{MO}_3$ ($M = \text{Mn}, \text{Co}, \text{Fe}$) and $\text{Ba}_x\text{Sr}_{1-x}(\text{Co}, \text{Fe})\text{O}_3$ ⁵⁵ showed best results for the Mn-containing perovskites. In a very recent study by Cooper *et al.*⁸⁵, Sr and Ca A-site doped lanthanum-manganites, with and without B-site doping of Al, were examined for redox performance and compared to the state-of-the-art material ceria. $\text{La}_{0.6}\text{Sr}_{0.4}\text{Mn}_{0.6}\text{Al}_{0.4}\text{O}_3$ and $\text{La}_{0.6}\text{Ca}_{0.4}\text{Mn}_{0.6}\text{Al}_{0.4}\text{O}_3$ reach four to nine times higher reduction extents compared to ceria in the temperature range $T = 1473 \text{ K} - 1673 \text{ K}$, while maintaining fast oxidation kinetics with CO_2 . Bork *et al.*⁵⁶ reported that $\text{La}_{0.6}\text{Sr}_{0.4}\text{Cr}_{1-x}\text{Co}_x\text{O}_3$ with the optimal dopant concentration $x = 0.2$ can split up to 25 times more CO_2 when cycling at $T = 1073 \text{ K} - 1473 \text{ K}$ compared to ceria or exhibits similar reduction extents ($\delta = 0.034$) at 300 K lower temperatures (1473 K instead of 1773 K). On the other hand, cyclability redox studies by Galvez *et al.*⁵⁸ revealed that the chemical stability of Ca, Sr and Al-doped La-Mn perovskites is detrimentally affected by sintering and by the formation and eventual segregation of a carbonate phase during oxidation by CO_2 .

Some of the conclusions drawn for the perovskites discussed above are mainly based on qualitative reduction experiments under an inert flow of low p_{O_2} and oxidation under a relatively high flow of CO_2 and/or H_2O in a thermogravimetric analyzer⁵³⁻⁵⁶ and/or in an electrically heated furnace coupled to a gas analysis.^{51, 53} Such experiments with large excess of CO_2 and/or H_2O can result in misleading conclusions, as indicated by various thermodynamic analyses.^{50, 52, 85} In the work of Yang *et al.*⁵², the amount of H_2O needed to oxidize $\text{La}_{1-x}\text{Sr}_x\text{MnO}_3$ ($0 \leq x \leq 0.4$) to a certain δ_{ox} , and hence produce a fixed amount of H_2 in a closed system with variable volume was calculated from thermodynamic data. Similar calculations were performed by Scheffe *et al.*⁵⁰ and Cooper *et al.*⁸⁵, however, there, the initial amount of CO_2 and/or H_2O was fixed and the fuel yield was predicted as a function of oxidation temperature. Such thermodynamic

fuel yield calculations allow for an accurate determination of the material's potential to efficiently split CO₂ and/or H₂O.

1.2 Thesis goals and outline

The objective of this thesis is to critically evaluate the potential of promising nonstoichiometric redox materials, namely: ceria, Zr⁴⁺ doped ceria and La-Mn based perovskites, to be used as reactive intermediates in two-step solar thermochemical redox cycles. The material's evaluation contains:

- Thermodynamic characterization
- Investigation of overall rates of redox reactions under solar conditions
- Determination of morphological and thermochemical stability

1.2.1 Thermodynamic characterization

Thermodynamic characterization was focused on undoped ceria and Zr⁴⁺ doped ceria, but also on other potentially promising oxides such as lanthanum-manganese based perovskites.^{50, 51, 57} Thermodynamic characterization of undoped and Zr⁴⁺ doped ceria is presented in Chapter 2. The characterization of lanthanum-manganese perovskites doped with Sr²⁺, Ca²⁺ and Al³⁺ is shown in Chapter 3. The thermodynamic analyses are divided into the following steps:

- Sample preparation and characterization
- Measurement of oxygen nonstoichiometry as a function of temperature and oxygen partial pressure by thermogravimetric analysis
- Development of appropriate defect models to describe oxygen nonstoichiometry as a function of temperature and oxygen partial pressure

- Determination of thermodynamic properties, namely standard partial molar enthalpy, entropy and Gibbs free energy ($\Delta\bar{h}_0^\circ$, $\Delta\bar{s}_0^\circ$ and $\Delta\bar{g}_0^\circ$)
- Calculation of hydrogen productivity for varying oxidation temperatures and varying amounts of steam
- Determination of the theoretical solar-to-fuel energy conversion efficiency

Such a thermodynamic analysis allows a straightforward and quantitative methodology for evaluating the thermodynamic potential of promising redox materials to be used in solar thermochemical redox cycles for producing H₂ and/or CO. It is envisioned that this work can be translated to not only solar thermochemical applications, but also to oxygen storage capacitance in automobiles^{86, 87} and electrolytes in solid oxide fuel cells^{88, 89}.

1.2.2 Overall rates of metal oxide structures under solar conditions

Chapter 4 presents the investigation of the overall rates of redox reactions, including heat and mass transport phenomena, using a solar-driven thermogravimetric analyzer (solar-TG), in which redox material structures are directly exposed to high-flux irradiation. With this arrangement, the overall rate of thermochemical reactions can be determined under similar radiative heat transfer characteristics typical of high-temperature solar reactors operated in concentrating solar systems, such as solar towers and dishes, thus mimicking realistic operating conditions.^{90, 91} This analysis is restricted to reticulated porous ceramic (RPC) structures made of undoped and Zr⁴⁺ doped ceria, as well as commercially available ceria fibers.

1.2.3 Morphological and thermochemical stability

Chapter 5 presents the morphological and thermochemical cycling stability of ceria RPC structures investigated in an infrared (IR) gold image furnace setup. The metal oxide structures are cycled for a number of times according to Eq. (1.2) and (1.3) while the yield and the rate of reactions are monitored *versus* cycle number. Morphological changes during cycling are optically characterized by scanning electron microscopy (SEM). This analysis allows to determine and predict a material's chemical and morphological stability over hundreds of cycles in a solar reactor.

Chapter 2

Thermodynamic characterization of ceria and Zr⁴⁺ doped ceria¹

In this chapter, the thermochemical performance of undoped and Zr⁴⁺ doped ceria is evaluated by using 5 mol% Zr⁴⁺ as a case study. Oxygen nonstoichiometry is reported in the operation range of solar reactors ($1573 \text{ K} \leq T_{\text{red}} \leq 1773 \text{ K}$, $2.3 \times 10^{-4} \text{ bar} < p_{\text{O}_2} < 4.56 \times 10^{-3} \text{ bar}$) for 5 mol% Zr⁴⁺ doped ceria (CZO_5) and undoped ceria (CeO₂). Appropriate defect models are developed to describe the defect chemical equilibria and partial molar thermodynamic properties ($\Delta \bar{h}_0^\circ$, $\Delta \bar{s}_0^\circ$ and $\Delta \bar{g}_0^\circ$) are extracted. From such data coupled with thermodynamic data from the literature, equilibrium hydrogen yields and theoretical solar-to-fuel energy conversion efficiencies for dopant concentrations as high as 20 mol% are determined. This analysis allows a straightforward and quantitative methodology for evaluating the potential of Zr⁴⁺ doped ceria to be used in solar thermochemical redox cycles.

¹ Material from this chapter has been published in: M. Takacs, J.R. Scheffe and A. Steinfeld, "Oxygen nonstoichiometry and thermodynamic characterization of Zr doped ceria in the 1573-1773 K temperature range", *Physical Chemistry Chemical Physics*, vol. 17, no. 12, pp. 7813-7822, 2015

2.1 Experimental section

2.1.1 Synthesis technique and sample characterization

5 mol% Zr^{4+} doped CeO_2 (CZO_5) powder was synthesized by sol-gel method as described by Scheffe *et al.*⁴⁷. Briefly, $\text{Ce}(\text{NO}_3)_3 \cdot 6\text{H}_2\text{O}$ (Aldrich, catalog number 238538), $\text{ZrO}(\text{NO}_3)_2 \cdot 6.3\text{H}_2\text{O}$ (Aldrich, catalog number 243493) and dry citric acid (Merck, catalog number 818707) in aqueous solution were used to carry out the synthesis. The ratio of the metal cations to the citric acid was 1:1.5. CeO_2 powder was purchased from a commercial distributor (Aldrich, catalog number 211575). CeO_2 and CZO_5 powders were uniaxially cold-pressed at 5 tons and sintered at 1873 K under air atmosphere for 5 hours into ~1250 mg dense cylindrical pellets. The approximate dimensions after sintering were 7 mm diameter and 5 mm height. The CZO_5 dopant concentration was measured by inductively coupled plasma mass spectrometry (ICP-MS) analysis and was 4.5 mol%. Powder X-ray diffraction (XRD) was performed in the Bragg Brentano geometry using $\text{Cu K}\alpha$ radiation (Philips, PANalytical/X'Pert MPD/DY636, $\lambda=1.5406 \text{ \AA}$, $2\theta=20\text{-}100^\circ$, $0.01^\circ/\text{s}$ scan rate, 45 kV/20 mA output). XRD patterns are shown in Figure 2.1 where (a) shows the formation of single-phase face-centered cubic structures for CeO_2 and CZO_5, and (b) the shift of the (111) reflection towards higher angles for CZO_5, indicating a lattice contraction due to the substitution of Ce^{4+} by Zr^{4+} . Scanning electron microscopy (SEM) of the dense pellets was conducted on a TM-1000 Microscope (Hitachi, 15 kV accelerating voltage) and shown in Figure 2.2. SEM images show well sintered dense pellets with a grain size in the range 10-50 μm for CeO_2 and CZO_5.

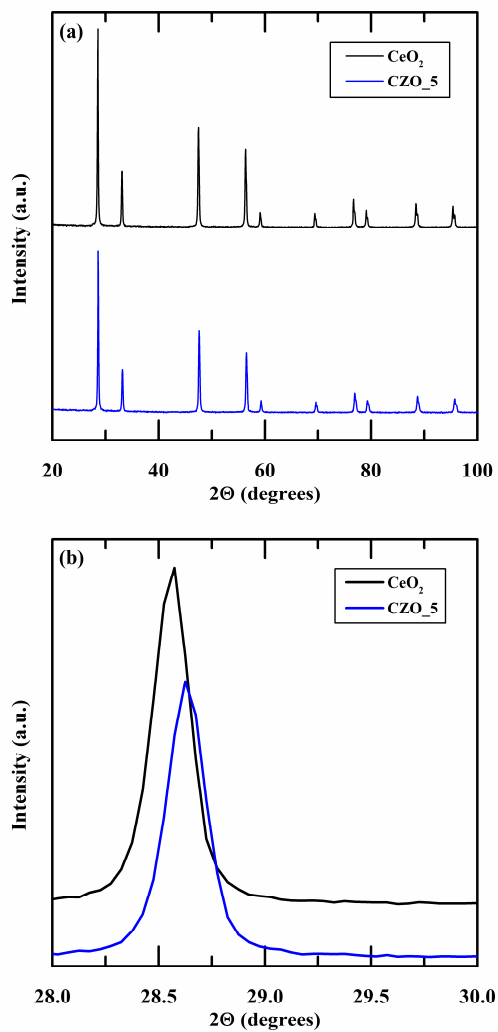


Figure 2.1. (a) XRD patterns of CeO₂ and CZO_5 powder. (b) (111) reflection of CeO₂ in comparison with CZO_5.

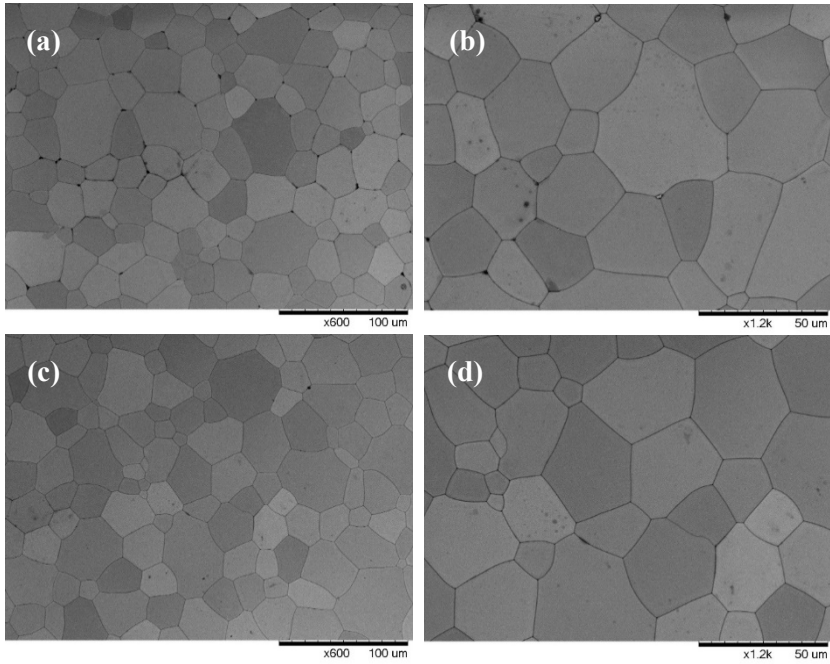


Figure 2.2. SEM images of the sintered CeO₂ pellet with (a) $\times 600$ and (b) $\times 1.2k$ magnification and of the sintered CZO_5 pellet with (c) $\times 600$ and (d) $\times 1.2k$ magnification.

2.1.2 Thermal analysis

Oxygen nonstoichiometry (δ) was measured using a thermogravimetric analyzer (TGA) (Setaram, Setsys Evolution), schematically shown in Figure 2.3. Samples were suspended to the scale with a custom-made platinum hook to ensure good exposure to the purge gas and eliminate gas diffusion limitations. A photograph of the platinum hook suspending the dense ceria pellet is shown in Figure 2.5. Special care was taken to ensure that reduction and oxidation reactions were not limited by gaseous mass transfer but by solid-state diffusion and/or surface reactions. The p_{O_2} of the surrounding gas atmosphere was controlled by mixing Ar (Messer, Argon 4.6) with an O_2/Ar mixture (Messer, 0.5% O_2 5.0 in Ar 5.0). Gases were mixed with electronic

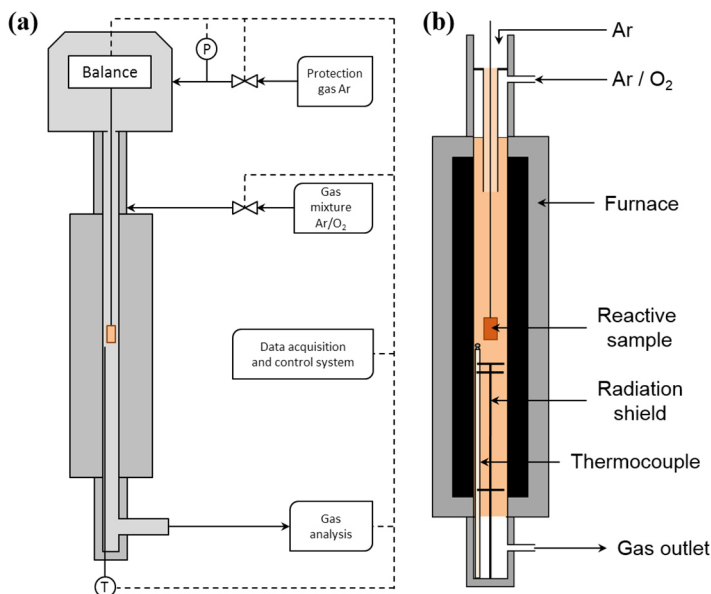


Figure 2.3. Schematic of the thermogravimetric analyzer (TGA) (Setaram Setsys Evolution). (a) shows an overview of the TGA whereas (b) shows a more detailed schematic of the furnace part. P and T denote pressure sensor and thermocouple, respectively.



Figure 2.4. Photograph of the custom-made platinum hook suspending the dense ceria pellet to the TGA balance.

mass flow controllers (Brooks, Model 5850TR, accuracy $\pm 1\%$) with a constant total flow rate of 200 mL/min. The gas species and concentrations at the outlet were monitored by mass spectrometry (Pfeiffer Vacuum, OmniStar GSD 320). Temperature was varied between 1573 K and 1773 K and p_{O_2} between 4.56×10^{-3} bar and 2.3×10^{-4} bar. In all measurements, the sample mass (m_s) was equilibrated at a constant temperature and p_{O_2} . Following each equilibrium measurement, the p_{O_2} was rapidly changed by adapting the O_2/Ar gas mixture, resulting in a temporal weight change of the sample due to evolving or uptaking of oxygen until a new equilibrium was reached. To correct for buoyancy, blank runs were performed with Al_2O_3 sintered pellets of same dimensions. An additional correction was applied for a small amount of sample sublimation (< 0.04 wt%) observed above 1723 K.

2.2. Oxygen nonstoichiometry

An exemplary experiment showing the dynamics of the reduction (decreasing p_{O_2}) and oxidation (increasing p_{O_2}) of CZO_5 and CeO_2 at 1573 K and 1773 K is shown in Figure 2.5(a). Initially, their weights were stabilized at a constant p_{O_2} , followed by a rapid p_{O_2} decrease to initiate

reduction. After stabilization at the new m_s, p_{O_2} is increased back to its initial value to commence oxidation. At 1573 K, the reduction and oxidation of CZO_5 are noticeably slower than those of CeO₂. However, at 1773 K, the kinetic rates are similar for both materials. If surface reactions are assumed not to be limiting – a reasonable assumption at these length scales – this would imply that the activation energy for ambipolar diffusion is higher in the case of CZO_5.

Figure 2.5(b) shows the mass change in wt% of CeO₂ and CZO_5 as a function of time for $T = 1673$ K for a broader range of p_{O_2} and Figure 2.5(c) shows all the reduction and oxidation runs over all temperatures and p_{O_2} . Samples were heated to 5 different set point temperatures followed by isothermal reduction and oxidation by stepwise changing p_{O_2} . As seen, CZO_5 released more oxygen than CeO₂ under all measurement conditions. The much slower oxidation of CZO_5 at 1073 K agrees well with the observation that its activation energy for ambipolar diffusion is higher than CeO₂ (*c.f.* Figure 2.5(a) and discussion above). A total sublimated mass of 0.40 mg and 0.32 mg at 1773 K was observed for CeO₂ and CZO_5, respectively.

Oxygen nonstoichiometry is calculated according to:

$$\delta = \Delta m_s \cdot \frac{M_s}{M_o} \quad (2.1)$$

where Δm_s is the relative weight loss at equilibrium, M_s is the molar mass of the sample and M_o the molar mass of O. Measured δ versus p_{O_2} of CeO₂ and CZO_5 for all temperatures investigated are shown in Figure 2.6(a) and Figure 2.6(b), respectively. Open symbols show δ measurements of this work whereas literature data are shown by closed symbols (Panlener *et al.*⁶⁴) and crossed symbols (Iwasaki *et al.*⁹²). Lines indicate defect models used to describe δ , presented in the following section. As seen, δ of CZO_5 is higher

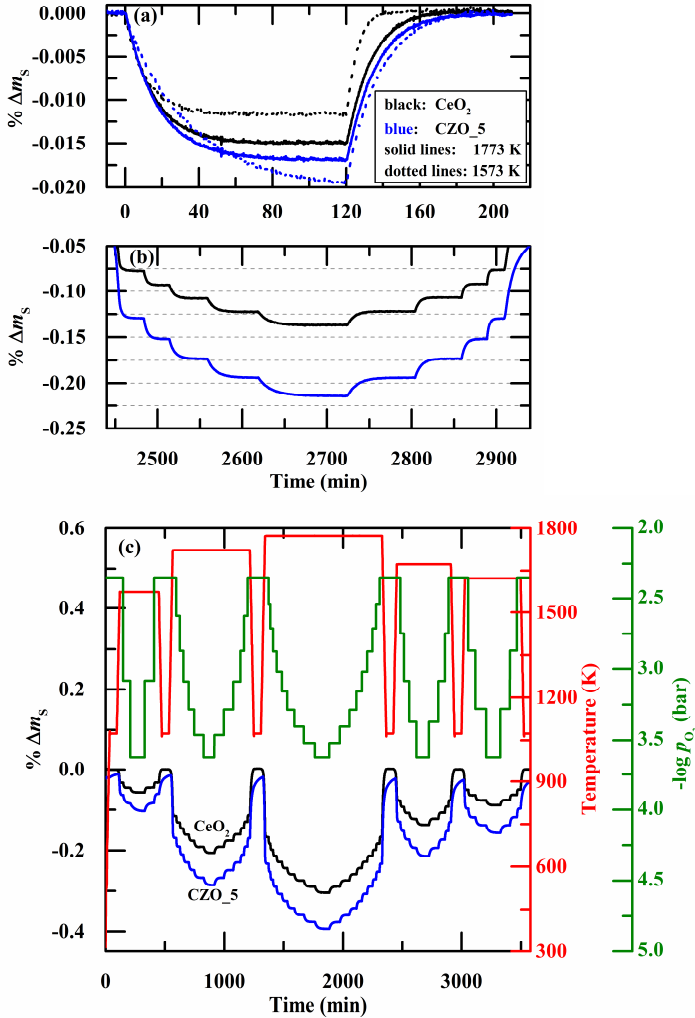


Figure 2.5. (a) Mass change in wt% as a function of time for the reduction and oxidation of CeO₂ (black) and CZO₅ (blue) at $T = 1773$ K where p_{O_2} was changed between 3.0×10^{-4} bar and 2.3×10^{-4} bar (solid lines) and at $T = 1573$ K where p_{O_2} was changed between 8.2×10^{-4} bar and 2.3×10^{-4} bar (dotted lines). (b) Mass change in wt% as a function of time for the reduction and oxidation runs of CeO₂ (black) and CZO₅ (blue) at $T = 1673$ K and O₂ partial pressure range $p_{O_2} = 4.50 \times 10^{-3} - 2.3 \times 10^{-4}$ bar. (c) Mass change in wt% as a function of time for all the reduction and oxidation runs of CeO₂ and CZO₅ in the temperature range $T = 1573 - 1773$ K and O₂ partial pressure range $p_{O_2} = 4.56 \times 10^{-3} - 2.3 \times 10^{-4}$ bar.

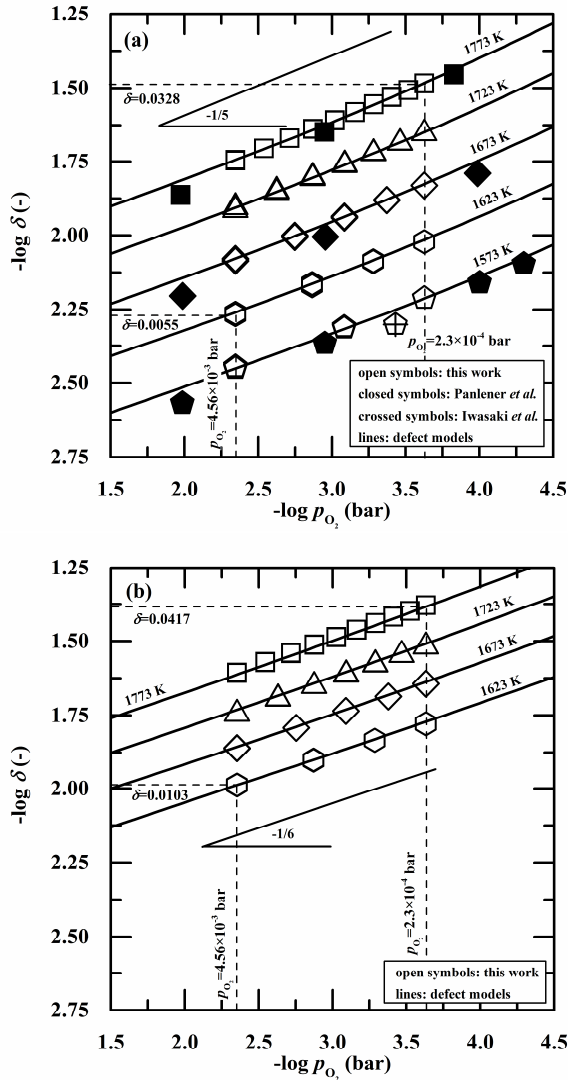
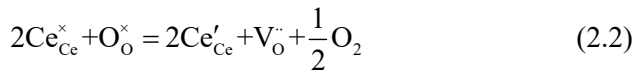


Figure 2.6. Measured δ (open symbols) of CeO_2 (a) and CZO_5 (b) for $T = 1573$ K to 1773 K and $p_{O_2} = 4.56 \times 10^{-3}$ bar to 2.3×10^{-4} bar and a comparison to literature data: Panlener *et al.*⁶⁴; closed symbols, Iwasaki *et al.*⁹²; crossed symbols. Lines indicate defect models used to describe δ .

over the whole measurement range investigated compared to CeO₂. Improvement in oxygen release is highest at low T_{red} and high p_{O_2} . For example, at $T = 1623$ K and $p_{\text{O}_2} \approx 4.56 \times 10^{-3}$ bar, the improvement is almost 90% per mole of oxide ($\delta = 0.010$ for CZO_5 and $\delta = 0.0055$ for CeO₂) and around 27% at $T = 1773$ K and $p_{\text{O}_2} \approx 2.3 \times 10^{-4}$ bar ($\delta = 0.042$ for CZO_5 and $\delta = 0.033$ for CeO₂). Nonstoichiometry of CZO_5 at 1573 K is not shown because the sample weight did not equilibrate completely within the allotted time due to slower kinetics. δ values of pure CeO₂ measured in this work are slightly higher than the values reported in literature,^{64, 92} especially towards higher p_{O_2} . The reason for the discrepancy is not clear but may be related to sample impurities and sublimation. Panlener *et al.*⁶⁴ performed oxygen nonstoichiometry measurements based on thermogravimetric analysis over a broad range of p_{O_2} from 0.01 bar to 10^{-23} bar between 873 K and 1773 K while Iwasaki *et al.*⁹² performed measurements only at temperatures up to 1573 K.

2.3 Defect modeling

Defect models were used to describe the chemical equilibria of both CeO₂ and CZO_5. For small reduction extents (as small as $\delta = 0.01$ for pure ceria and higher with dopant type and dopant concentration⁹³) the reduction of ceria and doped ceria can be described in Kröger-Vink notation as:

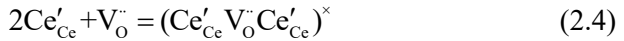


where oxygen atoms on oxygen lattice sites ($\text{O}_{\text{O}}^{\times}$) and cerium on cerium lattice sites ($\text{Ce}_{\text{Ce}}^{\times}$) are in equilibrium with gaseous oxygen, doubly ionized oxygen vacancies ($\text{V}_{\text{O}}^{\cdot\cdot}$) and electrons localized on cerium lattice sites (Ce'_{Ce}). Assuming there are no cluster formations between the various defects, δ can be described by:^{80, 94}

$$\delta = \text{constant} \cdot p_{\text{O}_2}^{-1/6} \Big|_{T=\text{const.}} \quad (2.3)$$

which implies a slope of -1/6 when plotting $\log \delta$ versus $\log p_{\text{O}_2}$.

For larger deviations from stoichiometry, the formation of oxygen vacancy-polaron associations $(\text{Ce}'_{\text{Ce}} \text{V}_{\text{O}}'' \text{Ce}'_{\text{Ce}})^{\times}$ should be accounted for, and is described as:



Assuming all defects form associations according to Eq.(2.4)⁹⁴,

$$\delta = \text{constant} \cdot p_{\text{O}_2}^{-1/2} \Big|_{T=\text{const.}} \quad (2.5)$$

As seen in the case of CeO_2 (Figure 2.6(a)), the slope of $\log \delta$ vs. $\log p_{\text{O}_2}$ best describing the data is close to -1/5, indicating that Eq.(2.3) cannot adequately describe its defect equilibria, in agreement with previous investigations^{64, 82, 93, 95, 96}. A slope of -1/5 indicates that a combination of both defect models (Eq.(2.2) and Eq.(2.4)) is needed to accurately describe ceria's defect chemistry, as evidenced by Otake *et al.*⁹³ who showed that the isolated defect model is only valid for very low nonstoichiometries ($\delta < 0.01$). A slope of -1/6, on the other hand adequately describes the data of CZO_5 over the entire measurement range. This is consistent with observations of 3+ valence dopants such as Sm^{3+} ,^{88, 96} Gd^{3+} ⁹⁶⁻⁹⁸ and Y^{3+} ,⁹³ but in such cases much higher concentrations are required to describe the measurement data with only a single defect model. For example, when doping ceria with 10 mol% Y^{3+} , a single isolated defect model can only describe the data up to $\delta \approx 0.02$, whereas in the case of 20 mol% it is valid until $\delta \approx 0.03$. Here, with only 5 mol% Zr^{4+} a single model appears to adequately describe δ at least until $\delta \approx 0.04$.

The nonstoichiometry as a function of T and p_{O_2} may be modelled by fitting appropriate equilibrium constants from Eq.(2.2) and Eq.(2.4) to the experimental data. To do so, the following site and charge relations for 4+ valence dopants and pure ceria⁹³ are needed:

$$[\text{Ce}_{\text{Ce}}^{\times}] = 1 - 2\delta - X \quad (2.6)$$

$$[\text{O}_0^{\times}] = 2 - \delta \quad (2.7)$$

$$2[\text{V}_0^{\cdot\cdot}] = [\text{Ce}'_{\text{Ce}}] \quad (2.8)$$

$$2\delta = [\text{Ce}'_{\text{Ce}}] + 2[(\text{Ce}'_{\text{Ce}} \text{V}_0^{\cdot\cdot} \text{Ce}'_{\text{Ce}})^{\times}] \quad (2.9)$$

where $X = 0.045$ is the dopant concentration of Zr^{4+} in the case of CZO_5. Thus, the equilibrium constants K_1 for Eq. (2.2) and K_2 for Eq. (2.4) are given by:

$$K_1 = \frac{[\text{Ce}'_{\text{Ce}}]^2 [\text{V}_0^{\cdot\cdot}] p_{O_2}^{1/2}}{[\text{Ce}_{\text{Ce}}^{\times}]^2 [\text{O}_0^{\times}]} = \frac{4[\text{V}_0^{\cdot\cdot}]^3 p_{O_2}^{1/2}}{(1 - 2\delta - X)^2 (2 - \delta)} \quad (2.10)$$

$$K_2 = \frac{[(\text{Ce}'_{\text{Ce}} \text{V}_0^{\cdot\cdot} \text{Ce}'_{\text{Ce}})^{\times}]}{[\text{Ce}'_{\text{Ce}}]^2 [\text{V}_0^{\cdot\cdot}]} = \frac{\delta - [\text{V}_0^{\cdot\cdot}]}{4[\text{V}_0^{\cdot\cdot}]^3} \quad (2.11)$$

K_1 and K_2 can be determined through a least square minimization of Eq. (2.10) and Eq. (2.11) with the experimental nonstoichiometry data. Results are summarized in Figure 2.7(a) and Figure 2.7(b) for CeO_2 and CZO_5, respectively. As expected, K_1 for CZO_5 is higher compared to that for CeO_2 because of its higher reduction extent. Additionally, the slope for CeO_2 is higher than that for CZO_5, indicating that its reduction enthalpy (at least at low δ where the reaction is dominated by K_1) is higher and consistent with Kuhn *et al.*⁸⁰. K_2 for CeO_2 is decreasing with increasing temperature meaning defect interactions become less predominant at higher temperatures. K_2 for CZO_5 does not show a meaningful trend and values are much smaller than

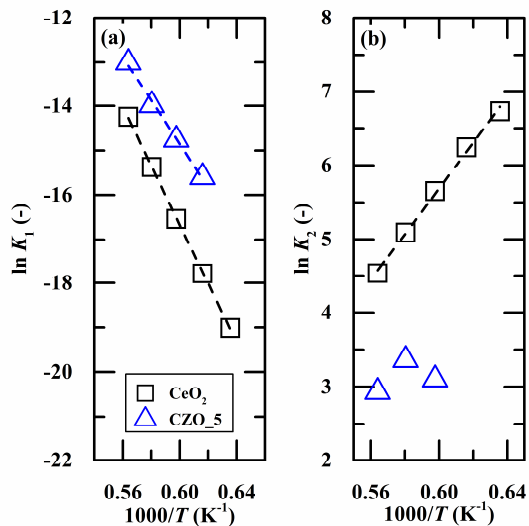


Figure 2.7. Equilibrium constants *versus* inverse temperature for CeO_2 and CZO_5 : (a) K_1 ; and (b) K_2 . Dashed lines indicate linear dependence of K_1 and K_2 on $1000/T$ ($R^2 > 0.99$).

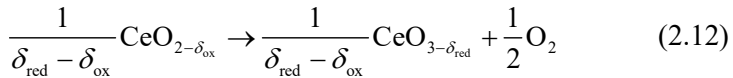
for CeO_2 because defect associations are probably not significant under the conditions investigated. In fact, in the case of CZO_5 at 1573 K, the best fit of K_2 is orders of magnitude below the fits at higher temperatures. These findings directly support the conclusions drawn from Figure 2.6, namely that a single isolated defect model appears to adequately describe the defect chemistry of CZO_5 , whereas electron-vacancy associations should be additionally taken into account in the case of CeO_2 . By fitting K_1 and K_2 over all experimental data, indicated by the lines in Figure 2.6(a) and (b), it can be seen that the agreement is very good. When including both defect models, the RMS deviations of the fitted $\log p_{\text{O}_2}$ (*c.f.* Figure 2.6) are 0.013 and 0.005 in the case of CeO_2 and CZO_5 , respectively. Both deviations are less than the uncertainty in the p_{O_2} setting, equal to 0.017. Considering only the isolated defect model (Eq. (2.2)) the RMS deviations are 0.094 for CeO_2 and 0.038 for CZO_5 . This reflects that defect associations are more important

in the case of CeO_2 than in the case of CZO_5 . The improvement in the RMS deviation for CZO_5 when including electron-vacancy associations may rather be a result of having an additional fitting parameter than having a more adequate physical model (*c.f.* trend of K_2 for CZO_5 in Figure 2.7(b)).

Based on computational investigations, Yang *et al.*⁹⁹ concluded that an oxygen vacancy is most likely created close to a Zr^{4+} dopant which might serve as nucleation center for vacancy clustering. Based on these results, Kuhn *et al.*⁸⁰ proposed that the considerably smaller Zr^{4+} , compared with Ce^{4+} , prefers a 7-fold coordination (instead of 8-fold) with oxygen which can be achieved if an oxygen vacancy is created next to the smaller Zr^{4+} cation. Therefore, $(\text{Zr}_{\text{Ce}}^{\times} \text{V}_{\text{O}}^{\cdot\cdot})^{\cdot}$ instead of $(\text{Ce}'_{\text{Ce}} \text{V}_{\text{O}}^{\cdot\cdot} \text{Ce}'_{\text{Ce}})^{\times}$ associations were also tested, but this did not improve the isolated defect model within the δ -range investigated.

2.4 Thermodynamic properties

Assuming unity activity for the solid and ideal gas behavior for O_2 , the standard partial molar Gibbs free energy, equivalent to the Gibbs free energy change of an infinitesimal reaction of Eq. (2.12), can be written as shown in Eq. (2.13).⁸⁵



$$\Delta \bar{g}_{\text{O}}^{\circ}(\delta, T) = -\frac{1}{2} RT \ln(p_{\text{O}_2} / p^{\circ}) \quad (2.13)$$

$\Delta \bar{g}_{\text{O}}^{\circ}$ can be additionally related to the standard partial molar enthalpy ($\Delta \bar{h}_{\text{O}}^{\circ}$) and entropy ($\Delta \bar{s}_{\text{O}}^{\circ}$) according to

$$\Delta \bar{g}_{\text{O}}^{\circ} = \Delta \bar{h}_{\text{O}}^{\circ} - T \Delta \bar{s}_{\text{O}}^{\circ} \quad (2.14)$$

By combining Eq.(2.13) and (2.14) and assuming temperature independent partial molar enthalpy and entropy, $\Delta\bar{h}_O^\circ$ and $\Delta\bar{s}_O^\circ$ as a function of δ (defined per one mole of oxygen vacancies created in the lattice or equivalent to half a mole of O_2 released to the surrounding gas atmosphere) are obtained by determining the slope and intercept of $-\ln(p_{O_2}/p^\circ)$ versus $1/T$ for a constant δ ,

$$-\ln\left(p_{O_2} / p^\circ\right) = \frac{2\Delta\bar{h}_O^\circ}{RT} - \frac{2\Delta\bar{s}_O^\circ}{R} \Bigg|_{\delta=\text{const.}} \quad (2.15)$$

Constant δ values are obtained by interpolating the defect models within the temperature range investigated (1573 K to 1773 K) and a slightly extrapolated p_{O_2} range ($\pm 20\%$ of the measured $-\log p_{O_2}$ range). Results of $\Delta\bar{h}_O^\circ$ and $\Delta\bar{s}_O^\circ$ versus δ are shown in Figure 2.8 and Figure 2.9, respectively, for CeO_2 (open squares) and CZO_5 (open triangles) (measurements from this work). For reference we have included CeO_2 data of Panlener *et al.*⁶⁴, Campserveux *et al.*⁸³, Bevan *et al.*⁶⁵ and Sørensen⁸². Additionally, measurements of CZO_5 by Kuhn *et al.*⁸⁰ and Hao *et al.*⁴⁹ are indicated by closed and crossed triangles, respectively. Measurements of 20 mol% Zr^{4+} doped CeO_2 (CZO_20) by Kuhn *et al.*⁸⁰ and Hao *et al.*⁴⁹ are indicated by closed circles and crossed circles, respectively. In general, it can be observed that $\Delta\bar{h}_O^\circ$ values decrease with increasing dopant concentration. This is expected due to the ease with which Zr^{4+} doped ceria reduces compared to pure ceria. Towards higher δ , the $\Delta\bar{h}_O^\circ$ values are in good agreement with literature data of CeO_2 ^{64, 65, 82, 83} and CZO_5^{49, 80}. However, at lower δ , they deviate. The same trend can be observed for $\Delta\bar{s}_O^\circ$. Deviations can be attributed primarily to different measurement temperatures and to a lesser extent to differences in nonstoichiometry measurements. For example, the literature data shown in Figure 2.8 and Figure 2.9 were calculated based on measurements below 1573 K^{65, 80, 82, 83} or as an average of measurements at

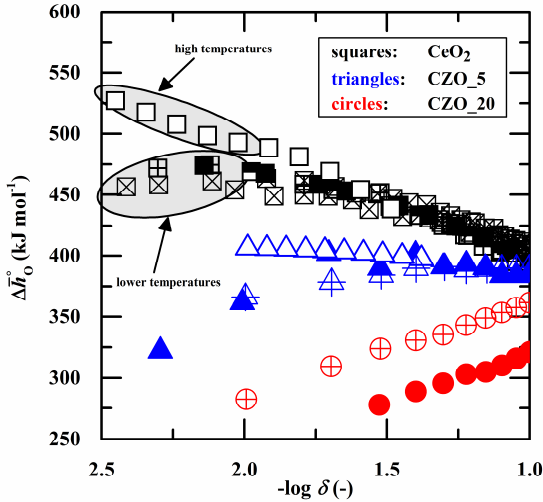


Figure 2.8. Partial molar enthalpy $\Delta \bar{h}_0^\circ$ of CeO_2 (open squares) and CZO_5 (open triangles) as a function of δ and a comparison to literature data of CeO_2 (Panlener *et al.*⁶⁴; closed squares, Campserveux *et al.*⁸³; diagonally crossed squares, Bevan *et al.*⁶⁵; half closed squares, Sørensen⁸²; crossed squares), CZO_5 (Kuhn *et al.*⁸⁰; closed triangles, Hao *et al.*⁴⁹; crossed triangles) and CZO_{20} (Kuhn *et al.*⁸⁰; closed circles, Hao *et al.*⁴⁹; crossed circles).

higher (>1573 K) and lower temperatures (<1573 K),^{49, 64} whereas values of this work are based on measurements only above 1573 K. Although it is often assumed that $\Delta \bar{h}_0^\circ$ and $\Delta \bar{g}_0^\circ$ are independent of temperature, this simplifying assumption is not always valid. For example, a temperature dependence of $\Delta \bar{h}_0^\circ$ is observed for the case of CeO_2 where two reactions dictate the defect chemistry. The degree of dependence varies in accordance with the magnitude of K_2 in regards to K_1 . Sørensen⁸² has showed that the slope of $\Delta \bar{g}_0^\circ$ vs. T (see Eq.(2.14)) is constant at $T < 1623$ K and $\delta < 0.08$, but decreases at higher temperatures due to the formation of sub-phases. The more negative $\Delta \bar{h}_0^\circ$ values at low δ from this work are in agreement with Sørensen⁸². Deviations in the measurements of CZO_5 can be additionally attributed to differences in Zr^{4+} dopant concentrations. For example, in this

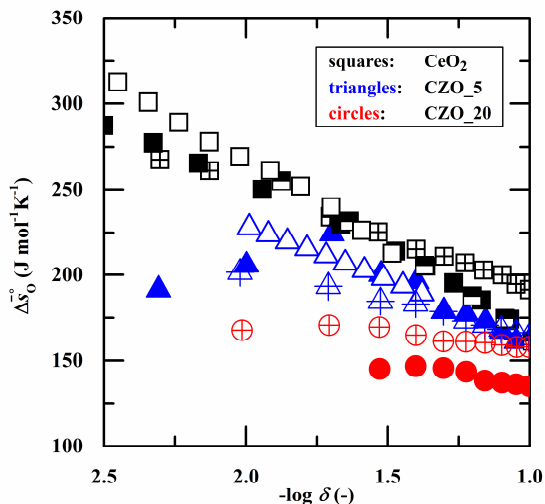


Figure 2.9. Partial molar entropy $\Delta\bar{s}_0^\circ$ of CeO_2 (open squares) and CZO_5 (open triangles) as a function of δ and a comparison to literature data of CeO_2 (Panlener *et al.*⁶⁴: closed squares, Bevan *et al.*⁶⁵: half closed squares, Sørensen⁸²: crossed squares), CZO_5 (Kuhn *et al.*⁸⁰: closed triangles, Hao *et al.*⁴⁹: crossed triangles) and CZO_{20} (Kuhn *et al.*⁸⁰: closed circles, Hao *et al.*⁴⁹: crossed circles).

work the dopant concentration is 4.5 mol% compared to 5.2 mol% in the work of Hao *et al.*⁴⁹.

The standard partial molar Gibbs free energy $\Delta\bar{g}_0^\circ$ as a function of T and δ was calculated from $\Delta\bar{h}_0^\circ$ and $\Delta\bar{s}_0^\circ$ values according to Eq.(2.14), where it was assumed that $\Delta\bar{h}_0^\circ$ and $\Delta\bar{s}_0^\circ$ are independent of T . $\Delta\bar{g}_0^\circ$ of the ceria, CZO_5 and CZO_{20} are shown in Figure 2.10 for $\delta = 0.05$, relevant for the metal oxide reduction reaction, and negative $\Delta\bar{g}_0^\circ$ for $\delta = 0.01$, relevant for the oxidation reaction with H_2O or CO_2 . Dashed lines represent the Gibbs free energy change of H_2 oxidation: $\text{H}_2 + 0.5\text{O}_2 = \text{H}_2\text{O}$ ($-\Delta_r G_{\text{H}_2\text{O}}^\circ$, green) and of CO oxidation: $\text{CO} + 0.5\text{O}_2 = \text{CO}_2$ ($-\Delta_r G_{\text{CO}_2}^\circ$, orange), obtained from NIST-JANAF thermochemical tables. The reduction reaction of the metal oxide is at equilibrium at $p_{\text{O}_2} = 1$ bar and $\delta = 0.05$ at the temperature where

$\Delta\bar{g}_O^\circ(\delta=0.05)=0$. The oxidation with $\text{H}_2\text{O}/\text{CO}_2$ to $\delta = 0.01$ is thermodynamically favorable at temperatures where $-\Delta\bar{g}_O^\circ(\delta=0.01)=-\Delta_r G_{\text{H}_2\text{O}}^\circ$ or $-\Delta_r G_{\text{CO}_2}^\circ$, respectively. From Figure 2.10 it can be concluded that at $p_{\text{O}_2} = 1$ bar, CZO_20 reduction to $\delta = 0.05$ is favorable at $T = 2075$ K and at even higher temperatures for CZO_5 ($T = 2165$ K) and CeO_2 ($T = 2175$ K), respectively. At lower temperatures, where $\Delta\bar{g}_O^\circ > 0$, reduction would only proceed if additional work is performed to the system, e.g. lowering p_{O_2} by vacuum pumping or flushing with inert gas. The oxidation of CZO_20 with H_2O and CO_2 to $\delta = 0.01$ is not favorable at $T > 400$ K, whereas the oxidation of CZO_5 with H_2O and CO_2 is favorable

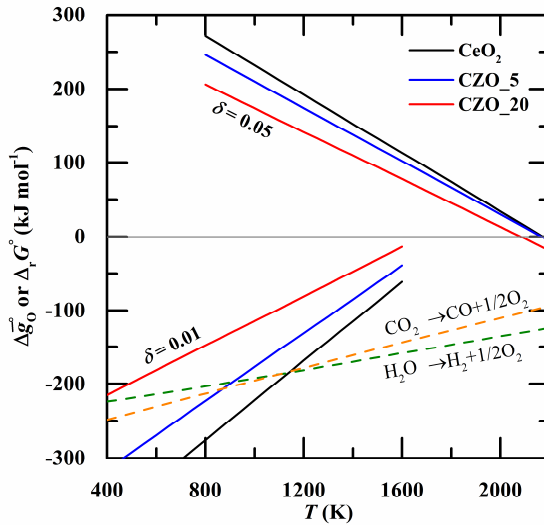
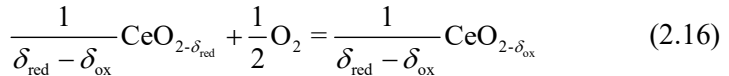


Figure 2.10. Standard partial molar Gibbs free energy $\Delta\bar{g}_O^\circ$ of CeO_2 , CZO_5 and CZO_20 for $\delta = 0.05$, relevant for the reduction, and negative $\Delta\bar{g}_O^\circ$ for $\delta = 0.01$, relevant for the oxidation reaction. Dashed lines represent the Gibbs free energy change of the H_2 oxidation reaction: $\text{H}_2 + 0.5\text{O}_2 = \text{H}_2\text{O}$ ($-\Delta_r G_{\text{H}_2\text{O}}^\circ$, green) and of the CO oxidation reaction: $\text{CO} + 0.5\text{O}_2 = \text{CO}_2$ ($-\Delta_r G_{\text{CO}_2}^\circ$, orange). The metal oxide reduction reaction is at equilibrium in 1 bar p_{O_2} at $\delta = 0.05$ at the temperature where $\Delta\bar{g}_O^\circ(\delta = 0.05) = 0$. The oxidation with $\text{H}_2\text{O}/\text{CO}_2$ to $\delta = 0.01$ is thermodynamically favorable at temperatures where $-\Delta\bar{g}_O^\circ(\delta = 0.01) = -\Delta_r G_{\text{H}_2\text{O}}^\circ$ or $-\Delta_r G_{\text{CO}_2}^\circ$, respectively.

at 910 K and 870 K, respectively. The oxidation of ceria to $\delta = 0.01$ with H_2O and CO_2 is favorable at much higher temperature ($T = 1050$ K) compared to the oxidation of the Zr^{4+} doped ceria. At $T = 1050$ K, the oxidation with H_2O and CO_2 is identically favorable. The favorable oxidation thermodynamics of ceria compared to the Zr^{4+} doped ceria can be explained by its relatively high $\Delta\bar{h}_0^\circ$ and $\Delta\bar{s}_0^\circ$ values. The high $\Delta\bar{s}_0^\circ$ results in a relatively high $\Delta\bar{g}_0^\circ$ value at lower temperatures and a relatively low $\Delta\bar{g}_0^\circ$ at higher temperatures.

2.5 Water splitting

This work focuses on H_2O splitting, but the thermodynamics of CO_2 splitting are qualitatively very similar and give similar insights into the performance of candidate redox materials.^{63, 85} Thermodynamically, the water splitting reaction can be described by the simultaneous oxidation of the perovskite with O_2 and the splitting of H_2O into H_2 and $1/2\text{O}_2$, as shown by Eq.(2.16) and (2.17), respectively.



The chemical equilibrium is described by the two simultaneous reaction equilibria

$$\Delta_r G_{\text{ox}}^\circ(\delta_{\text{ox}}, T_{\text{ox}}) = -\Delta\bar{g}_0^\circ(\delta_{\text{ox}}, T_{\text{ox}}) = \frac{1}{2} RT_{\text{ox}} \ln(p_{\text{O}_2} / p^\circ) \quad (2.18)$$

$$\Delta_r G_{\text{H}_2\text{O}}^\circ(T_{\text{ox}}) = -RT_{\text{ox}} \ln K_{\text{W}} = -RT_{\text{ox}} \ln \left(\frac{p_{\text{H}_2} p_{\text{O}_2}^{1/2}}{p_{\text{H}_2\text{O}}} p^{\circ-1/2} \right) \quad (2.19)$$

where p_{O_2} , p_{H_2} and p_{H_2O} denote the equilibrium partial pressures of O_2 , H_2 and H_2O , respectively and K_w is the reaction equilibrium constant of the H_2 oxidation reaction. By combining Eq.(2.18) and (2.19), and assuming negligible amounts of H_2 from direct thermolysis of H_2O , closed-system equilibrium H_2 yields can be calculated according to:

$$\Delta \bar{g}_O^\circ(\delta_{ox} = \delta_{red} - n_{H_2}) = RT \ln \left(\frac{K_w (n_{H_2O,i} - n_{H_2})}{n_{H_2}} \right) \quad (2.20)$$

where n_{H_2} is the molar amount of H_2 produced at equilibrium per mole oxide, and $n_{H_2O,i}$ is the initial molar amount of H_2O in the system per mole oxide. n_{H_2} is obtained by iteratively solving Eq.(2.20) and is shown in Figure 2.11 *versus* temperature for CeO_2 (black), CZO_5 (blue), and CZO_20 (red). $n_{H_2O,i}$ is set equal to δ_{red} (solid lines) and $100 \times \delta_{red}$ (dashed lines), where δ_{red} is the nonstoichiometry achieved after reduction at $T_{red} = 1773$ K and $p_{O_2} = 2.3 \times 10^{-4}$ bar. The calculations reaffirm that the oxidation with H_2O becomes thermodynamically less favorable with increasing Zr^{4+} dopant concentrations. For example, for $n_{H_2O,i} = \delta_{red}$, maximum n_{H_2} is reached at $T \leq 900$ K for CeO_2 , $T \leq 700$ K for CZO_5 , and $T < 400$ K for CZO_20 . If $n_{H_2O,i}$ is increased by a factor of hundred, these oxides can be oxidized at higher temperatures but at the expense of heating excess H_2O . In this case, maximum n_{H_2} is obtained at as high as 1200 K for CeO_2 , 1100 K for CZO_5 , and 500 K for CZO_20 . For CZO_20 , n_{H_2} is only shown up to 0.042 moles because $\Delta \bar{h}_O^\circ$ and $\Delta \bar{s}_O^\circ$ are not available at $\delta \leq 0.03$. Because $\Delta \bar{h}_O^\circ$ and $\Delta \bar{s}_O^\circ$ of CeO_2 and CZO_5 are not measured over the whole range $\delta = 0$ to 0.1, they are assumed to be constant for low δ and taken as the average from literature data^{64, 65, 80, 82, 83} for high δ .

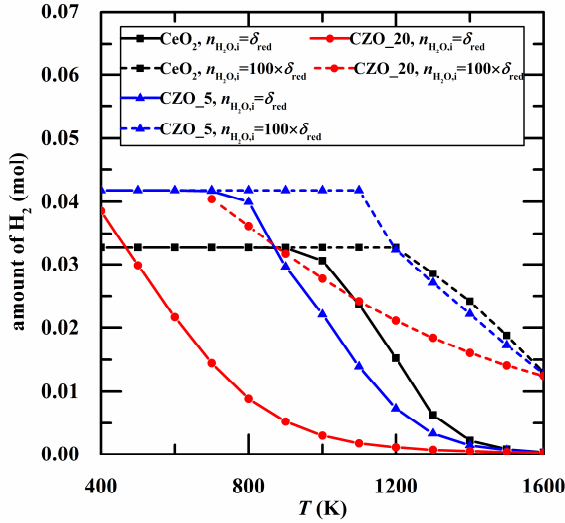


Figure 2.11. Molar amount of H_2 produced by oxidation of CeO_2 (black), CZO_5 (blue) and CZO_20 (red) with H_2O produced by oxidation assuming $n_{H_2O,i} = \delta_{red}$ (solid lines) and $100 \times \delta_{red}$ (dashed lines) where δ_{red} is the nonstoichiometry achieved after reduction at $T_{red} = 1773$ K and $p_{O_2} = 2.3 \times 10^{-4}$ bar ($\delta_{red} = 0.0328$ for CeO_2 , $\delta_{red} = 0.0417$ for CZO_5, and $\delta_{red} = 0.0725$ for CZO_20).

2.6 Efficiency analysis

The theoretical solar-to-fuel energy conversion efficiency ($\eta_{solar-to-fuel}$) for the case of hydrogen production is defined as:

$$\eta_{solar-to-fuel} = \frac{HHV_{H_2} n_{H_2}}{Q_{input,min}} \quad (2.21)$$

where $HHV_{H_2} = 285.5 \text{ kJ mol}^{-1}$ is the higher heating value of H_2 . $Q_{input,min}$ is the minimum input of energy required to produce n_{H_2} and comprises the solar process heat for driving the reduction, for heating the redox material from

T_{ox} to T_{red} , and for generating steam at T_{ox} , as well as the equivalent minimum work to drive the reduction for the case of $\Delta g_{\text{red}} > 0$, defined as:

$$\Delta g_{\text{red}} = \frac{\int_{\delta_{\text{red}}}^{\delta_{\text{ox}}} \Delta \bar{g}_{\text{O}}^{\circ} d\delta}{\delta_{\text{red}} - \delta_{\text{ox}}} \quad (2.22)$$

Assuming no heat recuperation between the redox steps,

$$Q_{\text{input,min}} = \frac{1}{\eta_{\text{absorption}}} \cdot \left[\Delta h_{\text{red}} (\delta_{\text{red}} - \delta_{\text{ox}}) + \int_{T_{\text{ox}}}^{T_{\text{red}}} c_p dT + \Delta h_{\text{H}_2\text{O}} \Big|_{298\text{K} \rightarrow T_{\text{ox}}} n_{\text{H}_2\text{O},i} + \frac{\Delta g_{\text{red}}}{\eta_{\text{Carnot}}} (\delta_{\text{red}} - \delta_{\text{ox}}) \right] \quad (2.23)$$

where Δh_{red} is the enthalpy change of the reduction (Eq.(2.24)),

$$\Delta h_{\text{red}} = \frac{\int_{\delta_{\text{ox}}}^{\delta_{\text{red}}} \Delta \bar{h}_{\text{O}}^{\circ} d\delta}{\delta_{\text{red}} - \delta_{\text{ox}}} \quad (2.24)$$

$\Delta h_{\text{H}_2\text{O}}|_{298\text{K} \rightarrow T_{\text{ox}}}$ is the thermal energy required to heat H_2O from ambient temperature to T_{ox} (obtained from NIST-JANAF tables), $n_{\text{H}_2\text{O},i}$ is the initial molar amount of H_2O determined by Eq.(2.20), and c_p is the specific heat capacity of pure ceria.¹⁰⁰ The excess H_2O needed is calculated for n_{H_2} approaching δ_{red} . Note that the maximum $\eta_{\text{solar-to-fuel}}$ may not be attained by completely re-oxidizing the material, as shown by Chueh *et al.*³⁹ and Furler *et al.*⁴⁰, but an overall optimization routine is outside the scope of this work. Due to the low dopant concentration of Zr^{4+} , c_p of CZO_5 and CZO_{20} are assumed to be identical to that of pure CeO_2 . $Q_{\text{input,min}}$ is assumed to be delivered by concentrated solar energy. The solar absorption efficiency ($\eta_{\text{absorption}}$) for a blackbody cavity-receiver is given by:¹¹

$$\eta_{\text{absorption}} = 1 - \frac{\sigma T_{\text{red}}^4}{IC} \quad (2.25)$$

where σ is the Stefan-Boltzmann constant, $I = 1 \text{ kWm}^{-2}$ the direct normal irradiation (DNI) and $C = 2000$ the solar flux concentration ratio. The fourth term in Eq.(2.23) is the minimum work required to drive the reduction at conditions for which $\Delta g_{\text{red}} > 0$; when $\Delta g_{\text{red}} \leq 0$ this term is omitted. η_{Carnot} is the efficiency of an ideal heat engine converting solar heat at T_{red} to work.¹¹

A contour plot of $\eta_{\text{solar-to-fuel}}$ shown as a function of δ_{red} and T_{ox} is shown in Figure 2.12 for CeO_2 (a) and CZO_5 (b), respectively. $p_{\text{O}_2} = 10^{-6}$ bar is assumed for the efficiency calculations resulting in reduction temperatures of 1744 K for CeO_2 and 1741 K for CZO_5 needed to reach $\delta_{\text{red}} = 0.1$ and 1564 K and 1510 K respectively to reach $\delta_{\text{red}} = 0.02$. It is shown that the maximum efficiency for CeO_2 is slightly higher compared to CZO_5 . $\eta_{\text{solar-to-fuel}}$ is slightly greater than 17% at $\delta_{\text{red}} = 0.1$ ($T_{\text{ox}} = 1050$ K) for CeO_2 and slightly greater than 16% at $\delta_{\text{red}} = 0.1$ ($T_{\text{ox}} = 880$ K) for CZO_5 . Simply stated, the energy savings during reduction of CZO_5 cannot compensate the additional energy inputs due to the less favorable re-oxidation with H_2O (lower T_{ox} and/or higher $n_{\text{H}_2\text{O},i}$ compared to CeO_2). In general $\eta_{\text{solar-to-fuel}}$ rapidly decreases towards higher T_{ox} as the re-oxidation with H_2O gets thermodynamically less favorable and an increasing amount of excess steam has to be heated in order to fully oxidize the reduced material. Towards lower T_{ox} , $\eta_{\text{solar-to-fuel}}$ decreases as the temperature difference between oxidation and reduction increases and towards lower δ_{red} it decreases as the amount of H_2 produced (equal to δ_{red}) decreases compared to the sensible energy required to heat the oxide. Qualitatively these results are in agreement with calculations reported in literature for pure ceria,^{50, 63, 77} and indicate the tradeoffs between a redox cycle driven by temperature swing and an isothermal redox cycle driven by pressure swing. Heat recovery, not accounted for in Figure 2.8, can significantly boost $\eta_{\text{solar-to-fuel}}$.⁶³ When heat

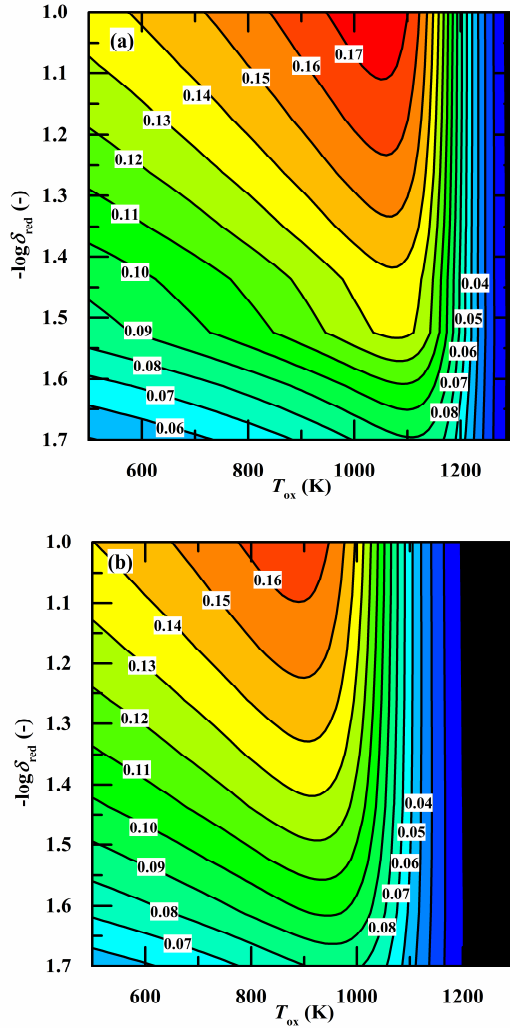


Figure 2.12. $\eta_{\text{solar-to-fuel}}$ shown as contour lines for CeO_2 (a) and CZO_5 (b) as a function of δ_{red} and T_{ox} assuming reduction at $p_{\text{O}_2} = 10^{-6}$ bar and subsequent complete re-oxidation with steam.

recovery is used for generating steam at T_{ox} , $\eta_{\text{solar-to-fuel}}$ peaks at 19% for CeO_2 and 18% for CZO_5 . If, in addition, heat recovery is used to heat the redox material from T_{ox} to T_{red} , $\eta_{\text{solar-to-fuel}}$ peaks at 41% and 44% for CeO_2 and CZO_5 , respectively. Results for CZO_{20} are not shown because thermodynamic data are not available at $\delta \leq 0.03$ and also because calculations always predict maximum $\eta_{\text{solar-to-fuel}}$ at lowest T_{ox} (400 K) and highest δ_{red} (0.1).

Maximum $\eta_{\text{solar-to-fuel}}$ as a function of p_{O_2} is shown in Figure 2.13 for CeO_2 (solid lines), CZO_5 (dashed lines) and CZO_{20} (dotted lines) where $\delta_{\text{red}} = 0.1$ (a) and $\delta_{\text{red}} = 0.05$ (b). Additionally, T_{red} where maximum $\eta_{\text{solar-to-fuel}}$ is obtained is shown in Figure 2.13. Estimates of T_{red} of CZO_{20} were

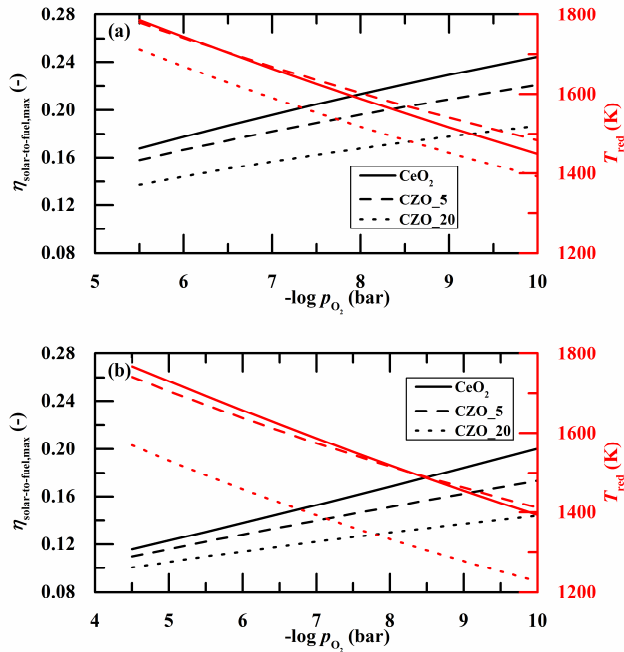


Figure 2.13. Maximum $\eta_{\text{solar-to-fuel}}$ and T_{red} versus p_{O_2} for CeO_2 (solid lines), CZO_5 (dashed lines) and CZO_{20} (dotted lines) assuming $\delta_{\text{red}} = 0.1$ (a) and $\delta_{\text{red}} = 0.05$ (b).

calculated according to the methodology described by Yang *et al.*⁵² using the thermodynamic data of Kuhn *et al.*⁸⁰. It is observed that CeO₂ shows the highest $\eta_{\text{solar-to-fuel}}$ under all conditions investigated and CZO_20 shows the lowest $\eta_{\text{solar-to-fuel}}$. Although CZO_20 reduces at substantially lower temperatures compared to CZO_5 and CeO₂, the lower energy input during reduction cannot compensate the higher energy input during oxidation with H₂O. In general, $\eta_{\text{solar-to-fuel}}$ increases with decreasing p_{O_2} , meaning less energy is required to reduce the oxide by lowering p_{O_2} compared to increasing T_{red} .

2.7 Conclusions

Oxygen nonstoichiometry measurements of Zr⁴⁺ doped ceria at elevated temperatures presented in this work are largely in agreement with the trends observed in works performed at lower temperatures (<1573 K), namely: for a given T_{red} and p_{O_2} the reduction extent increases and the reduction enthalpy decreases with increasing Zr⁴⁺ concentration. Extracted thermodynamic properties are also largely in agreement with previous data, but they deviate at low nonstoichiometries especially for the case of pure ceria. This is likely due to the fact that they are slightly temperature dependent, especially at higher temperatures (>1623 K) where different sub-phases can be expected.⁸² Interestingly, in the case of 5 mol% Zr⁴⁺ doped ceria, a single defect model is capable of describing the nonstoichiometry data over the entire measurement range ($\delta = 0.01$ to 0.04) and therefore the thermodynamic properties can be assumed to be independent of temperature. This is an important distinction when extrapolating nonstoichiometries to conditions that have not yet been measured experimentally.⁵² Although the nonstoichiometry increases with increasing Zr⁴⁺ dopant concentration, oxidation with steam becomes thermodynamically less favorable and has to be conducted at lower temperatures or with excess amounts of steam. This

ultimately results in lower theoretical solar-to-fuel energy conversion efficiencies compared to that for pure ceria. Therefore, when screening potential redox materials, it is important to consider both steps of the cycle, i.e. the materials ability to release lattice oxygen and its oxidation potential with H_2O and CO_2 . It was assumed that reduction and oxidation are driven to completion, but maximum efficiencies may be found at lower extents. In general, when we compare with the thermodynamic properties of pure ceria, a relatively lower partial molar enthalpy and a relatively higher partial molar entropy are desired, resulting in $\Delta\bar{g}_\text{O}^- = 0$ at lower T_red and $-\Delta\bar{g}_\text{O}^- = -\Delta_\text{r}G_{\text{H}_2\text{O}}^\circ$ at higher T_ox , which in turn yields a smaller temperature swing between the redox steps. Besides thermodynamic aspects, fast reaction kinetics and long term chemical and morphological stability are obviously essential.

Chapter 3

Thermodynamic characterization of La-Mn based perovskites²

This chapter builds up on the recent work of Cooper *et al.*⁸⁵ and reports detailed oxygen nonstoichiometry measurements of $\text{La}_{0.6}\text{A}_{0.4}\text{Mn}_{1-y}\text{Al}_y\text{O}_3$ ($A = \text{Ca}, \text{Sr}$ and $y = 0, 0.4$) over a wide temperature range $T = 1573 \text{ K} - 1773 \text{ K}$ and oxygen partial pressure range $p_{\text{O}_2} = 4.5066 \times 10^{-2} \text{ bar} - 9.9 \times 10^{-5} \text{ bar}$. The refinement of the nonstoichiometry measurements allows the development of more appropriate defect models to describe the defect chemical equilibria and to extract finer trends in partial molar thermodynamic properties ($\Delta \bar{h}_{\text{O}}^\circ$, $\Delta \bar{s}_{\text{O}}^\circ$, $\Delta \bar{g}_{\text{O}}^\circ$). From such data, equilibrium hydrogen yields are determined and the potential of these lanthanum-manganites to be used as reactive intermediates in solar thermochemical redox cycles is evaluated.

² Material from this chapter has been published in: M. Takacs, M. Hoes, M. Caduff, T. Cooper, J.R. Scheffe and A. Steinfeld, "Oxygen nonstoichiometry, defect equilibria, and thermodynamic characterization of LaMnO_3 perovskites with Ca/Sr A-site and Al B-site doping", *Acta Materialia*, vol. 103, pp. 700-710, 2016

3.1 Experimental section

3.1.1 Synthesis technique and sample characterization

$\text{La}_{0.6}\text{Sr}_{0.4}\text{MnO}_3$ (LSM40), $\text{La}_{0.6}\text{Ca}_{0.4}\text{MnO}_3$ (LCM40), $\text{La}_{0.6}\text{Sr}_{0.4}\text{Mn}_{0.6}\text{Al}_{0.4}\text{O}_3$ (LSMA) and $\text{La}_{0.6}\text{Ca}_{0.4}\text{Mn}_{0.6}\text{Al}_{0.4}\text{O}_3$ (LCMA) perovskite powders were synthesized by sol-gel method as described by Scheffe *et al.*⁴⁷. The corresponding metal nitrates (*c.f.* Table 3.1) and anhydrous citric acid (Sigma-Aldrich, catalog nr. 251275) in aqueous solution were used to carry out the synthesis. The ratio of the metal cations to the citric acid was 1:1.5. The aqueous solution was slowly heated up to 573 K to perform the pyrolysis. Afterwards, powders were calcined at 1273 K under air for 5 hours. Dense cylindrical pellets were obtained by uniaxially cold-pressing the powder at 5 tons followed by sintering at 1773 K under air atmosphere for 24 hours. The approximate dimensions after sintering were 6.4 - 6.9 mm diameter and 1 - 2 mm height and the mass of the pellets was ~250 mg (LSM40), ~290 mg

Table 3.1. Metal nitrates used for sample preparation.

Chemical	Formula	Manufacturer
Lanthanum (III) nitrate hexahydrate	$\text{La}(\text{NO}_3)_3 \cdot \text{H}_2\text{O}$	Sigma-Aldrich, catalog nr. 203548
Strontium nitrate	$\text{Sr}(\text{NO}_3)_2$	Sigma-Aldrich, catalog nr. 13914
Manganese (II) nitrate tetrahydrate	$\text{Mn}(\text{NO}_3)_2 \cdot 4\text{H}_2\text{O}$	Alfa Aesar, catalog nr. A18521
Aluminum nitrate nonahydrate	$\text{Al}(\text{NO}_3)_3 \cdot 9\text{H}_2\text{O}$	Alfa Aesar, catalog nr. 12360
Calcium nitrate tetrahydrate	$\text{Ca}(\text{NO}_3)_2 \cdot 4\text{H}_2\text{O}$	Alfa Aesar, catalog nr. A16645

(LCM40), ~150 mg (LSMA) and ~270 mg (LCMA).

Dopant concentrations were measured by inductively coupled plasma-atomic emission spectroscopy (ICP-OES) and deviated by less than 4% from their nominal composition for LSMA and LCMA, as shown in Table 3.2.

Table 3.2. ICP-OES analysis of $\text{La}_{0.6}\text{Sr}_{0.4}\text{Mn}_{0.6}\text{Al}_{0.4}\text{O}_3$ (LSMA) and $\text{La}_{0.6}\text{Ca}_{0.4}\text{Mn}_{0.6}\text{Al}_{0.4}\text{O}_3$ (LCMA) shown in mole fraction.

Component	$\text{La}_{0.6}\text{Sr}_{0.4}\text{Mn}_{0.6}\text{Al}_{0.4}\text{O}_3$ (LSMA)	$\text{La}_{0.6}\text{Ca}_{0.4}\text{Mn}_{0.6}\text{Al}_{0.4}\text{O}_3$ (LCMA)
Lanthanum	0.584	0.589
Strontium	0.414	-
Calcium	-	0.413
Manganese	0.612	0.604
Aluminum	0.394	0.390

Powder X-ray diffraction (XRD) was performed in the Bragg Brentano geometry using $\text{Cu K}\alpha$ radiation (Philips, PANalytical/X'Pert MPD/DY636, $\lambda = 1.5406 \text{ \AA}$, $2\Theta = 20\text{--}100^\circ$, $0.01^\circ \text{ s}^{-1}$ scan rate, 45 kV/20 mA output) and revealed a predominant perovskite phase for all the materials, as shown in Figure 3.1. Scanning electron microscopy (SEM) of the dense pellets was conducted on a TM-1000Microscope (Hitachi, 15 kV accelerating voltage). SEM images of the pressed and sintered pellets made from LSM40, LCM40, LSMA and LCMA are shown in Figure 3.2 and Figure 3.3, respectively. SEM images reveal a homogeneous grain structure for all the materials.

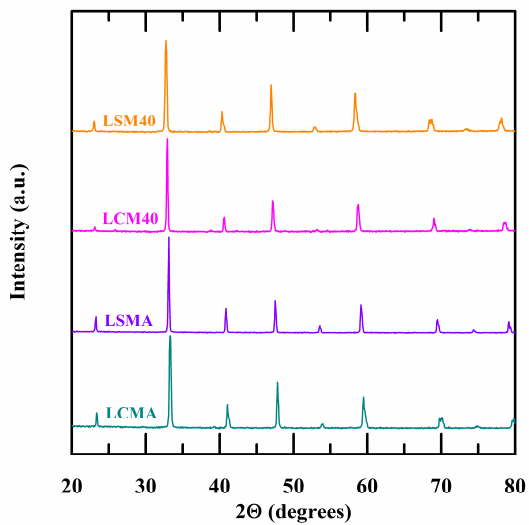
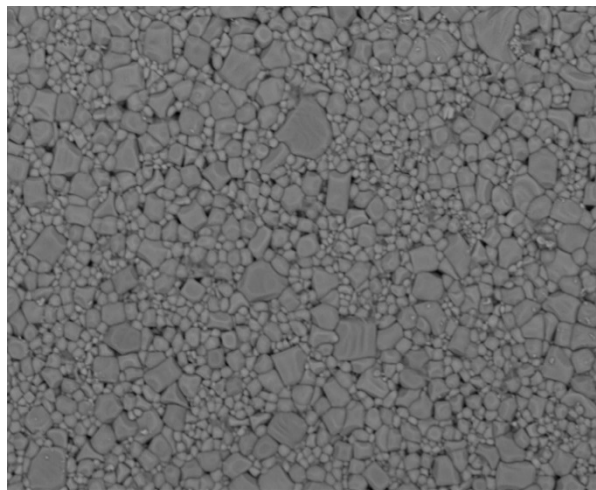
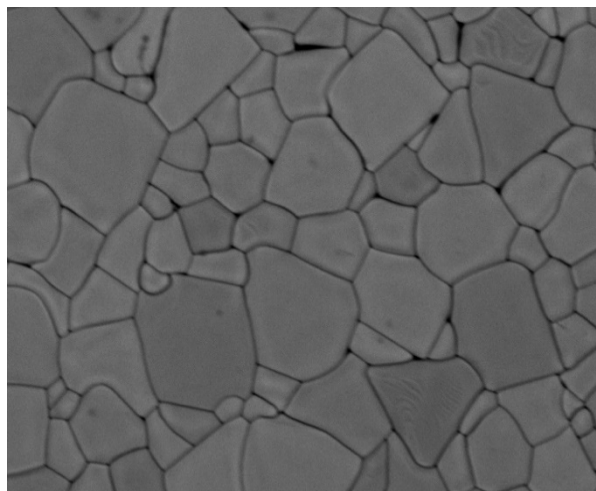


Figure 3.1. XRD patterns of LSM40, LCM40, LSMA and LCMA powder.



2015/01/15 D4.2 x1.8k 50 um



2014/11/19 D4.7 x1.8k 50 um

Figure 3.2. SEM images of the pressed and sintered LSM40 (top) and LCM40 (bottom) pellet.

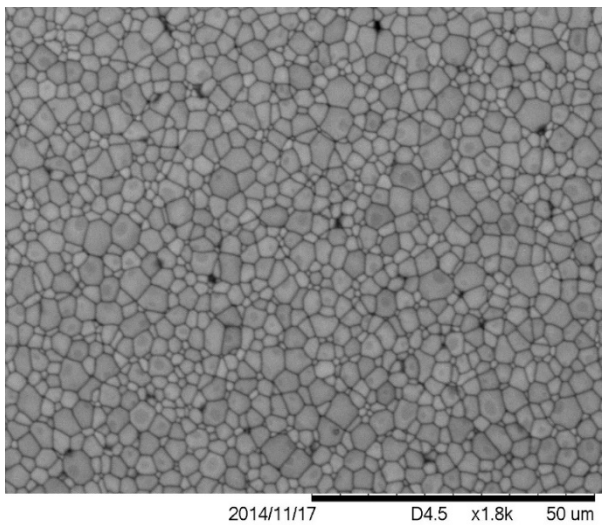
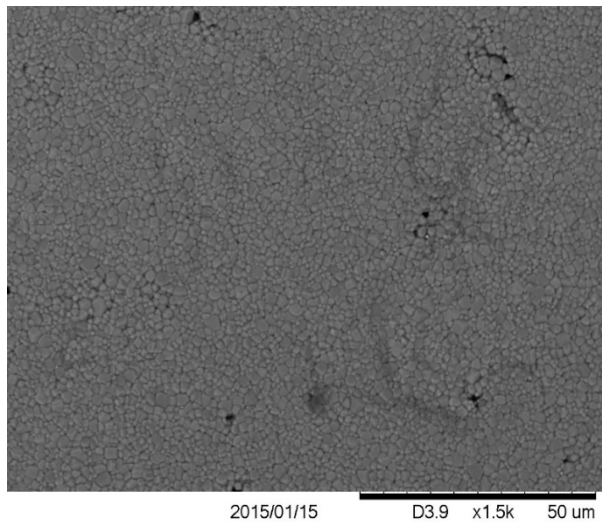


Figure 3.3. SEM images of the pressed and sintered LSMA (top) and LCMA(bottom) pellet.

3.1.2 Thermal analysis

Oxygen nonstoichiometry was measured using a thermogravimetric analyzer (TGA, Setaram Setsys Evolution). Pellets were suspended to the balance with a custom-made platinum hook (*cf.* Figure 2.4) to ensure good exposure to the purge gas and eliminate gas diffusion limitations. The p_{O_2} of the sweep gas was controlled by mixing Ar (Messer, Argon 4.6) with O₂/Ar mixtures (Messer, 5% O₂ 5.0 in Ar 5.0 and 0.1% O₂ 5.0 in Ar 5.0). Gases were mixed with electronic mass flow controllers (Brooks, Model 5850TR, accuracy $\pm 1\%$) with a constant total flow rate of 200 mL/min. The gas species and concentrations at the outlet were monitored by mass spectrometry (Pfeiffer Vacuum, OmniStar GSD 320). Temperature was varied between 1573 K and 1773 K and p_{O_2} between 4.5066×10^{-2} bar and 9.9×10^{-5} bar. In all measurements, the sample mass (m_s) was equilibrated at a constant T and p_{O_2} . Following each equilibrium measurement, the p_{O_2} was rapidly changed by adapting the O₂/Ar gas mixture, resulting in a temporal weight change of the sample due to evolving or uptaking of oxygen until a new equilibrium state was reached. To correct for buoyancy, blank runs were performed with inert Al₂O₃ sintered pellets of same dimensions.

3.2 Oxygen nonstoichiometry

The thermogravimetric measurements of LCM40, LSM40, LSMA and LCMA are shown in Figure 3.4(a) and (b). Figure 3.4(a) shows the reduction and oxidation runs within the higher p_{O_2} measurement range (4.5066×10^{-2} bar to 2.387×10^{-3} bar) whereas Figure 3.4(b) shows the runs within the lower p_{O_2} range (9.15×10^{-4} bar to 9.9×10^{-5} bar). The samples were heated to different set point temperatures followed by isothermal

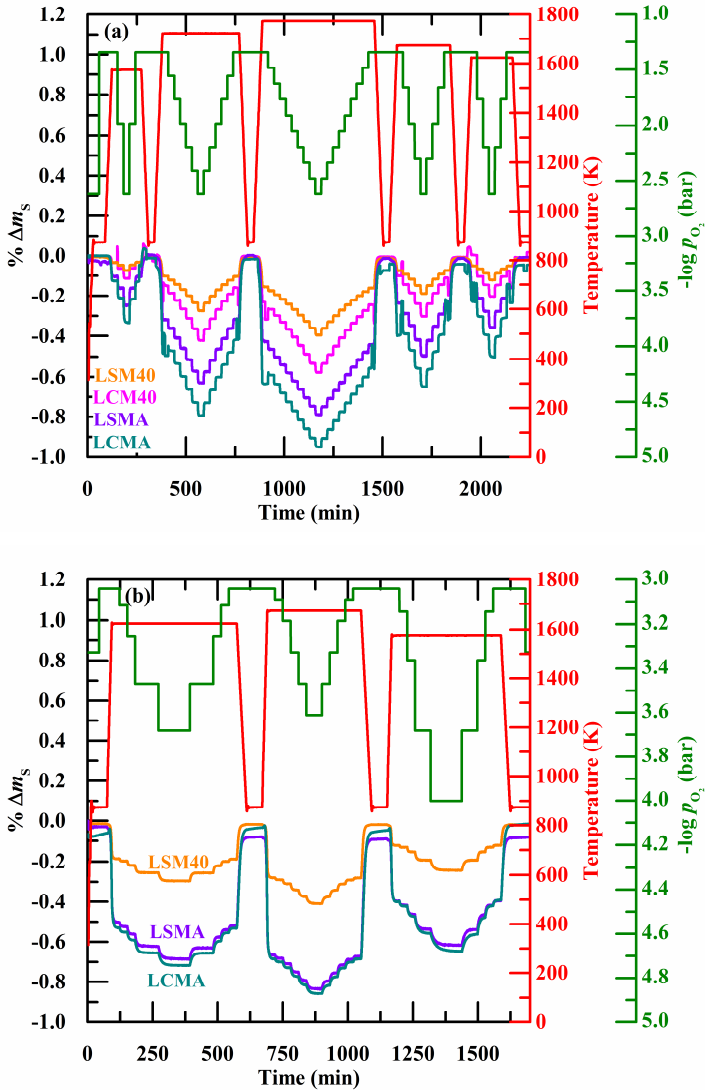


Figure 3.4. Percent mass change as a function of time for all reduction and oxidation runs of LCM40, LSM40, LSMA and LCMA for: (a) temperature range $T = 1573\text{-}1773$ K and O_2 partial pressure range $p_{\text{O}_2} = 4.5066 \times 10^{-2}\text{-}2.387 \times 10^{-3}$ bar; and (b) $T = 1573\text{-}1673$ K and $p_{\text{O}_2} = 9.15 \times 10^{-4}\text{-}9.9 \times 10^{-5}$ bar.

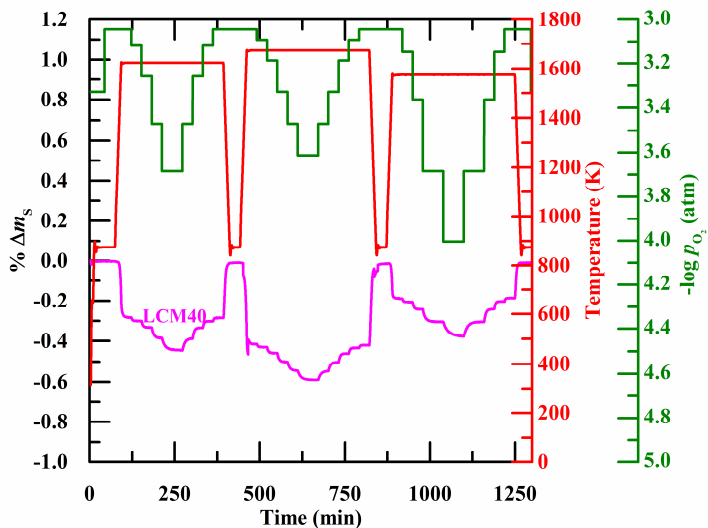


Figure 3.5. Percent mass change as a function of time for all reduction and oxidation runs of LCM40 for: $T = 1573\text{-}1673$ K and O_2 partial pressure range $p_{O_2} = 9.15 \times 10^{-4}\text{-}9.9 \times 10^{-5}$ bar.

reduction and oxidation by stepwise changing p_{O_2} . As seen, within the temperature and p_{O_2} range investigated, LCMA shows the highest reduction extents followed by LSMA, LCM40 and LSM40. The measurement of LCM40 within the lower p_{O_2} range is shown separately in Figure 3.5 because of different relaxation time scales. Oxygen nonstoichiometry δ is calculated according to:

$$\delta = \Delta m_s \cdot \frac{M_s}{M_o} \quad (3.1)$$

where Δm_s is the relative weight loss at equilibrium, M_s is the molar mass of the sample, and M_o the molar mass of atomic oxygen. Δm_s of the reduction and oxidation runs is calculated relative to the mass at $T = 873$ K before heating to the set point temperature and after cooling from the set point temperature, respectively. Measured $3 - \delta$ versus p_{O_2} for $T = 1573$

K to 1773 K is shown in Figure 3.6 for LSM40 (a), LCM40 (b) and in Figure 3.7 for LSMA (a), LCMA (b). Symbols indicate $3 - \delta$ values obtained from thermogravimetric (TG) analysis shown in Figure 3.4(a) and (b) and Figure 3.5. Dashed colored and solid black lines indicate defect models used to describe equilibrium data, presented in the next section. Error bars account for $\Delta m_S \neq 0$ at the stabilization temperature $T = 873$ K (*cf.* Δm_S of LSMA shown in Figure 3.4(b)). As seen in Figure 3.6 and Figure 3.7, δ is highest for LCMA followed by LSMA, LCM40 and LSM40, over the whole measurement range investigated. At $T = 1573$ K and at $p_{O_2} = 2.09 \times 10^{-4}$ bar, δ of LCMA is almost 100% higher than LCM40 whereas δ of LSMA is almost 150% higher than LSM40. At these conditions, LCMA releases about 20% more O_2 compared to LSMA (per mole of metal oxide). Compared to ceria⁶², higher reduction extents are obtained with all the four perovskites as seen in Figure 3.8, where the mass specific oxygen release n_{O_2}' is shown. For example, $n_{O_2}' = 0.15$ mol kg^{-1} is expected for ceria at $T = 1885$ K and $p_{O_2} = 10^{-3}$ bar, while LCMA is expected to reach the same n_{O_2}' but at 285 K lower temperatures. The higher reduction extent of LSMA compared to LSM40 is in agreement with measurements of McDaniel *et al.*⁵¹ and Cooper *et al.*⁸⁵. The higher reduction extents of the Ca-doped perovskites compared to the Sr-doped are in agreement with the study of Dey *et al.*⁵⁴, attributed to the smaller ionic radii of Ca^{2+} compared to Sr^{2+} .

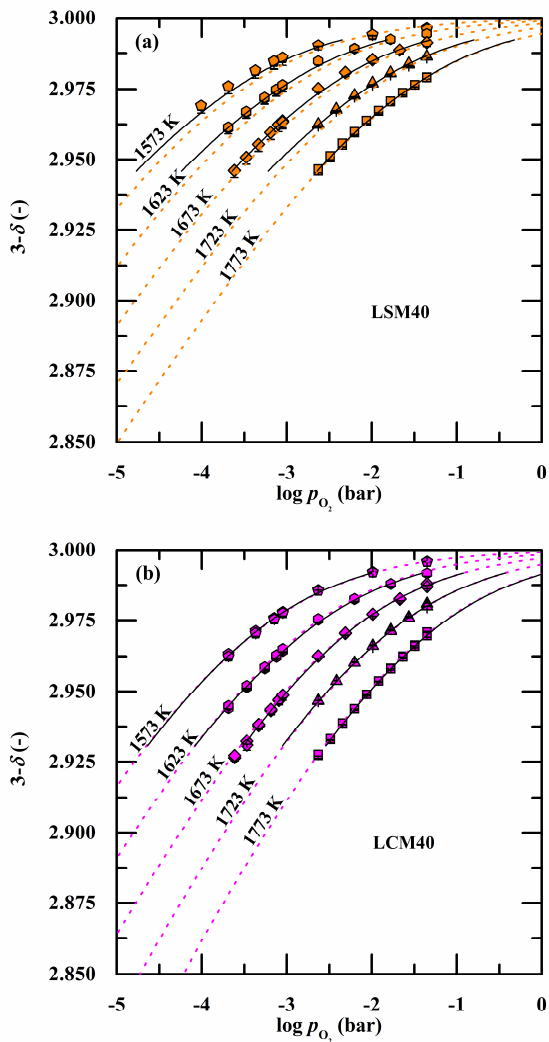


Figure 3.6. Measured oxygen nonstoichiometry (symbols) of LSM40 (a) and LCM40 (b) versus p_{O_2} for $T = 1573$ K to 1773 K. Colored dashed and black solid lines indicate defect models used to describe experimental results. Black solid lines are calculated based on individual defect equilibrium constants whereas the colored dashed lines are calculated by using the inverse temperature dependence of $\ln K_1$ and $\ln K_2$ (cf. Figure 3.9 and Eq.(3.11)).

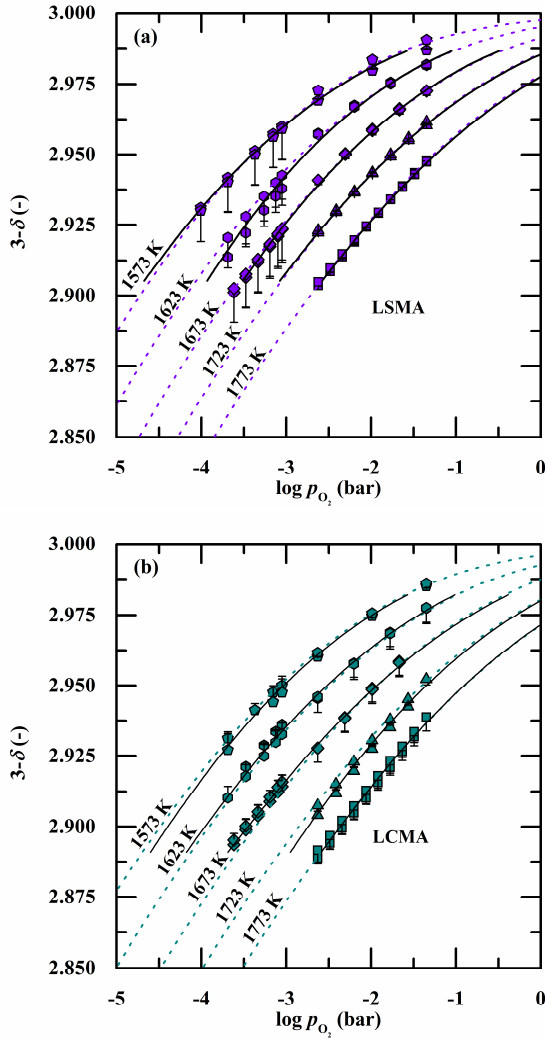


Figure 3.7. Measured oxygen nonstoichiometry (symbols) of LSMA (a) and LCMA (b) versus p_{O_2} for $T = 1573$ K to 1773 K. Colored dashed and black solid lines indicate defect models used to describe experimental results. Black solid lines are calculated based on individual defect equilibrium constants whereas the colored dashed lines are calculated by using the inverse temperature dependence of $\ln K_1$ and $\ln K_2$ (cf. Figure 3.9 and Eq.(3.11)).

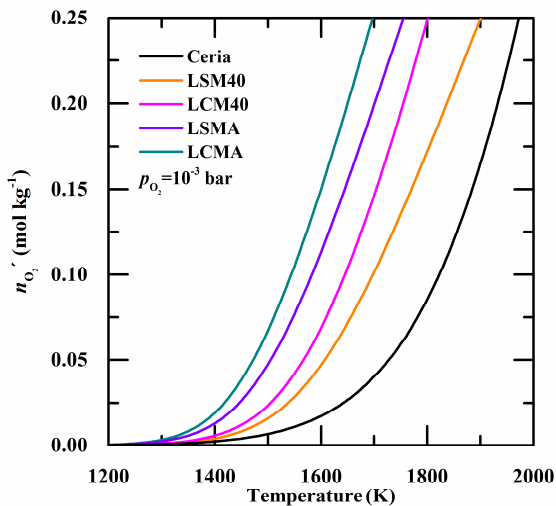
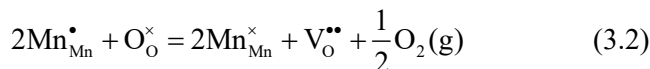


Figure 3.8. Mass specific oxygen evolution for LSM40, LCM40, LSMA, LCMA and ceria *versus* temperature at $p_{O_2} = 10^{-3}$ bar.

3.3 Defect modeling

Several defect models describing the oxygen nonstoichiometry of doped and undoped lanthanum-manganites can be found in literature.^{50, 84, 101-106} For undoped LaMnO_3 , La and Mn are in the trivalent state. When replacing some of the lanthanum by a divalent dopant (*e.g.* Sr, Ca) some of the Mn goes from its trivalent to its tetravalent state in order to compensate the charge differences introduced by the divalent dopant. In Kröger-Vink notation¹⁰⁷ this reads as $\text{La}_{1-x}^{\times}\text{Sr}_x^{\prime}\text{Mn}_{1-x}^{\times}\text{Mn}_x^{\bullet}\text{O}_3$. It was shown^{50, 84, 101, 103, 108} that the reduction of Sr-doped LaMnO_3 in the oxygen-deficient region can be described in Kröger-Vink notation as:



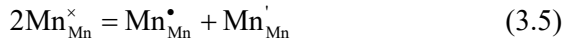
where tetravalent manganese ($\text{Mn}_{\text{Mn}}^{\bullet}$) on manganese lattice sites and oxygen atoms on oxygen lattice sites ($\text{O}_{\text{O}}^{\times}$) are in equilibrium with gaseous oxygen, trivalent manganese on manganese lattice sites ($\text{Mn}_{\text{Mn}}^{\times}$) and doubly ionized oxygen vacancies ($\text{V}_{\text{O}}^{\bullet\bullet}$). By applying the law of mass action, assuming activity coefficients equal 1 and a standard pressure $p^{\circ} = 1$ bar, the equilibrium constant for reaction (3.2) can be defined as:⁸⁵

$$K_1 = \frac{[\text{V}_{\text{O}}^{\bullet\bullet}][\text{Mn}_{\text{Mn}}^{\times}]^2}{[\text{O}_{\text{O}}^{\times}][\text{Mn}_{\text{Mn}}^{\bullet}]^2} (p_{\text{O}_2} / p^{\circ})^{1/2} \quad (3.3)$$

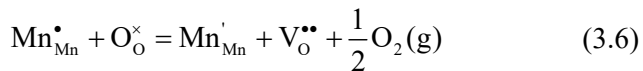
where square brackets denote concentrations taken as sublattice site fractions, *e.g.* for oxygen vacancies:

$$[\text{V}_{\text{O}}^{\bullet\bullet}] = \frac{n_{\text{V}_{\text{O}}^{\bullet\bullet}}}{n_{\text{V}_{\text{O}}^{\bullet\bullet}} + n_{\text{O}_{\text{O}}^{\times}}} \quad (3.4)$$

Trivalent manganese in Eq. (3.2) can further disproportionate to tetravalent and divalent manganese (Mn'_{Mn}) according to



By combining Eq. (3.5) with Eq. (3.2), the disproportionation reaction can be written as



with the equilibrium constant

$$K_2 = \frac{[\text{V}_{\text{O}}^{\bullet\bullet}][\text{Mn}'_{\text{Mn}}]}{[\text{O}_{\text{O}}^{\times}][\text{Mn}_{\text{Mn}}^{\bullet}]} (p_{\text{O}_2} / p^{\circ})^{1/2} \quad (3.7)$$

Measured oxygen nonstoichiometry of the four perovskites investigated in this work was modeled as a function of temperature and p_{O_2} by fitting the equilibrium constants K_1 and K_2 to the experimental data. A defect cluster model was not considered because it was reported to be limited to lower p_{O_2} values.¹⁰³ This is further supported by the very good fit of the proposed defect model to the experimental data. Site balances for manganese and oxygen

$$\begin{aligned} n_{\text{Mn}_{\text{Mn}}^{\bullet}} + n_{\text{Mn}_{\text{Mn}}^{\times}} + n_{\text{Mn}_{\text{Mn}}^{\cdot}} &= 1 - y \\ n_{\text{O}_{\text{O}}^{\times}} + n_{\text{V}_{\text{O}}^{\bullet}} &= 3 \end{aligned} \quad (3.8)$$

and charge neutrality

$$2n_{\text{V}_{\text{O}}^{\bullet}} + n_{\text{Mn}_{\text{Mn}}^{\bullet}} = x + n_{\text{Mn}_{\text{Mn}}^{\cdot}} \quad (3.9)$$

allow K_1 and K_2 to be written in terms of δ , p_{O_2} and one sublattice site fraction. The last unknown site fraction can be eliminated by combining K_1 and K_2 to one expression shown in a linear form by:

$$\underbrace{\frac{\delta^{1/2} (x + y - 2\delta - 1) (p_{\text{O}_2} / p^{\circ})^{1/4}}{(x - 2\delta)(3 - \delta)^{1/2}}}_Y = \underbrace{\frac{(3 - \delta)^{1/2} (2\delta - x + y - 1)}{\delta^{1/2} (x - 2\delta) (p_{\text{O}_2} / p^{\circ})^{1/4}}}_{X} K_2 - K_1^{1/2} \quad (3.10)$$

Complete derivation of Eq. (3.10) is shown in Appendix A. By plotting the measured nonstoichiometry data in the form Y versus X (cf. Eq. (3.10) and Figure A.1), K_1 and K_2 can be determined by linear regression. $-K_1^{1/2}$ equals the Y -intercept and K_2 the slope of the linear fit. Fitted equilibrium constants K_1 and K_2 versus $1000/T$ are shown in Figure 3.9(a) and (b), respectively. Lines indicate the best linear fits of $\ln K_1$ and $\ln K_2$ versus $1000/T$. The fitting parameters, represented by the enthalpy Δh_i° and

entropy Δs_i° of the single defect reactions ($i = 1$ for Eq. (3.2) and $i = 2$ for Eq. (3.6)), were extracted from the linear fits by using Eq. (3.11). Results are summarized in Table 3.3 for all four materials.

$$-\ln(K_i) = \frac{\Delta h_i^\circ}{RT} - \frac{\Delta s_i^\circ}{R}, \quad i = 1, 2 \quad (3.11)$$

Table 3.3. Linear fitting parameters of $\ln K_i$ versus $1000/T$ (cf. Eq.(3.11)) of all four perovskites represented by the enthalpy Δh_i° and entropy Δs_i° of the two single defect reactions.

Defect reaction	Extracted fitting parameter	LSM40	LCM40	LSMA	LCMA
Eq. (3.2) (K_1)	Δh_1° (kJ mol ⁻¹)	256.12	257.44	324.07	307.35
	Δs_1° (J mol ⁻¹ K ⁻¹)	98.60	101.54	133.05	127.36
Eq. (3.6) (K_2)	Δh_2° (kJ mol ⁻¹)	314.52	314.09	229.59	261.88
	Δs_2° (J mol ⁻¹ K ⁻¹)	96.82	106.52	61.16	82.35

Error bars shown in Figure 3.9 represent $\pm 2\sigma$ (two times standard deviation) of intercept (K_1) and slope (K_2) of the linear regression. With the knowledge of K_1 and K_2 , δ can be calculated for arbitrary p_{O_2} by solving Eq. (3.10). δ values calculated by using individual data points of Figure 3.9(a) and (b) are indicated by the solid black lines in Figure 3.6 and Figure 3.7. δ values shown by the colored dashed lines in Figure 3.6 and Figure 3.7 are determined by using the inverse linear temperature dependence of $\ln K_1$ and $\ln K_2$ as shown by the solid lines in Figure 3.9(a) and (b). In general, the measured δ values are well described by both fits. Thus, the reduction of all the four perovskites studied in this work can be well described by the reduction of Mn^{4+} to Mn^{3+} and Mn^{2+} , at least within the T and p_{O_2} range investigated here. Minor deviations of the two fits (black solid and colored dashed lines), especially towards higher δ values,

can be attributed to differences between individual data points (symbols) and linear fit in Figure 3.9(a) and (b). For LSM40, at $T = 1723$ K, 1623 K and 1573 K, best fits were obtained by only considering Eq. (3.2) ($K_2 = 0$).

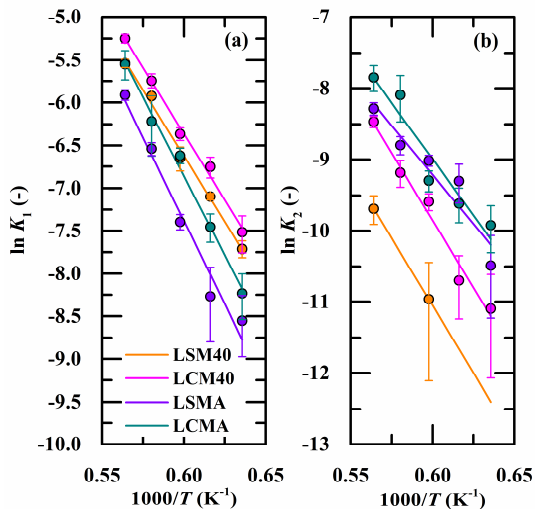


Figure 3.9. Equilibrium constants *versus* inverse temperature for LSM40, LCM40, LSMA and LCMA: (a) K_1 ; and (b) K_2 . Lines indicate linear fits of $\ln K$ on $1000/T$.

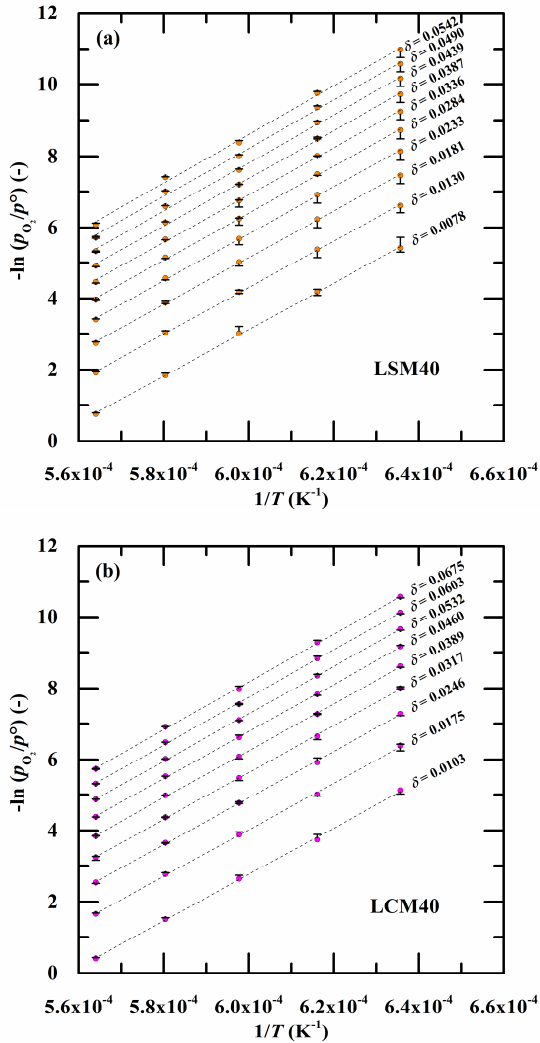


Figure 3.10. $-\ln(p_{O_2}/p^0)$ versus $1/T$ for LSM40 (a) and LCM40 (b) for the temperature range $T = 1573 \text{ K}$ to 1773 K and oxygen nonstoichiometry range $\delta = 0.0078\text{--}0.0542$ and $\delta = 0.0103\text{--}0.0675$, respectively.

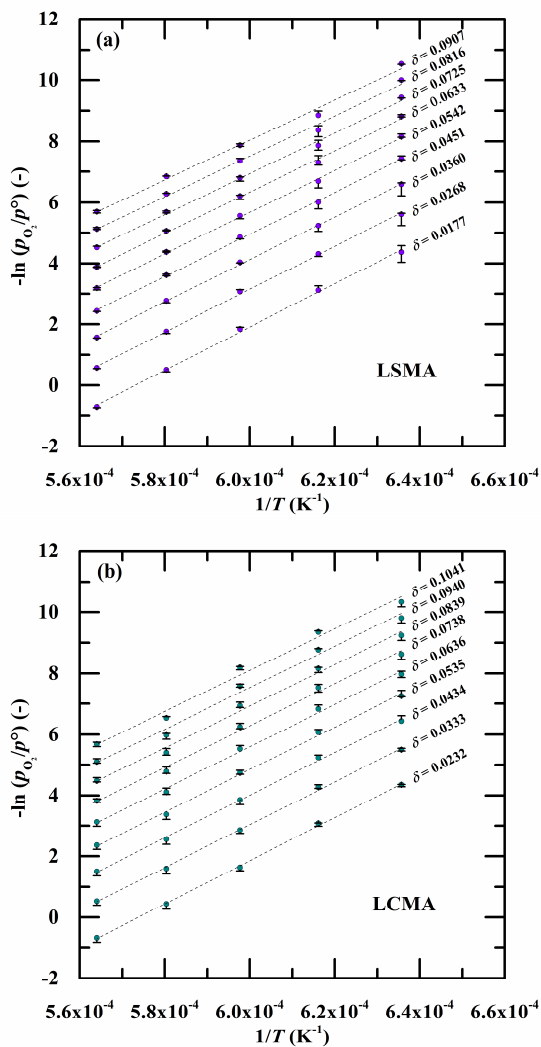


Figure 3.11. $-\ln(p_{O_2}/p^0)$ versus $1/T$ for LSMA (a) and LCMA (b) for the temperature range $T = 1573$ K to 1773 K and oxygen nonstoichiometry range $\delta = 0.0177$ – 0.0907 and $\delta = 0.0232$ – 0.1041 , respectively.

3.4 Thermodynamic properties

Assuming unity activity for the solid and ideal gas behavior for O₂, the standard partial molar Gibbs free energy, equivalent to the Gibbs free energy change of an infinitesimal reaction of Eq.(1.7), can be written as:⁸⁵

$$\Delta\bar{g}_O^\circ(\delta, T) = -\frac{1}{2}RT \ln(p_{O_2} / p^\circ) \quad (3.12)$$

$\Delta\bar{g}_O^\circ$ can be additionally related to the standard partial molar enthalpy ($\Delta\bar{h}_O^\circ$) and entropy ($\Delta\bar{s}_O^\circ$) according to

$$\Delta\bar{g}_O^\circ = \Delta\bar{h}_O^\circ - T \Delta\bar{s}_O^\circ \quad (3.13)$$

By combining Eq. (3.12) and (3.13) and assuming temperature independent partial molar enthalpy and entropy, $\Delta\bar{h}_O^\circ$ and $\Delta\bar{s}_O^\circ$ as a function of δ (defined per one mole of oxygen vacancies created in the lattice or equivalent to half a mole of O₂ released to the surrounding gas atmosphere) are obtained by determining the slope and intercept of $-\ln(p_{O_2}/p^\circ)$ versus $1/T$ for a constant δ ,

$$-\ln(p_{O_2} / p^\circ) = \frac{2\Delta\bar{h}_O^\circ}{RT} - \frac{2\Delta\bar{s}_O^\circ}{R} \Bigg|_{\delta=\text{const.}} \quad (3.14)$$

Constant δ values are obtained by evaluating the defect models in the temperature range $T = 1573$ K to 1773 K. Figure 3.10 and Figure 3.11 show $-\ln(p_{O_2}/p^\circ)$ versus $1/T$ of LSM40, LCM40 and LSMA, LCMA, respectively, for the temperature range $T = 1573$ K to 1773 K. The error bars correspond to deviations between measured and fitted p_{O_2} (obtained from fitted δ) shown in Figure 3.6 and Figure 3.7, whereas the symbols correspond to the fitted p_{O_2} shown by the black lines in Figure 3.6 and Figure 3.7. All data points are well represented by a linear fit ($R^2 > 0.93$)

indicating generally temperature independent $\Delta\bar{h}_O^\circ$ and $\Delta\bar{s}_O^\circ$ for all the perovskites within the temperature range investigated.

$\Delta\bar{h}_O^\circ$ and $\Delta\bar{s}_O^\circ$ as a function of δ are shown in Figure 3.12 and Figure 3.13, respectively, for all four perovskites investigated. Symbols represent $\Delta\bar{h}_O^\circ$ and $\Delta\bar{s}_O^\circ$ values calculated from δ values shown by the solid black lines of Figure 3.6 and Figure 3.7. Dashed lines represent modeled values calculated based on only the colored dashed lines of Figure 3.6 and Figure 3.7. Error bars were calculated from $\pm 2\sigma$ of slope (for $\Delta\bar{h}_O^\circ$) and intercept (for $\Delta\bar{s}_O^\circ$) of the linear regression of $-\ln(p_{O_2}/p^\circ)$ versus $1/T$ (*cf.* Figure 3.10, Figure 3.11 and Eq. (3.14)). The agreement between measured and modeled $\Delta\bar{h}_O^\circ$ and $\Delta\bar{s}_O^\circ$ values is quite good except for LSM40, where the discrepancy can be attributed to larger deviations between defect model

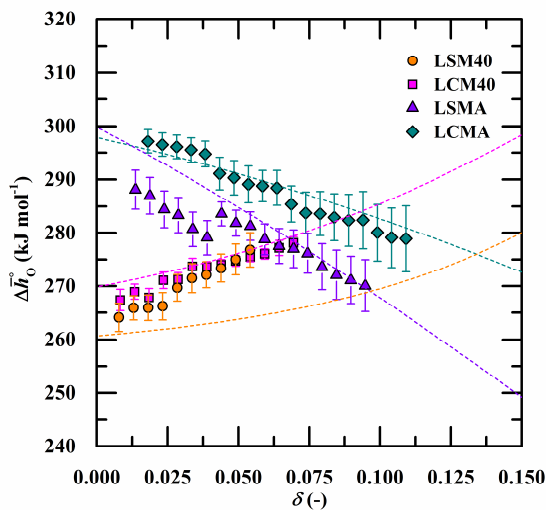


Figure 3.12. Standard partial molar enthalpy $\Delta\bar{h}_O^\circ$ for LSM40, LCM40, LSMA and LCMA as a function of δ . Symbols represent measured values calculated based on δ values shown by the black solid lines in Figure 3.6 and Figure 3.7 whereas dashed lines represent modeled values calculated based on δ values shown by the colored dashed lines in Figure 3.6 and Figure 3.7.

and measured δ values (*cf.* Figure 3.6 (a)). Interestingly, $\Delta\bar{h}_0^\circ$ of the Al-doped perovskites (LSMA and LCMA) decreases with increasing δ whereas $\Delta\bar{h}_0^\circ$ of the two non-Al-doped perovskites (LSM40 and LCM40) slightly increases with increasing δ . $\Delta\bar{h}_0^\circ$ values of the Ca-doped perovskites are slightly higher compared to their equivalent Sr-doped ones. $\Delta\bar{h}_0^\circ$ values of LSM40 shown in this work are consistent with the values calculated by Yang *et al.*⁵² using nonstoichiometry measurements of Mizusaki *et al.*⁸⁴, however, they observed a small decrease in enthalpy with increasing δ . The trend of increasing enthalpy with δ was also observed by Cooper *et al.*⁸⁵, although their values are lower than those reported here. In contrast, $\Delta\bar{h}_0^\circ$ values of LCMA and LSMA measured by Cooper *et al.*⁸⁵ increased with δ and therefore values differ by up to 100 kJ mol⁻¹ at low δ (≈ 0.02). Measurements for LCM40 are in good agreement. Compared to literature data of ceria⁶², $\Delta\bar{h}_0^\circ$ values obtained for the perovskites are around 150 kJ mol⁻¹ lower at $\delta \approx 0.07$. This result is expected because of the much higher reduction extents (or lower reduction temperature) of the perovskites compared to ceria. Although $\Delta\bar{h}_0^\circ$ of the Ca-doped perovskites is higher compared to that of Sr-doped ones, reduction extents are larger. This can be explained by the higher $\Delta\bar{s}_0^\circ$ (discussed below) which results in a lower $\Delta\bar{g}_0^\circ$ for the Ca-doped materials.

The $\Delta\bar{s}_0^\circ$ values of the Al-doped perovskites (LCMA and LSMA) show a much steeper decrease with increasing δ compared to the non-Al-doped ones (LCM40 and LSM40). $\Delta\bar{s}_0^\circ$ is highest for LCMA followed by LSMA, LCM40 and LSM40, at least for $\delta < 0.75$. Entropy values of LSM40 and their dependence on δ reported by Yang *et al.*⁵² are similar to

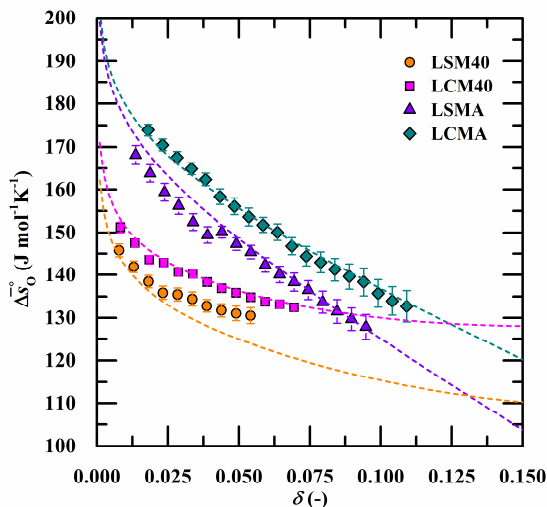


Figure 3.13. Standard partial molar entropy $\Delta\bar{s}_0^\circ$ for LSM40, LCM40, LSMA and LCMA as a function of δ . Symbols represent measured values calculated based on δ values shown by the black solid lines in Figure 3.6 and Figure 3.7 whereas dashed lines represent modeled values calculated based on δ values shown by the colored dashed lines in Figure 3.6 and Figure 3.7.

this work. $\Delta\bar{s}_0^\circ$ values measured by Cooper *et al.*⁸⁵ are comparable to the measurements shown in this work, except for LSM40 which are higher in this work. Cooper *et al.*⁸⁵ show highest $\Delta\bar{s}_0^\circ$ for LCM40 (out of LCMA, LSMA, LCM40 and LSM40) whereas here, highest $\Delta\bar{s}_0^\circ$ was measured for LCMA (for $\delta < 0.125$). Deviations in the partial molar thermodynamic properties from the work of Cooper *et al.*⁸⁵ might be explained by differences in the measured oxygen nonstoichiometry. The increase in $\Delta\bar{h}_0^\circ$ and $\Delta\bar{s}_0^\circ$ when adding Al to the B-site of $\text{La}_{1-x}\text{Ca}_x\text{MnO}_3$ is in agreement with the measurements of Tanasescu *et al.*¹⁰⁹ (at least for $\delta <$

0.02). Compared to ceria,⁶² $\Delta\bar{s}_0^\circ$ values of the perovskites are in general more than $50 \text{ J mol}^{-1} \text{ K}^{-1}$ lower.

The partial molar Gibbs free energy $\Delta\bar{g}_0^\circ$ as a function of T and δ was calculated from modeled $\Delta\bar{h}_0^\circ$ and $\Delta\bar{s}_0^\circ$ values (*cf.* dashed lines in Figure 3.12 and Figure 3.13) according to Eq. (3.13), where it was assumed that $\Delta\bar{h}_0^\circ$ and $\Delta\bar{s}_0^\circ$ are independent of T . $\Delta\bar{g}_0^\circ$ of the perovskites and ceria⁶² are shown in Figure 3.14 for $\delta = 0.10$, relevant for the metal oxide reduction reaction, and negative $\Delta\bar{g}_0^\circ$ for $\delta = 0.01$, relevant for the oxidation reaction with H_2O or CO_2 . For comparison, the corresponding

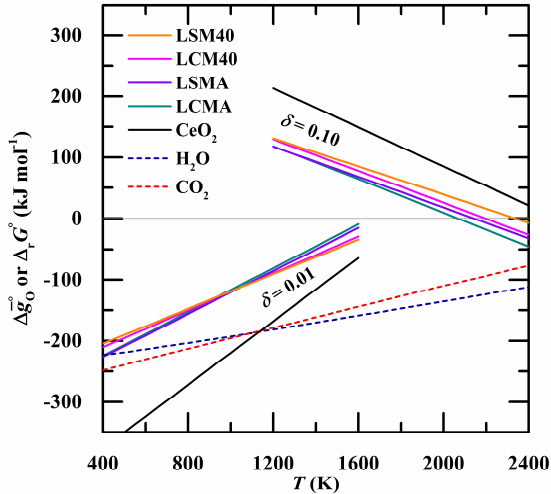


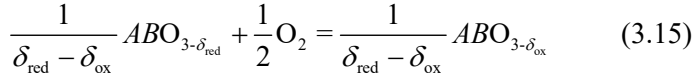
Figure 3.14. Standard partial molar Gibbs free energy $\Delta\bar{g}_0^\circ$ for LSM40, LCM40, LSMA, LCMA and CeO_2 for $\delta = 0.10$, relevant for the reduction, and negative $\Delta\bar{g}_0^\circ$ for $\delta = 0.01$, relevant for the oxidation reaction. Dashed lines represent the Gibbs free energy change of the H_2 oxidation reaction: $\text{H}_2 + 0.5\text{O}_2 = \text{H}_2\text{O}$ ($-\Delta_r G_{\text{H}_2\text{O}}^\circ$, blue) and of the CO oxidation reaction: $\text{CO} + 0.5\text{O}_2 = \text{CO}_2$ ($-\Delta_r G_{\text{CO}_2}^\circ$, red). The metal oxide reduction reaction is at equilibrium in 1 bar p_{O_2} at $\delta = 0.10$ at the temperature where $\Delta\bar{g}_0^\circ(\delta = 0.10) = 0$. The oxidation with $\text{H}_2\text{O}/\text{CO}_2$ to $\delta = 0.01$ is thermodynamically favorable at temperatures where $-\Delta\bar{g}_0^\circ(\delta = 0.01) = -\Delta_r G_{\text{H}_2\text{O}}^\circ$ or $-\Delta_r G_{\text{CO}_2}^\circ$, respectively.

values for ceria⁶² were calculated: $\Delta\bar{g}_O^\circ(\delta = 0.10)$ with $\Delta\bar{h}_O^\circ = 405 \text{ kJ mol}^{-1}$ and $\Delta\bar{s}_O^\circ = 160 \text{ J mol}^{-1} \text{ K}^{-1}$ and $\Delta\bar{g}_O^\circ(\delta = 0.01)$ with $\Delta\bar{h}_O^\circ = 480 \text{ kJ mol}^{-1}$ and $\Delta\bar{s}_O^\circ = 260 \text{ J mol}^{-1} \text{ K}^{-1}$ and additionally shown in Figure 3.14. Dashed lines represent the Gibbs free energy change of H₂ oxidation: $\text{H}_2 + 0.5\text{O}_2 = \text{H}_2\text{O}$ ($-\Delta_r G_{\text{H}_2\text{O}}^\circ$, blue) and of CO oxidation: $\text{CO} + 0.5\text{O}_2 = \text{CO}_2$ ($-\Delta_r G_{\text{CO}_2}^\circ$, red), obtained from NIST-JANAF thermochemical tables. The reduction reaction of the metal oxide is at equilibrium at $p_{\text{O}_2} = 1 \text{ bar}$ and $\delta = 0.10$ at the temperature where $\Delta\bar{g}_O^\circ(\delta = 0.10) = 0$. The oxidation with H₂O/CO₂ to $\delta = 0.01$ is thermodynamically favorable at temperatures where $-\Delta\bar{g}_O^\circ(\delta = 0.01) = -\Delta_r G_{\text{H}_2\text{O}}^\circ$ or $-\Delta_r G_{\text{CO}_2}^\circ$, respectively. From Figure 3.14 it can be concluded that at $p_{\text{O}_2} = 1 \text{ bar}$, LCMA reduction to $\delta = 0.10$ is favorable at $T = 2070 \text{ K}$ and at even higher temperatures for the other perovskites and ceria. The oxidation of LSM40 and LCM40 with H₂O and CO₂ to $\delta = 0.01$ (assuming $p_{\text{CO}}/p_{\text{CO}_2} = 1$ or $p_{\text{H}_2}/p_{\text{H}_2\text{O}} = 1$) is not favorable at $T > 400 \text{ K}$, whereas the oxidation of the Al-doped perovskites with H₂O is favorable at 420 K (LSMA) and 405 K (LCMA). Their oxidation with CO₂ is thermodynamically unfavorable at $T > 400 \text{ K}$. The oxidation of ceria to $\delta = 0.01$ with H₂O and CO₂ is favorable at much higher temperature ($T = 1050 \text{ K}$) compared to the oxidation of the perovskites. At $T = 1050 \text{ K}$, the oxidation with H₂O and CO₂ is identically favorable. The favorable oxidation thermodynamics of ceria can be explained by its relatively high $\Delta\bar{h}_O^\circ$ and $\Delta\bar{s}_O^\circ$ values. The high $\Delta\bar{s}_O^\circ$ results in a relatively high $\Delta\bar{g}_O^\circ$ value at lower temperatures and a relatively low $\Delta\bar{g}_O^\circ$ at higher temperatures. Out of the perovskites, LCMA

shows the best thermodynamic performance because of the highest $\Delta\bar{s}_O^\circ$ and additionally a decreasing $\Delta\bar{h}_O^\circ$ with increasing δ .

3.5 Water splitting

Similar to Chapter 2.5, here the focus is on H₂O splitting, but the thermodynamics of CO₂ splitting are qualitatively very similar and give similar insights into the performance of candidate redox materials.^{63, 85} Thermodynamically, the water splitting reaction can be described by the simultaneous oxidation of the perovskite with O₂ and the splitting of H₂O into H₂ and 1/2O₂, as shown by Eq. (3.15) and (3.16), respectively.



The chemical equilibrium is described by the two simultaneous reaction equilibria

$$\Delta_r G_{\text{ox}}^\circ(\delta_{\text{ox}}, T_{\text{ox}}) = -\Delta\bar{g}_O^\circ(\delta_{\text{ox}}, T_{\text{ox}}) = \frac{1}{2}RT_{\text{ox}} \ln(p_{O_2} / p^\circ) \quad (3.17)$$

$$\Delta_r G_{H_2O}^\circ(T_{\text{ox}}) = -RT_{\text{ox}} \ln K_w = -RT_{\text{ox}} \ln \left(\frac{p_{H_2} p_{O_2}^{1/2}}{p_{H_2O}} p^{\circ-1/2} \right) \quad (3.18)$$

where p_{O_2} , p_{H_2} and p_{H_2O} denotes the equilibrium partial pressures of O₂, H₂ and H₂O, respectively and K_w is the reaction equilibrium constant of the H₂ oxidation reaction. Assigning reaction coordinates ξ_1 to Eq. (3.15) and ξ_2 to Eq. (3.16) and assuming that reactions proceed in a closed-

system with variable volume, the equilibrium gas-phase composition may be found according to:¹¹⁰

$$\begin{aligned}
 n_{\text{H}_2\text{O}} &= n_{\text{H}_2\text{O},i} - \xi_2 \\
 n_{\text{H}_2} &= n_{\text{H}_2,i} + \xi_2 \\
 n_{\text{O}_2} &= n_{\text{O}_2,i} - \frac{1}{2}\xi_1 + \frac{1}{2}\xi_2 \\
 n_{\text{tot(g)}} &= n_{\text{O}_2} + n_{\text{H}_2} + n_{\text{H}_2\text{O}} \\
 \delta_{\text{ox}} &= \delta_{\text{red}} - \xi_1
 \end{aligned} \tag{3.19}$$

where the subscript i denotes initial molar amount of the gas species. The partial pressure of gas phase species g is defined by

$$p_g = \frac{n_g}{n_{\text{tot}}} p_{\text{tot}} \tag{3.20}$$

where p_{tot} denotes the closed system total pressure. For given $n_{\text{H}_2\text{O},i}$, $n_{\text{H}_2,i}$ ($= 0$), $n_{\text{O}_2,i}$ ($= 0$), T_{ox} , δ_{red} and p_{tot} , the equilibrium gas phase composition ($n_{\text{H}_2\text{O}}$, n_{H_2} , n_{O_2}), the equilibrium partial pressures ($p_{\text{H}_2\text{O}}$, p_{H_2} , p_{O_2}) and the reaction coordinates (ξ_1 , ξ_2) can be determined by simultaneously solving Eq. (3.17) - (3.20). Gas phase amounts of H, O and OH were assumed to be negligible at $T < 1600\text{K}$.¹⁴ Figure 3.15(a) shows $\xi_1 = \delta_{\text{red}} - \delta_{\text{ox}}$, the H_2 yield (black dashed lines), and n_{H_2} , the equilibrium amount of H_2 , (red solid lines) *versus* temperature upon oxidation of LCMA ($\delta_{\text{red}} = 0.127$, calculated at $T_{\text{red}} = 1673\text{ K}$ and $p_{\text{O}_2,\text{red}} = 10^{-4}\text{ bar}$) at $p_{\text{tot}} = 1\text{ bar}$ for $n_{\text{H}_2\text{O},i} = 1000\text{ mol}$ (circles), $n_{\text{H}_2\text{O},i} = 100\text{ mol}$ (triangles), $n_{\text{H}_2\text{O},i} = 1\text{ mol}$ (squares) and $n_{\text{H}_2\text{O},i} \rightarrow \infty$ (+ symbols). For $n_{\text{H}_2\text{O},i} = 1000\text{ mol}$ and $T < 1200\text{ K}$, $\xi_1 \approx n_{\text{H}_2}$, meaning that most of the O_2 produced by Eq. (3.16) is consumed by the perovskite and therefore the amount of H_2 from thermolysis of the excess H_2O has a negligible contribution to the total equilibrium amount of H_2 . At $T > 1200\text{ K}$, $n_{\text{H}_2} > \xi_1$, meaning that a significant amount of the excess H_2O splits into H_2 and O_2 whereas this amount of O_2 is not

consumed by the perovskite. When cooling down the equilibrium gas mixture to room temperature, n_{H_2} minus ζ_1 moles of H_2 may recombine with the gas-phase O_2 to H_2O . Therefore, the minimum amount of H_2 that can be used for further processing at lower temperatures (*e.g.* converting to liquid fuels) is ζ_1 , indicated by the black dashed lines and colored grey area in Figure 3.15(a). It is shown that H_2 yields increase with decreasing temperature and increasing $n_{\text{H}_2\text{O},i}$. For comparison, the equilibrium amount of H_2 for thermolysis only ($\zeta_1 = 0$) as a function of temperature is shown in Figure 3.15(a) (blue dotted lines). As expected, towards higher temperatures, n_{H_2} for thermolysis only converges towards n_{H_2} upon oxidation of the perovskite. This is expected because towards higher temperatures the amount of gas-phase oxygen consumed by the perovskite decreases (decreasing ζ_1 and increasing δ_{ox}). Equilibrium amounts of H_2 are always higher in the case of perovskite oxidation compared to thermolysis only. Figure 3.15(b) shows the corresponding equilibrium partial pressures p_{H_2} (red solid lines) and p_{O_2} (green solid lines) upon oxidation of LCMA. By increasing $n_{\text{H}_2\text{O},i}$, p_{H_2} decreases because of the higher dilution of H_2 in H_2O , which ultimately results in an increase in p_{O_2} (*cf.* Eq. (3.18)). Because δ_{ox} decreases with increasing p_{O_2} at constant temperature (*cf.* Figure 3.6 and Figure 3.7), H_2 yields (ζ_1) increase with increasing $n_{\text{H}_2\text{O},i}$. However, it should be kept in mind that the H_2 concentration in the product gas will decrease when flowing large amounts of H_2O . The + symbols shown in Figure 3.15(b) represent the minimum p_{H_2} and maximum p_{O_2} that could theoretically be obtained at $p_{\text{tot}} = 1$ bar and are equal to the equilibrium partial pressures of the thermolysis reaction. Therefore, + symbols in Figure 3.15(a) show the maximum H_2 yield upon oxidation of LCMA with H_2O ($\delta_{\text{red}} = 0.127$) at 1 bar. For an open system, this would imply a perfectly purged reactive

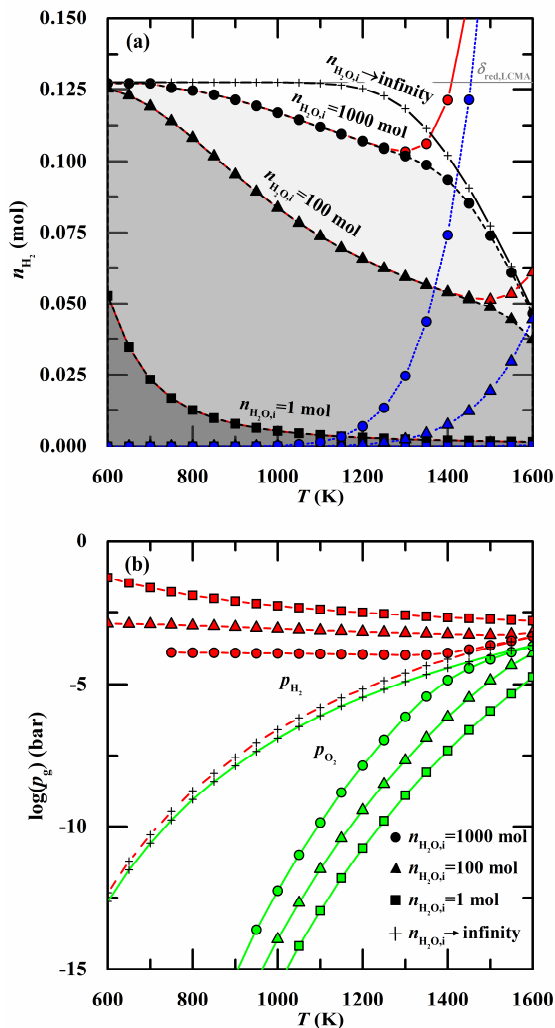


Figure 3.15. (a) H₂ yield ($\zeta_1 = \delta_{\text{red}} - \delta_{\text{ox}}$) upon oxidation of LCMA (black dashed lines), total equilibrium amount of H₂ (n_{H_2}) (red solid lines) and equilibrium amount of H₂ considering direct thermolysis only (blue dotted lines) versus temperature. (b) Corresponding equilibrium partial pressures of H₂ (red solid lines), of O₂ (green solid lines) upon oxidation of LCMA. In (a) and (b), squares represents results for $n_{\text{H}_2\text{O},i} = 1$ mol, triangles for $n_{\text{H}_2\text{O},i} = 100$ mol, circles for $n_{\text{H}_2\text{O},i} = 1000$ mol and + symbols for $n_{\text{H}_2\text{O},i} \rightarrow \infty$, all at $p_{\text{tot}} = 1$ bar. p_{H_2} and p_{O_2} shown by the + symbols ($n_{\text{H}_2\text{O},i} \rightarrow \infty$) represents the minimum p_{H_2} and maximum p_{O_2} and are equal to the equilibrium partial pressures of the H₂O thermolysis reaction.

structure or running the oxidation for an infinite long time, whereas for a closed system, this would require an infinite amount of H_2O . The results for $n_{\text{H}_2\text{O},i} \rightarrow \text{infinity}$ are in agreement with the thermogravimetric analysis of Cooper *et al.*⁸⁵ where they experimentally showed that CO production upon oxidation of LCMA with CO_2 significantly decreases with increasing temperature and that the material cannot be fully oxidized at $T \geq 1323$ K under pure CO_2 .

The influence of p_{tot} on the H_2 yield upon oxidation of LCMA ($\delta_{\text{red}} = 0.127$ at $T_{\text{red}} = 1673$ K and $p_{\text{O}_2,\text{red}} = 10^{-4}$ bar) for $n_{\text{H}_2\text{O},i} = 100$ mol is shown in Figure 3.16(a) and the corresponding equilibrium partial pressures are shown in Figure 3.16(b). Labeling is similar to Figure 3.15, but here circles represent results for $p_{\text{tot}} = 0.01$ bar, triangles $p_{\text{tot}} = 1$ bar and squares $p_{\text{tot}} = 100$ bar. It is shown that under most conditions ($p_{\text{tot}} > 0.01$ bar and $T < 1300$ K), the total pressure does not significantly affect the equilibrium H_2 yield, except for higher temperatures and lower p_{tot} , where $\xi_1 \neq n_{\text{H}_2}$; here the H_2 yield slightly increases with increasing p_{tot} . As long as $\xi_1 \approx n_{\text{H}_2}$, implying that thermolysis of the excess steam does not significantly affect the H_2 equilibrium amount, one mole of H_2 is produced per mole of H_2O , whereas the O_2 is consumed by the perovskite. Therefore, the number of moles in the gas phase stays constant and therefore the overall reaction is not influenced by a change in p_{tot} . When thermolysis becomes significant, the number of moles in the equilibrium gas phase increases and therefore a change in p_{tot} shifts the chemical equilibrium. Indeed, this is shown in Figure 3.16(b), where p_{O_2} does not significantly change by increasing or decreasing p_{tot} , at least for $p_{\text{tot}} > 0.01$ bar and $T < 1300$ K. p_{H_2} increases with increasing p_{tot} , but the ratio of $p_{\text{H}_2\text{O}}/p_{\text{H}_2}$ is constant which leads to a constant p_{O_2} according to Eq. (3.18). For high temperatures and large $n_{\text{H}_2\text{O},i}$, where p_{O_2} converges to

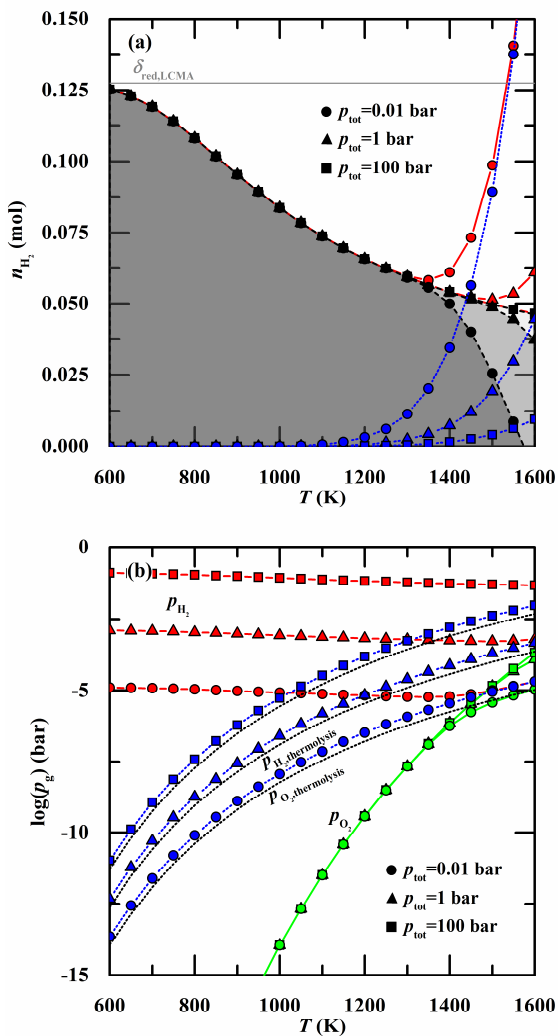


Figure 3.16. (a) H₂ yield ($\zeta_1 = \delta_{\text{red}} - \delta_{\text{ox}}$) upon oxidation of LCMA (black dashed lines) as a function of temperature and 3 different operating pressures. Total equilibrium yields of H₂ (n_{H_2}) (red solid lines) and equilibrium amount of H₂ considering direct thermolysis only (blue dotted lines) are also shown. (b) Corresponding equilibrium partial pressures of H₂ (red solid lines), of O₂ (green solid lines) upon oxidation of LCMA. Blue and black dotted lines indicate the equilibrium partial pressure of H₂ and O₂ for thermolysis only, which is equivalent to the partial pressures when $n_{\text{H}_2\text{O},i} \rightarrow \infty$. In (a) and (b), squares represents results for $p_{\text{tot}} = 100$ bar, triangles for $p_{\text{tot}} = 1$ bar and circles for $p_{\text{tot}} = 0.01$ bar, all for $n_{\text{H}_2\text{O},i} = 100$ mol.

$p_{\text{O}_2, \text{thermolysis}}$ and p_{H_2} to $p_{\text{H}_2, \text{thermolysis}}$, higher H_2 yields could theoretically be obtained at higher p_{tot} . However, such operation conditions (large amount of $n_{\text{H}_2\text{O},i}$ or running oxidation for a very long time) might not be efficient for a solar thermochemical process.

Figure 3.17(a) shows the theoretical H_2 yield at $p_{\text{tot}} = 1$ bar, assuming reaction in a closed system with variable volume and constant pressure, *versus* temperature for LCMA, LSMA, LCM40, LSM40 and CeO_2 ⁶². Results are shown for $n_{\text{H}_2\text{O},i} = 1$ mol per mole metal oxide (squares) and $n_{\text{H}_2\text{O},i} = 1000$ mol (circles). The nonstoichiometry before oxidation (δ_{red}) was calculated for the reduction conditions $T_{\text{red}} = 1673$ K and $p_{\text{O}_2} = 10^{-4}$ bar and additionally for $T_{\text{red}} = 1873$ K and $p_{\text{O}_2} = 10^{-4}$ bar for CeO_2 (open symbols). δ_{red} for each material is indicated by the solid horizontal lines and represent the maximum H_2 yield that could be obtained when oxidizing to $\delta_{\text{ox}} = 0$. For $n_{\text{H}_2\text{O},i} = 1$ mol, all the perovskites show only minor H_2 production and reach oxidation extents of less than 42% for $T > 600$ K. However, CeO_2 oxidizes by more than 85% as high as $T = 1200$ K; its maximum H_2 yield ($\delta_{\text{red}} = 0.018$) is relatively low under the reduction conditions considered for the perovskites however. By increasing $n_{\text{H}_2\text{O},i}$ to 1000 mol, all materials can be oxidized at higher temperatures because of the higher p_{O_2} , resulting in H_2 yields higher than 80% at $T = 1200$ K for all materials. In summary, all perovskites investigated within this work only produce more H_2 compared to ceria under a large excess of oxidant gas and/or at relatively low oxidation temperatures. Both scenarios imply additional energy penalties, for example to heat oxidant gas, separate reaction products and to overcome a high temperature difference between the low temperature oxidation and high temperature reduction (large sensible heat penalty). The finding of higher H_2 yield for CeO_2 (at least for $T > 750$ K) compared to the perovskites under relatively small $n_{\text{H}_2\text{O},i}$ is in good agreement with the

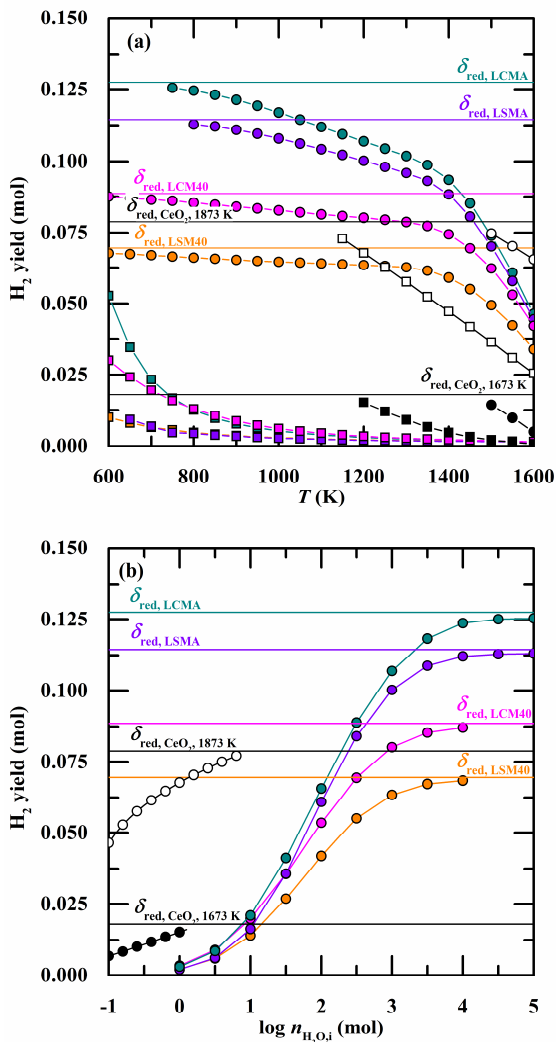


Figure 3.17. (a) Calculated H_2 yield upon oxidation of LCMA, LSMA, LCM40, LSM40 and CeO_2 versus temperature for $n_{H_2O,i} = 1$ mol (squares) and $n_{H_2O,i} = 1000$ mol (circles) at $p_{\text{tot}} = 1$ bar. (b) Calculated H_2 yield upon oxidation of LCMA, LSMA, LCM40, LSM40 and CeO_2 versus $n_{H_2O,i}$ for $T = 1200$ K at $p_{\text{tot}} = 1$ bar. In (a) and (b), the oxygen nonstoichiometry before oxidation (δ_{red}) is shown by the solid lines and was determined for $T_{\text{red}} = 1673$ K and $p_{O_2} = 10^{-4}$ bar for all materials and additionally for $T_{\text{red}} = 1873$ K and $p_{O_2} = 10^{-4}$ bar for CeO_2 (open symbols). H_2 yields close to their maximum are not shown because partial molar thermodynamic data was only calculated for $\delta \geq 0.001$.

calculations of Scheffe *et al.*⁵⁰ for LSM30 and LSM40 and Cooper *et al.*⁸⁵ for LCM40, LCMA and LSMA. The finding of higher fuel yields with increasing amount of oxidant gas is in agreement with literature studies on doped ceria^{62, 63} and perovskites^{50, 85}. For such a high amount of oxidant gas (e.g. $n_{\text{H}_2\text{O},i} = 1000$ mol per mole of metal oxide), highest H_2 yield is reached with LCMA, the perovskite showing the highest reduction extent.

These results point out that qualitative oxidation experiments under large CO_2 and/or H_2O excess in a thermogravimetric analyzer or equivalent test setup can result in misleading predictions of a material's potential to efficiently split CO_2 and/or H_2O in a solar reactor because of flowing relatively large amounts of oxidant gas for a long time and therefore attaining a high p_{O_2} . The high p_{O_2} results then in a low oxygen nonstoichiometry after oxidation and therefore a high fuel yield. When assuming a total pressure of 1 bar and $T = 1100$ K, a maximum $p_{\text{O}_2} \approx 7.5 \times 10^{-7}$ bar could be attained when flowing H_2O only (equal to the equilibrium p_{O_2} of the thermolysis reaction). However, the assumption of such a high p_{O_2} for the equilibrium of the oxidation reaction with H_2O would imply a perfectly purged material structure or an infinitely long oxidation reaction when considering an open reaction system, or an infinite amount of H_2O when considering a closed system. For solar reactor systems, typical maximum p_{O_2} during oxidation are much lower because it is inefficient to run oxidation until completion⁴² and/or to heat large amounts of excess CO_2 or H_2O . For example, by limiting the minimum H_2 concentration in the product gas to 1% (at $T = 298$ K), a maximum p_{O_2} of only about 1.6×10^{-14} bar could be obtained at $T = 1100$ K. This is more than seven orders of magnitude lower compared to the p_{O_2} when flowing steam only. By looking at oxygen nonstoichiometry measurements of $\text{La}_{0.5}\text{Sr}_{0.5}\text{MnO}_3$ ⁸⁴ it can be seen that at $T = 1100$ K and $p_{\text{O}_2} \approx 7.5 \times 10^{-7}$ bar (pure steam), its oxygen nonstoichiometry is $\delta_{\text{ox}} \approx 0$,

whereas at $p_{\text{O}_2} \approx 1.6 \times 10^{-14}$ bar, $\delta_{\text{ox}} \approx 0.17$. This means that by doing experiments in a thermogravimetric analyzer (or equivalent test setup) with a large amount of H_2O for a relatively long reaction time, H_2 yield gets over-predicted by around 0.17 mol H_2 per mole of $\text{La}_{0.5}\text{Sr}_{0.5}\text{MnO}_3$ compared to a solar reactor where the minimum outlet concentration of H_2 was fixed to 1%. Therefore, extracted fuel yields from simple Ar/ CO_2 or Ar/ H_2O cycling experiments performed in a thermogravimetric analyzer (or equivalent setup) should be considered as maximum fuel yields attainable but do not necessarily represent a material's fuel productivity in a solar reactor.

3.6 Conclusions

Oxygen nonstoichiometry measurements of $\text{La}_{0.6}\text{A}_{0.4}\text{Mn}_{1-y}\text{Al}_y\text{O}_{3-\delta}$ ($A = \text{Ca}, \text{Sr}$ and $y = 0, 0.4$) in the temperature range $T = 1573 \text{ K} - 1773 \text{ K}$ and oxygen partial pressure range $p_{\text{O}_2} = 4.5066 \times 10^{-2} \text{ bar} - 9.9 \times 10^{-5} \text{ bar}$ revealed that the highest reduction extents are obtained using $\text{La}_{0.6}\text{Ca}_{0.4}\text{Mn}_{0.6}\text{Al}_{0.4}\text{O}_{3-\delta}$ (LCMA). Compared to the state-of-the-art material ceria, LCMA releases more than 500% more O_2 per unit mass of redox material at $T = 1700 \text{ K}$ and $p_{\text{O}_2} = 10^{-3} \text{ bar}$. It releases 0.15 mol O_2 per kg of redox material at 285 K lower reduction temperature than ceria (1885 K for CeO_2 and 1600 K for LCMA) at $p_{\text{O}_2} = 10^{-3} \text{ bar}$. It was found that oxygen nonstoichiometry increases when replacing the divalent dopant Sr in $\text{La}_{0.6}\text{Sr}_{0.4}\text{MnO}_{3-\delta}$ with Ca and additionally significantly increases when doping 40 mol% Al on the Mn-site. The oxygen nonstoichiometry of all perovskites investigated was accurately modeled by a chemical defect model considering the reduction of Mn^{4+} to Mn^{3+} in combination with a disproportionation reaction of Mn^{3+} to Mn^{4+} and Mn^{2+} . From the defect models, partial molar thermodynamic properties ($\Delta \bar{h}_{\text{O}}^\circ$, $\Delta \bar{s}_{\text{O}}^\circ$, $\Delta \bar{g}_{\text{O}}^\circ$) were extracted. When doping Al to the Mn-site of

$\text{La}_{0.6}\text{Sr}_{0.4}\text{MnO}_{3-\delta}$ and $\text{La}_{0.6}\text{Ca}_{0.4}\text{MnO}_{3-\delta}$, $\Delta\bar{h}_0^\circ$ changes its trend of increasing $\Delta\bar{h}_0^\circ$ with δ to decreasing $\Delta\bar{h}_0^\circ$ with δ . This has an impact on the performance because a low enthalpy value towards higher δ is desired for a favorable reduction and a high enthalpy value at low δ is desired for a favorable oxidation with H_2O and CO_2 . In general, $\Delta\bar{h}_0^\circ$ and $\Delta\bar{s}_0^\circ$ of the perovskites are significantly lower compared to CeO_2 , leading to a thermodynamically more favorable reduction step, but less favorable oxidation (fuel production) step. Indeed, closed system calculations indicate that H_2 or CO yields of CeO_2 can only be surpassed using high amounts of excess $\text{H}_2\text{O}/\text{CO}_2$ and/or at much lower oxidation temperatures; both approaches imply additional energy penalties to heat excess $\text{H}_2\text{O}/\text{CO}_2$ and/or to overcome larger temperature differences between oxidation and reduction steps. Therefore, compared to the perovskites investigated in this work, a material with a higher $\Delta\bar{h}_0^\circ$ and higher $\Delta\bar{s}_0^\circ$ would be desired, yielding a higher $\Delta\bar{g}_0^\circ$ at lower temperatures (relevant for oxidation) and a lower $\Delta\bar{g}_0^\circ$ at higher temperatures (relevant for reduction). A strong decrease of $\Delta\bar{h}_0^\circ$ with δ would also be favorable.

As a summary, Figure 3.18 shows the thermodynamic equilibrium of reduction and oxidation reaction of all the materials investigated in this work. Figure 3.18 is very similar to Figure 2.10 and Figure 3.14, but also includes the equilibrium functions for the reduction (Eq. (3.12)) at $p_{\text{O}_2} = 1 \times 10^{-3}$, 1×10^{-4} , 1×10^{-5} and 1×10^{-6} bar and for the oxidation (Eq. (3.18)) with H_2O (a) and CO_2 (b) for fuel ratios of 0.1, 1 and 10. It is shown that at $p_{\text{O}_2} \geq 1 \times 10^{-3}$ bar, reduction to $\delta = 0.1$ proceeds at lowest temperature for LCMA followed by LSMA, LCM40, LSM40, CZO_20, CZO_5 and undoped ceria. Oxidation with H_2O or CO_2 to $\delta = 0.01$ proceeds at highest temperature for undoped ceria followed by CZO_5, LSMA, LCMA, CZO_20, LCM40 and LSM40 whereas temperature swing is smallest for

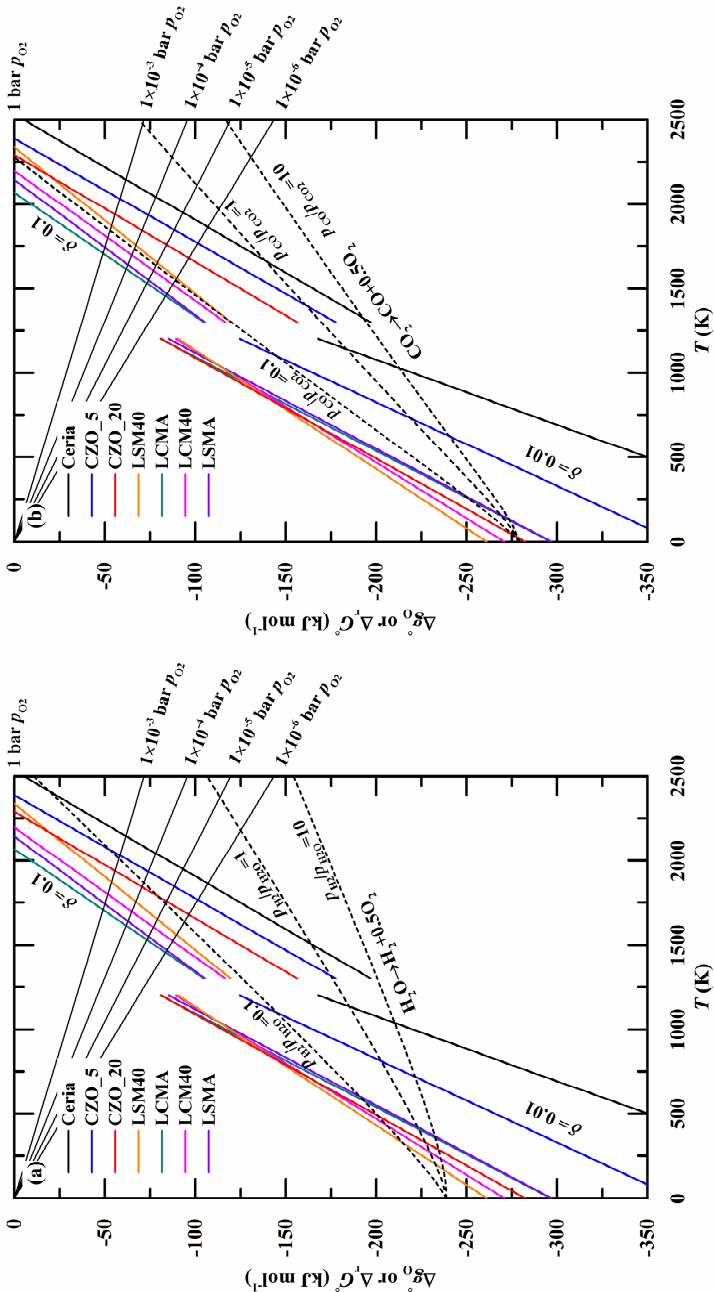


Figure 3.18. $\Delta \bar{g}_0^\circ$ for all the materials investigated for $\delta = 0.10$, relevant for the reduction, and negative $\Delta \bar{g}_0^\circ$ for $\delta = 0.01$, relevant for the oxidation reaction. Dashed lines represent the Gibbs free energy change of (a): the H_2 oxidation reaction: $(-\Delta_r G_{\text{H}_2,0}^\circ)$ and of (b): the CO oxidation reaction: $(-\Delta_r G_{\text{CO},0}^\circ)$ for varying equilibrium fuel ratios. The metal oxide reduction reaction is at equilibrium at $\delta = 0.10$ at T where $\Delta \bar{g}_0^\circ(\delta = 0.10)$ crosses the corresponding p_{O_2} line (solid line). The oxidation with $\text{H}_2\text{O}/\text{CO}_2$ to $\delta = 0.01$ is thermodynamically favorable at T where $-\Delta \bar{g}_0^\circ(\delta = 0.01)$ crosses the corresponding line of $-\Delta_r G_{\text{H}_2,0}^\circ$ or $-\Delta_r G_{\text{CO},0}^\circ$, respectively.

undoped ceria. Assuming reduction to $\delta = 0.1$ at $p_{\text{O}_2} = 1 \times 10^{-4}$ bar and oxidation to $\delta = 0.01$ with $p_{\text{H}_2}/p_{\text{H}_2\text{O}} = 1$, temperature swing is 905 K for undoped ceria, 1125 K for CZO_5 and 1210 K for LCMA. This reflects the findings from above, namely that all the investigated materials show more favorable reduction thermodynamics compared to undoped ceria, however, less favorable oxidations thermodynamics yielding in larger temperature swings between reduction and oxidation.

Chapter 4

Overall rates of metal oxide structures under solar conditions³

This chapter investigates the overall rates of redox reactions, including heat and mass transport phenomena, using a solar-driven thermogravimetric analyzer (solar-TG), in which the RPC structures are directly exposed to high-flux irradiation while their mass change is continuously monitored. With this arrangement, the overall rates of thermochemical reactions can be determined under similar radiative heat transfer characteristics typical of high-temperature solar reactors operated in concentrating solar systems, such as solar towers and dishes, thus mimicking realistic operating conditions.^{90, 91} The O₂ and CO evolutions are analyzed during reduction and oxidation, respectively, of SS-RPC, DS-RPC, and fibers made of undoped ceria. Additionally, DS-RPC samples made of ceria doped with 10 and 20 mol% Zr⁴⁺ are compared to those made of undoped ceria. The sample morphology before and after redox cycling is investigated by scanning electron microscopy (SEM); the phase composition by powder X-ray diffraction (XRD).

³ Material from this chapter has been published in: M. Takacs, S. Ackermann, A. Bonk, M. Neises-von Puttkamer, Ph. Haueter, J.R. Scheffe, U. Vogt and A. Steinfeld, "Splitting CO₂ with a Ceria-Based Redox Cycle in a Solar-Driven Thermogravimetric Analyzer", *AIChE Journal*, doi:10.1002/aic.15501

4.1 Experimental section

4.1.1 Sample preparation and characterization

DS- and SS-RPC samples of composition $Zr_xCe_{1-x}O_2$ ($x = 0, 0.1, \text{ and } 0.2$) were produced by the replication method.¹¹¹ CeO_2 powder (Sigma Aldrich, 99.9% purity, particle size $< 5\mu\text{m}$), stoichiometric amounts of ZrO_2 (Tosoh, TZ-0, 99.95% purity, surface area $14.5\text{ m}^2\text{ g}^{-1}$), and 30 vol% spherical carbon pore-forming agent particles (HTW Hochttemperatur-Werkstoffe GmbH, Sigradur K, particle size $0.4 - 12\ \mu\text{m}$) were mixed with water in a 5:1 mass ratio. 0.84 wt% organic deflocculating agent (Zschimmer & Schwarz, Dolapix CE64), 20 wt% polyvinyl alcohol binder (PVA, Zschimmer & Schwarz, Optapix RA 4G) and antifoaming agent (Zschimmer & Schwarz, Contraspum KWE) were added and processed according to a previously reported recipe.^{40, 67} Organic polyurethane sponges (Foam Partner, Fritz Nauer AG) with 8, 10, and 35 ppi were then immersed into the slurry, dried in air, and finally sintered for 5 h at 1873 K. The solid-to-water ratio was decreased linearly for the ZrO_2 containing RPCs from 5:1 for $x = 0$ to 4.8:1 for $x = 0.2$ due to the increasing viscosity with increasing ZrO_2 content. Figure 4.1 shows photographs of the ceria RPC structures with 8, 10, and 35 pores per inch (ppi) in the mm-scale, and 18% porosity within the struts in the μm -scale. The approximate dimensions of all the RPC samples after sintering were 30 mm diameter and 18 mm thickness. Also shown is a photo of the commercially available ceria fiber sample (Zircar Zirconia, 88% porosity, mean fiber dimensions: $7\ \mu\text{m}$ -diameter, $100\ \mu\text{m}$ -length). The 10 ppi ceria SS-RPC is the sample with the highest density (2.12 g cm^{-3}) because of its non-porous struts. Among the DS-RPC with porous struts, the 10 ppi sample has the highest density because of its small mm-sized pores and large strut thickness. The strut thickness depended on the viscosity of the slurry and on the number of coating layers. The 8 and 10 ppi RPC

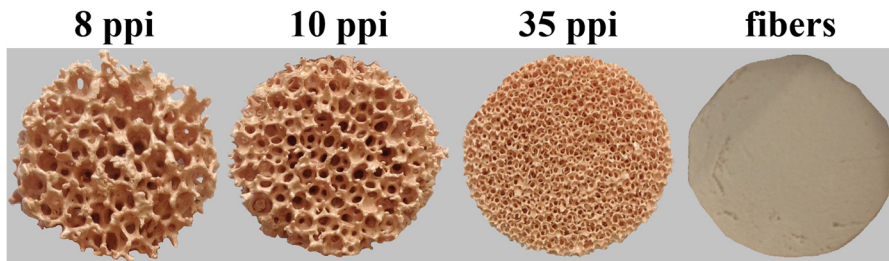


Figure 4.1. Photographs of ceria DS-RPC structures with 8, 10 and 35 ppi in the mm-scale and 18% porosity within the struts in the μm -scale. Also shown is the ceria fiber sample with 88% porosity in the μm -scale.

samples were coated twice, while the 35 ppi RPC sample was coated only once because of the small mm-size pores. The different values of density of the Zr-doped RPC samples were also due to the strut thickness obtained during manufacturing with a different slurry when adding Zr. XRD was performed in parallel-beam geometry using Cu K α radiation (Philips, PANalytical/X'Pert MPD/DY636, $\lambda = 1.5418 \text{ \AA}$, $2\Theta = 20 - 95^\circ$, $1.0^\circ \text{ min}^{-1}$ scan rate). XRD patterns (shown in Appendix B.1) show the formation of single phase face centered cubic (fcc) structures for all compositions of $\text{Zr}_x\text{Ce}_{1-x}\text{O}_2$. A shift of the reflections indicates a contraction of the ceria lattice due to the substitution of Ce^{4+} (0.97 \AA) by isovalent Zr^{4+} (0.84 \AA).¹¹² SEM was performed on an ESEM XL30 Microscope (FEI, 10 kV accelerating voltage). SS-RPC structures made of Al_2O_3 with same dimensions were identically fabricated for the thermogravimetric buoyancy correction.

4.1.2 Experimental set-up

The solar-driven thermogravimetric analyzer is schematically shown in Figure 4.2. The setup consists of an Al_2O_3 rod of 12 mm outer diameter, 340 mm length, and 2 mm wall thickness, suspended on top of a balance (WMS404C, Mettler Toledo, 0.1 mg accuracy) and enclosed in a stainless

steel housing. The RPC sample is placed on top of a ZrO_2 porous platform (30 ppi, Spohr GmbH, 24 mm height, 30 mm diameter) positioned on the Al_2O_3 rod. The RPC sample is covered with a transparent quartz dome (Schmizo, 70 mm outer diameter, 150 mm height, 2.5 mm wall thickness) that is sealed to the metallic housing with a refrigerated O-ring flange. The temperature of the bottom of the RPC is measured by a type-S thermocouple and transmitted wireless (Omega, MWTC-A-S-868 and MWTC-REC6) to eliminate disturbance of the balance. Temperatures are also measured along the centerline of the RPC at $z = 2, 7,$ and 12 mm below the top surface of the RPC in separate experiments where the balance is disconnected (accuracy of the thermocouple placement was ± 2 mm). A refrigerated brass jacket (63 mm outer diameter, 48 mm inner diameter, 76 mm length) lined with an Al_2O_3 fiber ring (4 mm thickness, 64 mm height) is placed around the RPC on the inner side of the quartz dome. A tangential gas inlet through the top of the quartz dome enables the injection of Ar sweep gas during the reduction step and of CO_2 during the oxidation step. Additionally, Ar is injected through the bottom of the metallic housing to prevent product gases flowing towards the balance. The product gas exits through an outlet port located 100 mm below the RPC and is cooled by a gas cooler (AGT Thermotechnik GmbH, MAK 10). Mass flow rates are electronically controlled (Bronkhorst HIGH-TECH B.V., EL-FLOW). The product gas composition is analyzed by infrared (IR) sensors for CO and CO_2 and an electrochemical sensor for O_2 (Siemens Ultramat 23), and verified by gas chromatography (Varian, CP-4900 Micro GC).

Experimentation was performed at the High-Flux Solar Simulator (HFSS) of ETH Zurich. An array of seven Xe-arcs, close-coupled to truncated ellipsoidal reflectors, provided an external source of intense thermal

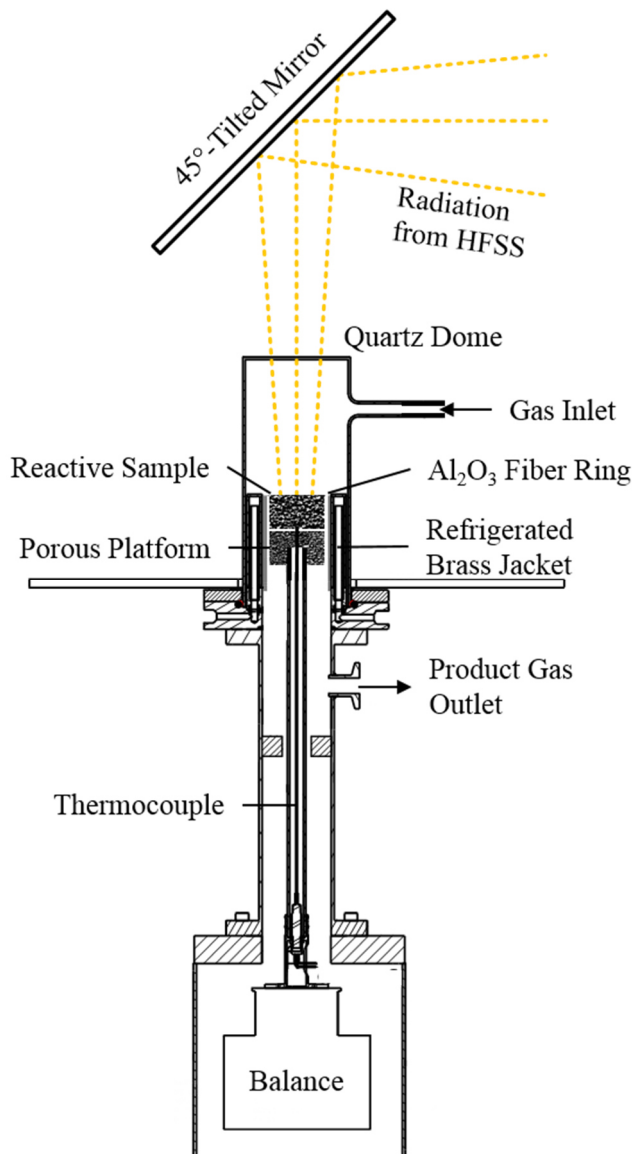


Figure 4.2. Schematic of the solar-driven thermogravimetric analyzer. Concentrated radiation delivered by the High-Flux Solar Simulator (HFSS) is redirected by a 45° -tilted mirror, enters the setup through a transparent quartz dome, and is incident on the RPC sample whose weight change and gas evolution are temporally monitored.

radiation, mostly in the visible and IR spectra, that closely approximates the heat transfer characteristics of highly concentrating solar systems.¹¹³ The concentrated radiation was redirected by a 45°-tilted mirror and focused on the top surface of the RPC. The radiative flux distribution on the plane of that surface was determined prior to the solar-TG runs by using a CCD camera (BASLER, A 1021) focused on a water-cooled, Al₂O₃ plasma-coated Lambertian (diffusely reflecting) target. The total solar radiative power input on the sample surface was calculated by flux integration and verified by water calorimetry.

During a typical redox cycle, the system was first purged with Ar (Messer, Argon 4.6) until $p_{O_2} < 0.2$ mbar was reached in the outlet gas. At time $t = 0$ min, the HFSS was switched on and the RPC sample was exposed to a mean radiative flux of 128 W cm⁻² (1280 suns) under an Ar gas flow of 0.5 L min⁻¹. After 10 min of reduction, the radiative flux was decreased to 44 W cm⁻² (440 suns) and the samples cooled for 30 s. Afterwards, the gas flow was switched to 0.5 L min⁻¹ CO₂ (Messer, Carbon Dioxide 4.8). After 9 min of oxidation with CO₂, the next cycle was initiated by switching the gas flow back to Ar and increasing the solar flux. Note that, although the re-oxidation step is exothermic, the HFSS was not completely switched off to counter-balance the heat losses and maintain a constant T_{ox} . Three consecutive redox cycles were performed with each sample. In the first cycle the sample was heated from ambient temperature to T_{red} whereas in the second and third cycle it was heated from T_{ox} . Buoyancy effects were accounted by subtracting the weight change obtained with blank runs using unreactive samples made of Al₂O₃ and having equivalent porous structures, namely 8, 10, and 35 ppi RPC and fibers. Although it was not possible to apply the buoyancy corrections at the exact same temperature for each reactive sample, the maximum relative temperature difference was less than 6.4%, 8.0%, 4.0% and 3.8% for the 8, 10, and 35 ppi RPC and the fiber sample,

respectively. This, in turn, led to an uncertainty in the weight change measurement of less than 7% of the absolute measured weight change for all samples at all times. Since the solar radiative input power and the solar radiative fluxes incident on the RPC are main design parameters of the solar reactor, O₂ and CO evolutions are compared for samples exposed to the same incident radiative fluxes, i.e., 1280 suns during reduction and 440 suns during oxidation for all experimental runs. This way, the effect of the porous structure (porosity and pore size) on the overall kinetics can be assessed, including heat and mass transfer limitations during both redox steps, and the results can be directly applied to guide the design of these structures for solar reactors.

4.2 Results and discussion

Figure 4.3 shows a representative solar-TG run with the 10 ppi ceria DS-RPC (19 mm height, 18.4 g mass): (a) shows temperature as a function of time at $z = 2, 7,$ and 12 mm below the top surface of the RPC; (b) shows the corresponding weight change, and (c) shows the corresponding specific gas evolution rates. The RPC was heated at an average rate of 100 K s⁻¹ for the first 10 seconds at $z = 2$ mm, faster than at the center and bottom because radiation was efficiently absorbed in the first layers while heat was internally transferred to the bottom by combined conduction, convection, and re-radiation. Approximate steady-state temperatures of 1900, 1670, and 1590 K were obtained at $z = 2, 7,$ and 12 mm, respectively. During reduction under Ar, the RPC underwent a weight decrease by 0.35% accompanied by O₂ evolution within the allotted 10 min. During oxidation with CO₂ at $T_{\text{ox}} = 1400, 1200,$ and 1110 K at $z = 2, 7,$ and 12 mm, respectively, the weight increased and CO evolved, but complete oxidation was not reached within the allotted 9 min.

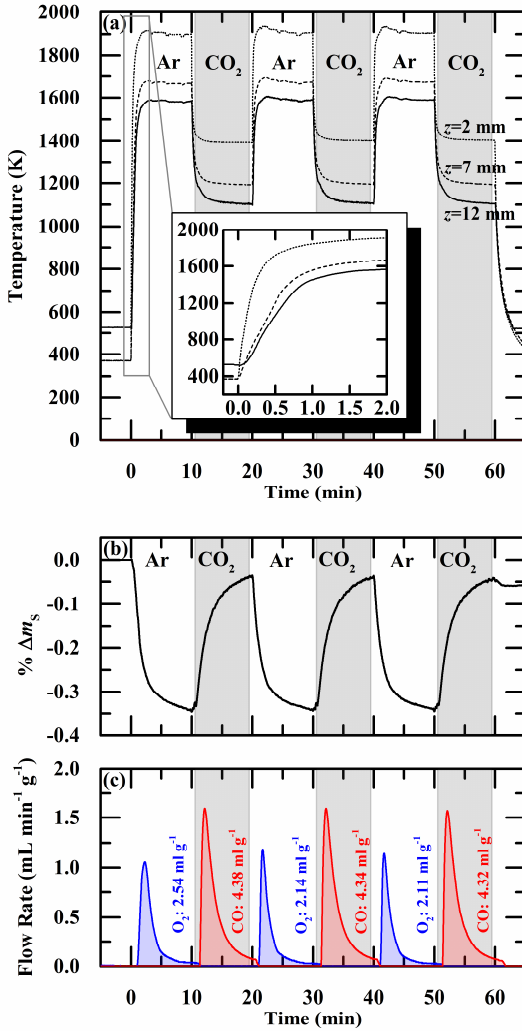


Figure 4.3. Solar-TG measurements for the 10 ppi ceria DS-RPC: (a) temperature as a function of time at $z = 2$ mm (dotted lines), 7 mm (dashed lines), and 12 mm (solid lines) below the top surface during 3 consecutive redox cycles; (b) corresponding % mass change; and (c) corresponding mass specific O₂ and CO evolution rates as well as the integrated mass specific O₂ and CO evolved.

For the 1st cycle, the specific O₂ and CO amounts evolved as obtained by integration of the curves of Figure 4.3(c) were 2.54 and 4.38 mL g⁻¹, respectively, yielding a CO:O₂ molar ratio of 1.72 due to the incomplete oxidation. During the subsequent cycles, CO:O₂ molar ratio was 2 ± 0.05 , confirming closed mass balance and full selectivity of CO₂ to CO. The total amount of O₂ released, as measured by the gas analysis, agreed well with the weight change measurement within 7%. Temporal variations of temperatures, weight, and gas evolution were reproducible during the three consecutive redox cycles.

4.2.1 Optical thickness

The influence of the sample's optical thickness on the heating rate and specific fuel yield was investigated by testing ceria DS-RPC with 8, 10, and 35 ppi as well as the ceria fiber sample (*cf.* Figure 4.1) of similar dimensions (RPCs: ~18 mm thickness, ~30 mm diameter; fiber sample: ~14 mm thickness, ~32 mm diameter) but different mass as listed in Table 4.1.

Table 4.1. Mass and density of the porous ceria samples.

Sample	Mass (g)	Density (g cm ⁻³)
8 ppi DS-RPC	16.42	1.26
10 ppi DS-RPC	18.41	1.41
35 ppi DS-RPC	11.63	0.89
fiber sample	9.65	0.86

The solar-TG measurements of these samples are shown in Figure 4.4: (a) the bottom temperature as a function of time during reduction of the 2nd cycle; and (b) the corresponding specific weight loss. The 8 ppi ceria RPC underwent the fastest heating, followed by the 10 ppi, the 35 ppi and the

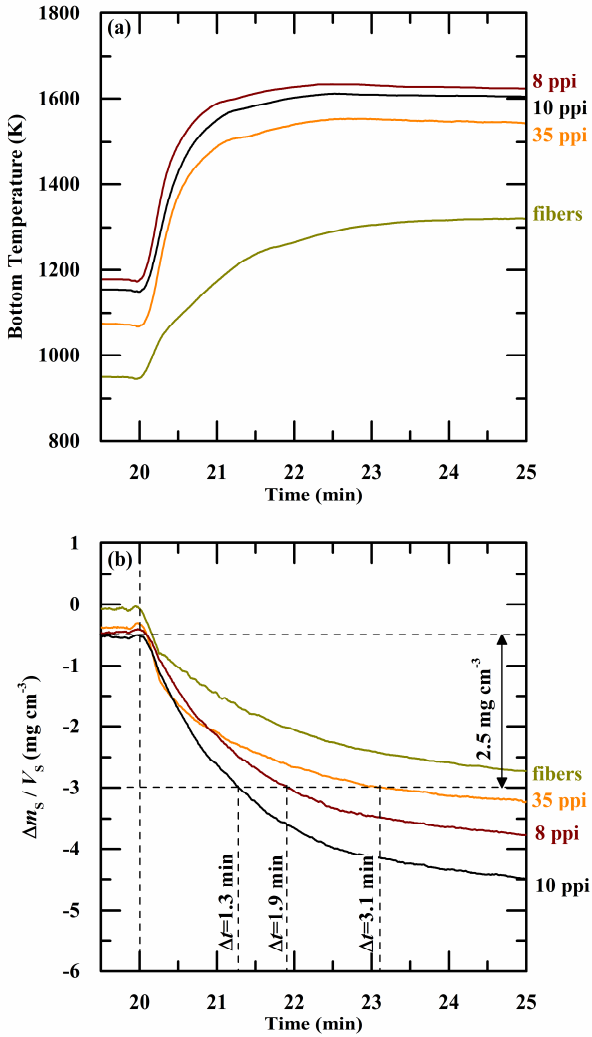


Figure 4.4. Solar-TG measurements of the 8 ppi, 10 ppi and 35 ppi ceria DS-RPC and the ceria fiber sample: (a) bottom temperature as a function of time during reduction; (b) specific weight change during reduction.

fiber sample. The average heating rate from 1200 to 1400 K was 16 K s^{-1} for the 8 ppi RPC, 12 K s^{-1} for the 10 ppi RPC and 11 K s^{-1} for the 35 ppi RPC. The steady-state temperatures achieved at the bottom of the RPC samples increased with the large-scale pore size, from around 1540 K for the 35 ppi to 1625 K for the 8 ppi, as a result of the deeper penetration and volumetric absorption of concentrated radiation. In contrast, the fiber sample achieved the lowest steady-state temperature of around 1330 K at the bottom because of opacity to incident radiation, leading to inefficient heating. Typical mean values of the effective extinction coefficient were 280 m^{-1} for the RPC and $40\,000 \text{ m}^{-1}$ for the fiber, indicating two orders of magnitude higher optical thickness for the latter.⁴⁰ The highest specific weight loss was observed for the 10 ppi RPC, even though the highest temperature was measured for the 8 ppi RPC, because of its high sample density (*cf.* Table 4.1) in combination with its relatively large pores. As the solar reactor is designed for a fixed RPC volume,^{40, 42, 67} the volume-specific weight loss of the RPC dictates the

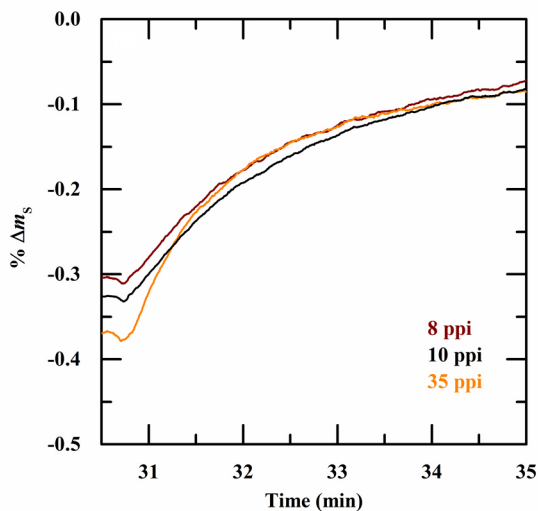


Figure 4.5. Percent weight change of the 8 ppi, 10 ppi and 35 ppi ceria DS-RPC during oxidation with CO_2 .

performance and not the mass-specific one. The time required for releasing 2.5 mg cm^{-3} of O_2 was approximately 1.3, 1.9, and 3.1 min for the 10, 8, and 35 ppi RPC, respectively. For a constant radiative power input of 128 W cm^{-2} , this implies that almost 140% more energy was needed to reduce the 35 ppi RPC compared to the 10 ppi RPC, which obviously affects detrimentally the solar-to-fuel energy conversion efficiency.⁴² The oxidation rates with CO_2 were very similar for all the RPC samples tested, as shown in Figure 4.5, because of their similar specific surface area ($0.066 \text{ m}^2 \text{ g}^{-1}$)⁶⁷ that is mainly determined by the μm -sized porosity of the struts. The 10 ppi DS-RPC produced the largest amounts of CO , as obtained by multiplying the curves in Figure 4.5 with the corresponding densities. Thus, because of the very similar oxidation rates, the redox performance of the various DS-RPC structures can be assessed by simply comparing their volume-specific O_2 release during reduction (*cf.* Figure 4.4).

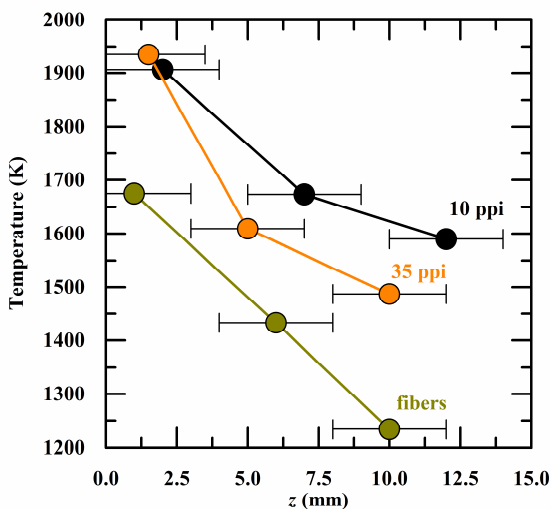


Figure 4.6. Temperatures along the centerline of the 10 ppi and 35 ppi ceria DS-RPC and the ceria fiber sample *versus* distance z below the top surface, measured at the end of the reduction step of the 2nd cycle for a radiative mean flux of 1280 suns.

The temperature distribution along the centerline of the RPC ($z = 0$ at the top surface), measured at the end of the reduction step of the 2nd cycle, is shown in Figure 4.6 for the 10 ppi and 35 ppi ceria DS-RPC and for the ceria fiber sample. Horizontal error bars account for ± 2 mm uncertainty in the thermocouple placement. The top surface, which is exposed to the high-flux radiation equivalent to 1280 suns, approached 1930 K for both RPC structures, but the bottom was 1590 and 1485 K for the 10 and 35 ppi RPC samples, respectively, i.e. a larger temperature gradient with decreasing pore size of approximately 32 and 53 K mm⁻¹ for the 10 and 35 ppi RPC samples, respectively. In contrast, the top of the ceria fiber did not exceed 1750 K, while the bottom was hardly heated during the reduction step, as a result of the optically thick medium for the visible and IR spectrum of the μm -size porosity.

Figure 4.7 shows the SEM images of strut brake planes of the 10 ppi ceria DS-RPC (1st row of images) and of the ceria fiber sample (2nd row of images): (a) locations where the SEM images were taken; (b,f) before redox cycling; (c,g) after redox cycling at the edge of the bottom surface; (d,h) after redox cycling at the edge of the top surface; and (e,i) after redox cycling at the center of the irradiated top surface. For the RPC, morphological changes are predominantly observed at the center of the irradiated top surface directly exposed to 1660 suns (*cf.* Figure B.2 in Appendix B.2), resulting in temperatures exceeding 1900 K that lead to grain growth and partial sintering of the μm -sized pores, as shown in Figure 4.7(e). Nevertheless, no significant decreases in redox performance was observed during 3 consecutive redox cycles (*cf.* Figure 4.3 for the 10 ppi ceria DS-RPC). For the fiber sample, grain growth was observed all over the sample, getting more pronounced towards the center of the irradiated top surface where the fiber structure was completely destroyed.

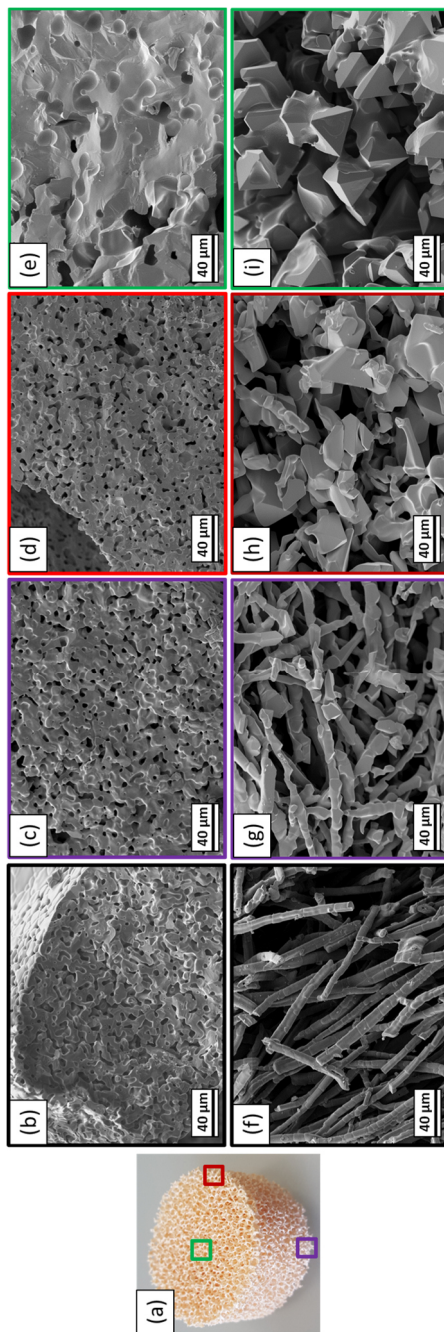


Figure 4.7. SEM images of the 10 ppi ceria DS-RPC (1st row) and of the ceria fiber sample (2nd row): (a) locations where the SEM images were taken; (b,f) before redox cycling; (c-g) after redox cycling at the edge of the bottom surface; (d,h) after redox cycling at the edge of the top surface; and (e,i) after redox cycling at the center of the irradiated top surface.

4.2.2 Single- versus dual-scale porosity

The influence of the strut porosity on the specific fuel yield was investigated by comparing the redox performance of the 10 ppi SS-RPC (no porous struts) and the 10 ppi DS-RPC (porous struts). Figure 4.8 shows the temporal variation during the 2nd redox cycle of: (a) the volume-specific O₂ and CO evolutions rates along with the bottom temperatures, (b) the cumulative mass-specific CO yield; and (c) the cumulative volume-specific CO yield. Integration of the O₂ and CO curves of Figure 4.8(a) reveals that the SS-RPC released more O₂ and consequently produced more CO compared to the DS-RPC, mainly because of its higher density of 2.12 g cm⁻³ for the SS-RPC *vs.* only 1.41 g cm⁻³ for the DS-RPC. However, due to the larger specific surface area of the RPC with μm-size strut porosity,⁶⁷ the DS-RPC exhibited faster oxidation rates, as shown in Figure 4.8(b). These results are in full agreement with the experiments carried out with a solar reactor, where time duration of the oxidation step was cut from 20 minutes for the SS-RPC to 8 minutes for the DS-RPC.⁴² On the other hand, Figure 4.8(c) confirms that, in terms of volume-specific fuel yields, the SS-RPC is superior to the DS-RPC because of the higher density.

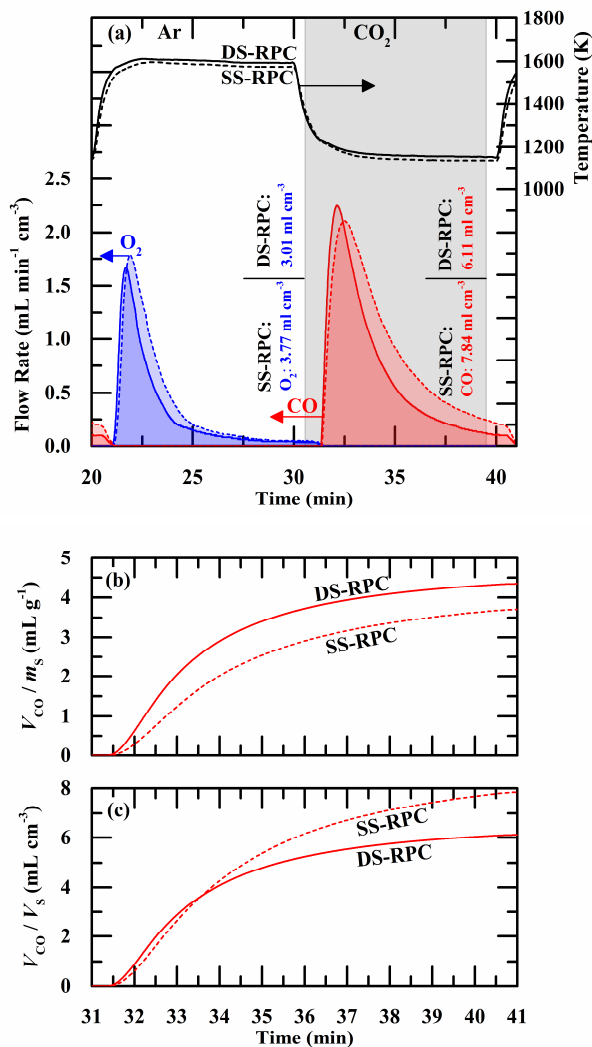


Figure 4.8. (a) Volume-specific flow rate of O₂ and CO as well as the bottom temperature of the RPC with single-scale porosity (SS-RPC) (dashed lines) and of the RPC with dual-scale porosity (DS-RPC) (solid lines) during the second redox cycle. Additionally, integrated mass specific O₂ release and CO yield are shown in (a). (b) Mass-specific and (c) volume-specific CO yield of both RPCs during the second oxidation.

4.2.3 Ceria versus Zr doped ceria

Figure 4.9 shows the percent weight change as a function of time during three consecutive redox cycles of the 10 ppi DS-RPCs made of undoped ceria, 10 mol% Zr⁴⁺ doped ceria (CZO_10), and 20 mol% Zr⁴⁺ doped ceria (CZO_20), as well as their corresponding bottom temperature. The corresponding mass-specific O₂ and CO evolutions are shown in (b) and (c), respectively. The highest mass loss was measured for CZO_20, followed by CZO_10 and undoped ceria, leading to a mass-specific O₂ release of 4.2 mL g⁻¹ for CZO_20, followed by 3.3 mL g⁻¹ for CZO_10 and 2.6 mL g⁻¹ for undoped ceria. This trend is in agreement with previous studies.^{44, 47-49, 62, 80} During the subsequent oxidation with CO₂, undoped ceria exhibited faster reaction rates and reached 80% oxidation extent to yield 4.4 mL g⁻¹ CO within the allotted oxidation time of 9 min. On the other hand, the oxidation of CZO_10 and CZO_20 was much slower and reached 50 and 25% oxidation extents, respectively, within 9 min to yield 2.8 and 1.5 mL g⁻¹, respectively, consistent with previous measurements.^{47, 114} Due to the incomplete oxidation, the O₂ release in the subsequent reduction steps decreased with higher Zr⁴⁺ dopant concentration. To check whether oxidation rates were restricted by thermodynamic limitations, the maximum oxidation extents (equilibrium δ) at $t=11.5$ min were determined by using thermodynamic data for Zr⁴⁺ doped ceria⁴⁹ and undoped ceria⁶⁴. CO partial pressures were determined from the temporal weight gain of the samples in combination with the CO₂ inlet flow rate; it was assumed that CO and CO₂ were perfectly mixed. With the knowledge of p_{CO} and p_{CO_2} the corresponding p_{O_2} was calculated according to:

$$p_{\text{O}_2} = \left(K_f^{-1} \frac{p_{\text{CO}_2}}{p_{\text{CO}}} \right)^2 \quad (4.1)$$

where K_f is the equilibrium constant for the formation of CO_2 obtained from NIST-JANAF thermochemical tables. Comparing the calculated thermodynamic weight losses to the measured ones reveals that the measured oxidation extents have not yet reached the thermodynamic limit. When assuming a constant RPC oxidation temperature of 1230 K, the measured weight change is 15, 40, and 300% lower than the thermodynamic limit for CZO_20, CZO_10, and undoped ceria, respectively. This is because the oxidation step was interrupted prior to its completion, as the reaction slowed down due presumably to high local CO concentrations, i.e., mass transfer limitations. Note, however, that the thermodynamic oxidation limit is closest to $\Delta m_s=0$ for ceria, followed by CZO_10 and CZO_20, which means that undoped ceria has the most favorable oxidation thermodynamics. Note that the temperature distribution of the RPC was not uniform (*cf.* Figure 4.6) and that the temporal p_{CO} inside the RPC is unknown; thus, a precise differentiation between thermodynamic and kinetic limitation is not possible.

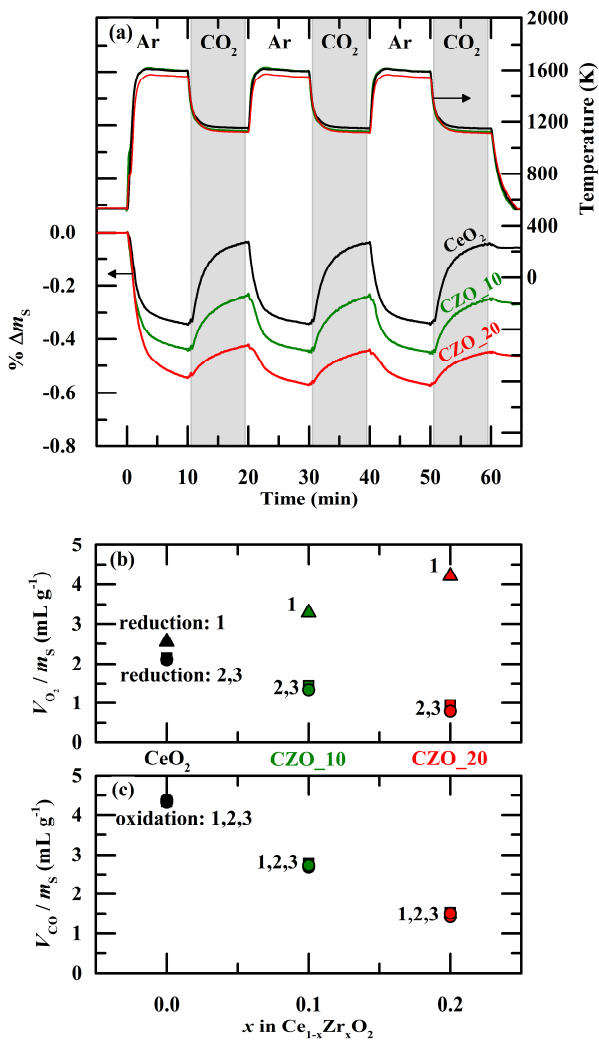


Figure 4.9. (a) Percent mass change and bottom temperature of the CeO_2 , CZO_10 and CZO_20 DS-RPC sample with 10 ppi during the three redox cycles. Mass specific O_2 release (b) and CO productivity (c) during reduction steps 1, 2 and 3 versus Zr^{4+} -dopant concentration x .

4.3 Conclusions

RPC structures with single- and dual-scale porosity made of undoped, 10 and 20 mol% Zr^{4+} doped ceria, as well as commercially available ceria fibers, were investigated for their redox performance to thermochemically split CO_2 under radiative heat flux characteristics of highly concentrating solar systems by using a solar-driven thermogravimetric analyzer. During three consecutive redox cycles, the porous samples were reduced in Ar under direct irradiation and subsequently oxidized with CO_2 to generate CO. The RPC with the largest mm-sized pores (8 ppi) featured efficient heat transfer because of its low optical thickness, as indicated by the relatively higher heating rate, higher measured bottom temperature and lower temperature gradient across the RPC. In contrast, the highest volume-specific O_2 release and CO yield was obtained with the 10 ppi RPC because of its higher sample density. SEM images revealed grain growth and partial sintering of the struts's μm -scale pores at the top surface of the RPC that was directly exposed to a radiative flux of 1660 suns. The DS-RPC with mm-sized porosity containing struts with μm -sized porosity exhibited faster oxidation rates than those for the SS-RPC with struts without porosity because of the higher specific surface area, but yielded less CO per unit volume because of the lower sample density. Although Zr^{4+} doped ceria showed increasing reduction extents with increasing dopant concentration, it could not be oxidized to a large extent due to unfavorable thermodynamics and slower kinetic rates, and hence yielded less CO compared to undoped ceria under the conditions investigated. The ceria fiber sample with only μm -sized porosity performed poorly in all aspects compared to the RPC due mainly to its opacity to incident irradiation. In conclusion, the 10 ppi ceria DS-RPC offers the best trade-off in terms of fast heating rates, temperature uniformity, fast reaction rates, and high specific fuel yields.

Chapter 5

Long term cycling stability of ceria RPCs

This chapter investigates the morphological and chemical stability of ceria RPC structures with single and dual-scale porosity. Ceria RPCs are cycled in a fast heating infrared furnace according to Eq. (1.2) and (1.3) at $T_{\text{red,set}} = 1673 - 1773$ K and $T_{\text{ox,set}} = 873$ K, whereas rate of heating and cooling is set to 600 K min^{-1} which results in a total cycle time of less than 15 min. The rate and yield of reduction and oxidation are measured by product gas analysis with a mass spectrometer. Morphological characterization before and after cycling is performed by scanning electron microscopy (SEM). Due to the fast heating and cooling rate, this setup allows to conduct more redox cycles per time compared to solar reactors^{40, 42} and other analytical setups such as thermogravimetric analyzers.

5.1 Experimental section

5.1.1 Synthesis technique and sample characterization

RPCs with single- and dual-scale porosity were fabricated by the replication method.¹¹¹ CeO₂ powder (Sigma Aldrich, 99.9% purity, particle size < 5 μm) and 30 vol% spherical carbon pore-forming agent particles (HTW Hochtemperatur-Werkstoffe GmbH, Sigradur K, particle size 0.4 - 12 μm or 10 – 20 μm) were mixed with water in a 5:1 mass ratio. 0.83 wt% organic deflocculating agent (Zschimmer & Schwarz, Dolapix CE64), polyvinyl alcohol binder (Zschimmer & Schwarz, Optapix RA 4G) and antifoaming agent (Zschimmer & Schwarz, Contraspum KWE) were added and processed according to a previously reported recipe.^{40, 67} Organic polyurethane sponges (Foam Partner, Fritz Nauer AG) with 10 ppi were then immersed into the slurry, dried in air and finally sintered for 1 h at $T = 1873$ K. Scanning electron microscopy of the RPC structures before and after redox cycling was conducted on a TM-1000Microscope (Hitachi, 15 kV accelerating voltage).

5.1.2 Experimental setup

The experimental setup is schematically shown in Figure 5.1. The setup's main component is an infrared radiation furnace (VHT-E48, Ulvac-Riko). The furnace consists of four quartz enclosed tungsten heating elements surrounded by gold coated water-cooled mirrors reflecting the infrared radiation towards the centerline of the furnace. The reactive sample is placed inside a sealed quartz tube (24 mm outer diameter, 1.5 mm thickness, 500 mm length). The quartz tube is surrounded by another quartz tube (50 mm outer diameter, 2.5 mm thickness, 360 mm length) to protect the heating elements and the gold coated surfaces from damage. The heated length of

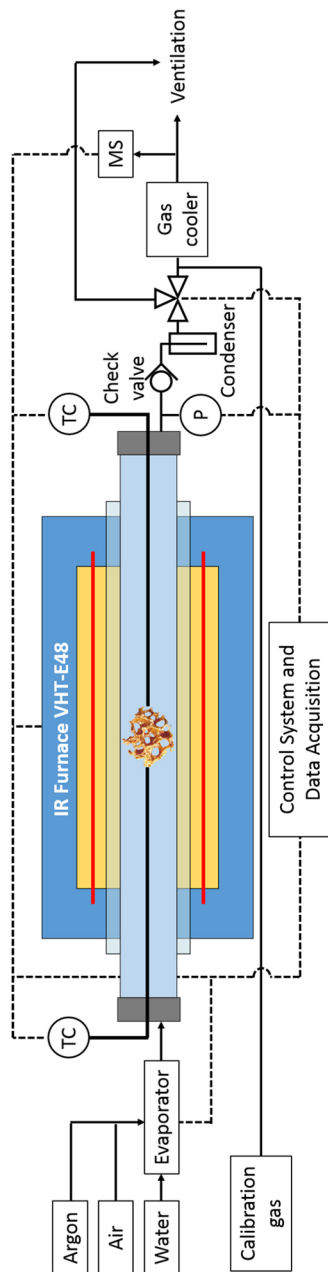


Figure 5.1. Schematic of the infrared furnace setup. The RPC sample is placed in the quartz tube located inside the IR furnace. Temperature is controlled and measured with two type-B thermocouples (TC). Sweep and oxidant gases are delivered with electronic mass flow controllers. Excess steam is condensed in a glass condenser and product gases are cooled in a gas cooler. The product gas composition is analyzed with a mass spectrometer. The overpressure inside the quartz tube, maintained by the check valve, is monitored with a pressure sensor (P) located at the product gas exit of the furnace.

the furnace is approximately 230 mm whereas the sample is placed at the center of the furnace. Two type-B thermocouples measure the sample temperature, one of them directly connected to the temperature controller of the furnace. Photographs of the IR furnace setup are shown in Figure 5.2.

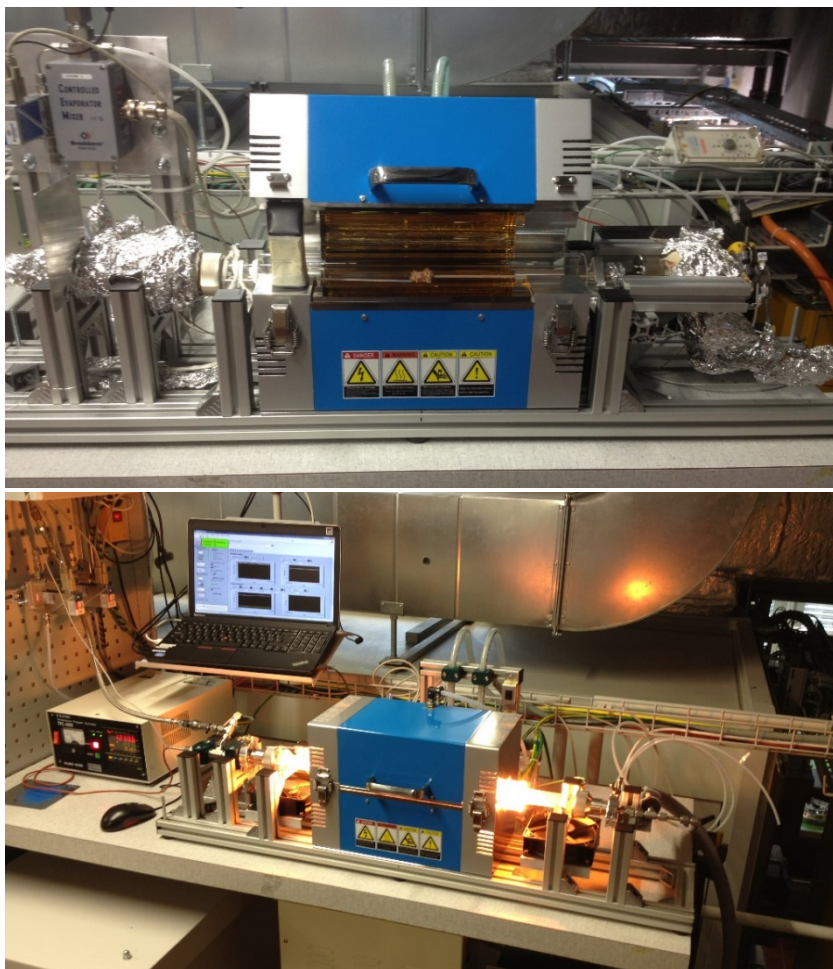


Figure 5.2. Photographs of the infrared furnace setup. Top: Open furnace with view on the ceria RPC sample and the thermocouples. Bottom: Infrared furnace in operation.

Argon (Messer, Argon 4.6) and synthetic air (Messer, Synthetic air pure) are delivered with electronic mass flow controllers (Bronkhorst, EL-FLOW). Steam is produced and delivered with a controlled evaporator (Bronkhorst, Controlled Evaporator Mixer, $T = 448$ K) connected to a liquid flow meter (Bronkhorst, Liqui-Flow). Gases flow to the reactive sample through insulated and heated pipes to avoid condensation of steam. Product gases are cooled and excess steam is condensed in a glass condenser (ACE Glass, Vacuum Trap). Afterwards, product gases are additionally cooled in a gas cooler (MAK 10, AGT Thermotechnik GmbH, $T = 275$ K) and analyzed with a mass spectrometer (MS) (GSD 320, Pfeiffer Vacuum). A pressure sensor (PSE54, SMC) measures the relative pressure of the gas stream at the exit of the furnace. A check valve is installed in between furnace and glass condenser resulting in a small overpressure of around 100 mbar inside the quartz tube. The overpressure in combination with the pressure sensor allows to detect failures of system components during operation (*e.g.* breaking of the quartz tube).

Typically, every day before starting an experiment, the MS was calibrated with four concentrations of N_2 , O_2 , H_2 , and Ar (Messer, Calibration gas mixture, 5.0 purity) within the range of measured product gas concentrations. Then, the system was purged with Ar until a $p_{O_2} < 0.1$ mbar was reached in the outlet gas. Afterwards, the RPC was heated with 100 K min^{-1} to the oxidation temperature $T_{\text{ox,set}} = 873$ K. Prior to the first reduction of the day, an oxidation step was conducted, consisting of the oxidation with 150 mL min^{-1} steam mixed with 300 mL min^{-1} Ar for 4 min, oxidation with 150 mL min^{-1} air mixed with 150 mL min^{-1} Ar for 0.5 min, followed by purging the system with 300 mL min^{-1} Ar for 3 min. To initiate reduction, the RPC was typically heated with 600 K min^{-1} to the reduction temperature and was kept for 4 min. Afterwards, the RPC was cooled with 600 K min^{-1} to the oxidation temperature where it was oxidized according to the

procedure shown above. O₂ evolution and H₂ production as well as the N₂ baseline were measured with the MS. After the last oxidation step, the RPC was cooled to room temperature with 100 K min⁻¹ and the MS was calibrated identically to before starting the experiment. During the last 3 min of each oxidation step, the MS was calibrated with the highest concentration of N₂, O₂, and H₂. This calibration procedure allows to accurately account for drifts in the MS measurement over day. Typically, around 25 redox cycles were conducted per day.

5.2 Results and discussion

As an example, Figure 5.3 shows measured specific O₂ evolution and H₂ production of the DS-RPC with small pores (0.4 – 12 μm pore former size, 2.005 g mass) as well as controlling temperature (solid line) and measured reference temperature (dashed line) of the RPC during 2 redox cycles between minute 110 and 140. At time 112 min, the DS-RPC was heated with 600 K min⁻¹ to $T_{\text{red,set}} = 1773$ K (setpoint reduction temperature) in Ar, resulting in the evolution of O₂ with a peak rate of 1.6 mL min⁻¹ g⁻¹. After 4 min reduction, the RPC was cooled with 600 K min⁻¹ to $T_{\text{ox,set}} = 873$ K where it was oxidized with steam to produce H₂ with a peak rate of 2.6 mL min⁻¹ g⁻¹. At $t = 123$ min, steam was switched off and air was delivered for 0.5 min to the sample to approach $\delta = 0^{60, 64}$ after each oxidation step. The integrated amount of O₂ was 1.65 mL g⁻¹ in both reduction steps whereas the amount of H₂ was 3.21 and 3.13 mL g⁻¹ for the prior and later oxidation step, respectively. This results in a H₂/O₂ ratio of 1.95 and 1.90, respectively. H₂/O₂ ≠ 2 is explained by the incomplete oxidation with steam within the allotted 4 min in combination with the complete oxidation with air. The differences in the temperature measurements (*cf.* solid and dashed lines in Figure 5.3) might be explained by temperature gradients along the RPC

sample and improper contact between thermocouple and RPC due to expansion and contraction of the RPC during redox cycling.

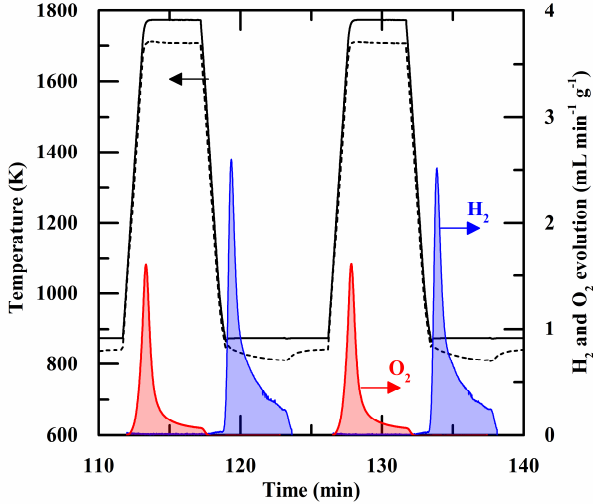


Figure 5.3. Typical specific O_2 evolution and H_2 production of the DS-RPC with the small pores ($0.4 - 12 \mu\text{m}$ pore former size) as well as controlling temperature (solid line) and measured reference temperature (dashed line) of the RPC during 2 redox cycles between minute 110 and 140.

5.2.1 H_2 rate dependence on temperature

In order to find the temperature where oxidation is fastest, H_2 production rate *versus* oxidation temperature was investigated with a DS-RPC with large pores ($10 - 20 \mu\text{m}$ pore former size, 3.318 g mass). The RPC was reduced at $T_{\text{red, set}} = 1673 \text{ K}$ and oxidized at temperatures from $T_{\text{ox, set}} = 773$ to 1073 K in 50 K steps, whereas temperature order was chosen randomly. The oxygen nonstoichiometry obtained after reduction was approximately $\delta_{\text{red}} = 0.016$.

As the oxidation rate not only depends on temperature but also on δ ,⁵⁹ the H_2 rate was determined at a constant δ . The mass specific H_2 rate at $\delta = 0.01$, 0.0075, and 0.005 *versus* oxidation temperature is shown in Figure 5.4. H_2 productivity was fastest at $T_{\text{ox,set}} = 873$ K and decreased towards higher and lower temperatures. At 873 K, 2.87 mL min⁻¹ g⁻¹ H_2 were produced at $\delta = 0.01$. At $\delta = 0.0075$ and 0.005, H_2 production was 2.72 and 2.23 mL min⁻¹ g⁻¹, respectively. Therefore, $T_{\text{ox,set}} = 873$ K was chosen as the oxidation temperature for all the cycling studies because of the fastest measured oxidation rate.

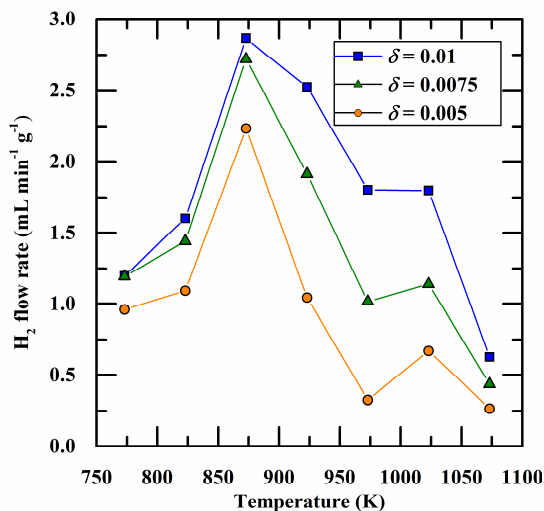


Figure 5.4. H_2 flow rate at $\delta = 0.01$, 0.0075, and 0.005 of the DS-RPC with large pores *versus* oxidation temperature. δ before oxidation was approximately $\delta = 0.016$, obtained after reduction at $T_{\text{red,set}} = 1673$ K.

5.2.2 Influence of pore size on cycling stability

DS-RPCs with large (10 – 20 μm pore former size) and small pores in the μm -range (0.4 – 12 μm pore former size) were reduced in Ar and oxidized with H_2O each for at least 100 times at $T_{\text{red,set}} = 1673$ and 1773 K. Figure 5.5(a) shows the O_2 yield (symbols) of the DS-RPC with large pores *versus* cycle number as well as the maximum mean reduction temperature \bar{T}_{red} during each cycle (lines). (b) shows the corresponding H_2 yields (symbols) and minimum mean oxidation temperatures \bar{T}_{ox} when flowing H_2O (lines). In (a) and (b), open symbols and solid lines correspond to the cycles at $T_{\text{red,set}} = 1773$ K, whereas closed symbols and dashed lines correspond to the cycles at $T_{\text{red,set}} = 1673$ K. Rather constant O_2 evolution and \bar{T}_{red} were observed over 175 and 100 cycles, respectively. Maximum variation in \bar{T}_{red} was 1%, for $T_{\text{red,set}} = 1673$ and 1773 K. Fluctuations in O_2 yield might be explained by daily start up and shut down effects (typically 25 cycles per day) and small changes in \bar{T}_{red} due to expansion and contraction of the RPC. The H_2 yield was rather constant over 100 cycles for $T_{\text{red,set}} = 1673$ K, but decreased slightly for $T_{\text{red,set}} = 1773$ K from more than 4.0 mL g^{-1} in the first cycles to ~ 3.3 mL g^{-1} in the last cycles. Additionally, decreasing H_2 yields over day were observed, whereas H_2 yield was largest always in the first cycles of the day. Maximum variation in \bar{T}_{ox} was $< 0.5\%$ and $< 1\%$ for $T_{\text{red,set}} = 1673$ and 1773 K, respectively. Figure 5.5(c) shows the H_2 flow rate at $\delta = 0.01$ for $T_{\text{red,set}} = 1673$ K (open circles) and $\delta = 0.02$ for $T_{\text{red,set}} = 1773$ K (\times - symbols). For $T_{\text{red,set}} = 1773$ K, the H_2 rate decreased by around 60% from 5.5 $\text{mL min}^{-1} \text{g}^{-1}$ in the first cycle to ~ 2.1 $\text{mL min}^{-1} \text{g}^{-1}$ in the last cycles. For $T_{\text{red,set}} = 1673$ K, the decrease was less pronounced.

Figure 5.6 shows the results for the DS-RPC with small pores. Labeling is identical to Figure 5.5. Similar to the RPC with large pores, O_2 yield was rather constant over 100 cycles. When neglecting cycle 1 and 2, maximum

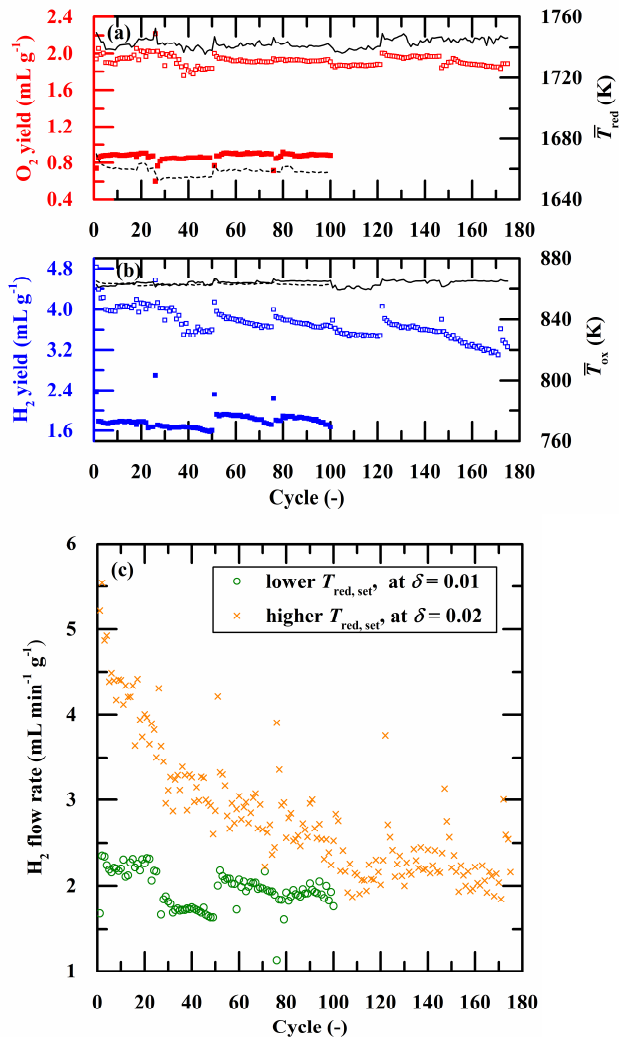


Figure 5.5. (a) O_2 yield (symbols) of the DS-RPC with large pores in the μm -range ($10 - 20 \mu\text{m}$ pore former size) versus cycle number as well as the maximum mean reduction temperature \bar{T}_{red} during each cycle (lines). (b) H_2 yield (symbols) and minimum mean oxidation temperature \bar{T}_{ox} (lines) versus cycle number. In (a) and (b), open symbols and solid lines correspond to the cycles with set reduction temperature $T_{\text{red,set}} = 1773$ K, whereas closed symbols and dashed lines correspond to the cycles at $T_{\text{red,set}} = 1673$ K. (c) Corresponding H_2 flow rate at $\delta = 0.01$ for $T_{\text{red,set}} = 1673$ K (open circles) and $\delta = 0.02$ for $T_{\text{red,set}} = 1773$ K (\times -symbols).

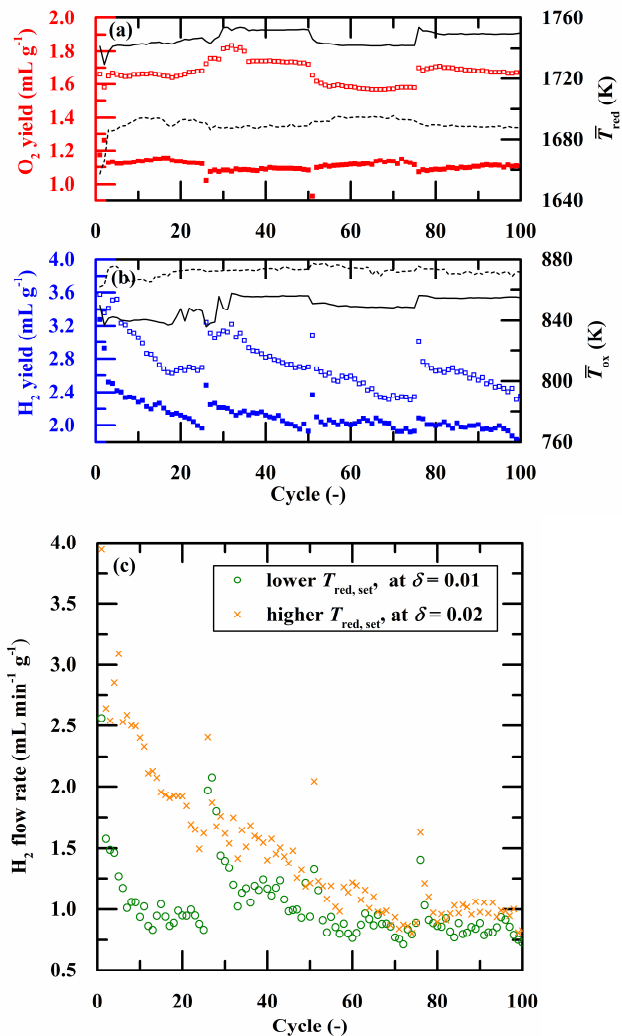


Figure 5.6. (a) O₂ yield (symbols) of the DS-RPC with small pores in the μm -range (0.4 – 12 μm pore former size) versus cycle number as well as the maximum mean reduction temperature \bar{T}_{red} during each cycle (lines). (b) H₂ yield (symbols) and minimum mean oxidation temperature \bar{T}_{ox} (lines) versus cycle number. In (a) and (b), open symbols and solid lines correspond to the cycles with set reduction temperature $T_{\text{red, set}} = 1773$ K, whereas closed symbols and dashed lines correspond to the cycles at $T_{\text{red, set}} = 1673$ K. (c) Corresponding H₂ flow rate at $\delta = 0.01$ for $T_{\text{red, set}} = 1673$ K (open circles) and $\delta = 0.02$ for $T_{\text{red, set}} = 1773$ K (\times -symbols).

differences in \bar{T}_{red} were 0.9% and 0.6% for $T_{\text{red,set}} = 1773$ and 1673 K, respectively. Variations in the O_2 yield for $T_{\text{red,set}} = 1773$ K (*e.g.* at cycle 51) correlate with \bar{T}_{red} because δ strongly depends on temperature at these conditions.^{62, 64} The H_2 yield showed a decreasing trend over 100 cycles, both for $T_{\text{red,set}} = 1673$ and 1773 K. For $T_{\text{red,set}} = 1673$ K, it decreased from > 3.2 mL g^{-1} in the first cycles to < 2.0 mL g^{-1} in the last cycles. For $T_{\text{red,set}} = 1773$ K, it decreased from > 3.5 mL g^{-1} in the first cycles to < 2.5 mL g^{-1} in the last cycles. Especially for $T_{\text{red,set}} = 1773$ K, daily variations in the H_2 yield were observed (*e.g.* at cycle 26 and 76) which might be explained by a slight change in \bar{T}_{ox} . Figure 5.6(c) shows the corresponding H_2 flow rates for the RPC with the large pores, similarly to Figure 5.5(c). Open circles show H_2 rates at $\delta = 0.01$ for $T_{\text{red,set}} = 1673$ K and \times -symbols at $\delta = 0.02$ for $T_{\text{red,set}} = 1773$ K. For $T_{\text{red,set}} = 1773$ K, the H_2 rate decreased by around 74% from 3.9 $\text{mL min}^{-1} \text{g}^{-1}$ in the first cycle to ~ 1.0 $\text{mL min}^{-1} \text{g}^{-1}$ in the last cycles. For $T_{\text{red,set}} = 1673$ K, the decrease was by around 70% from > 2.5 to ~ 0.8 $\text{mL min}^{-1} \text{g}^{-1}$.

The morphological changes during redox cycling were investigated by SEM. Figure 5.7 shows SEM images of DS-RPCs with small pores in the μm -range (0.4 – 12 μm pore former size): (a) before redox cycling; (b) after 1 reduction; (c) after reduction of the 2nd cycle; (d) after 25 cycles at $T_{\text{red,set}} = 1773$ K; (e) after 100 cycles at $T_{\text{red,set}} = 1773$ K ($\delta_{\text{red}} \approx 0.026$); and (f) after 100 cycles at $T_{\text{red,set}} = 1673$ K ($\delta_{\text{red}} \approx 0.017$). After the 1st reduction at $T_{\text{red,set}} = 1773$ K, cracks within ceria grains were observed (*cf.* Figure 5.7(b)), which have not been present in the fresh RPC, as shown in Figure 5.7(a). The cracks were also observed after the reduction of the 2nd cycle, whereas after 25 cycles, the cracks seem to be sintered together and smaller grains started to be formed within the larger ceria grains (*cf.* Figure 5.7(d)). The formation of the small grains was observed to be even more pronounced after 100 cycles,

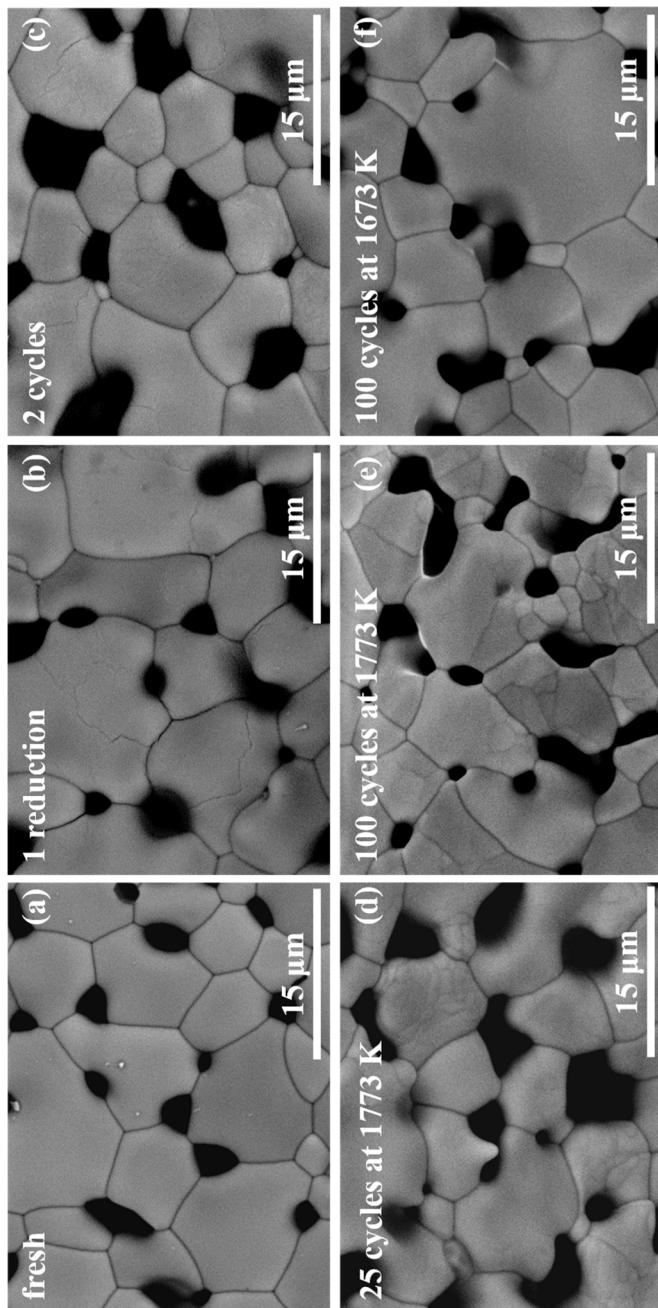


Figure 5.7. SEM images of DS-RPCs with small pores in the μm -range (0.4 – 12 μm pore former size): (a) before redox cycling; (b) after 1 reduction; (c) after reduction of the 2nd cycle; (d) after 25 cycles at $T_{\text{red,set}} = 1773 \text{ K}$; (e) after 100 cycles at $T_{\text{red,set}} = 1773 \text{ K}$ ($\delta \approx 0.026$); and (f) after 100 cycles at $T_{\text{red,set}} = 1673 \text{ K}$ ($\delta \approx 0.017$).

as shown in Figure 5.7(e). The initial grain size was in the range of 5 – 15 μm , whereas the new grains are only a few μm in size. Some of the large grains were already completely split into small grains after 100 cycles, whereas some of them show only first signs of grain splitting. The DS-RPC reduced at $T_{\text{red,set}} = 1673 \text{ K}$, did not show significant changes in morphology (e.g. cracking and grain splitting). Ackermann *et al.*⁵⁹ reported similar crack formation for dense ceria pellets when thermally and chemically reduced to $\delta_{\text{red}} = 0.034$ and 0.128, respectively. Bonk *et al.*¹¹⁵ reported crack formation for porous 15 mol% Hf doped ceria at 873 K in H_2 atmosphere. In both studies^{59, 115}, crack formation was more likely attributed to stresses due to chemical expansion and not due to thermal expansion.

5.2.3 Investigation of cracks within ceria grains

Due to the relatively fast oxygen diffusion within the ceria bulk,⁶⁰ reduction reaction of the DS-RPC under the conditions investigated above can be assumed to be thermodynamically limited, meaning, either limited by heat transfer or by the local p_{O_2} at the sample surface. To proof whether thermal expansion during heating^{116, 117} or chemical expansion during reduction^{94, 95, 118-120} caused the cracks within the ceria grains, heating and reduction of the RPC were decoupled. A DS-RPC with small pores was heated in air with 600 K min^{-1} to $T_{\text{red,set}} = 1773 \text{ K}$, kept for 4 min and cooled down with 600 K min^{-1} to room temperature. No cracks within the grains were observed as shown by SEM images in Figure 5.8(a). However, when heated the RPC in air and then isothermally (at $T_{\text{red,set}} = 1773 \text{ K}$) switched to Ar to initiate reduction, similar cracks as in Figure 5.7(b) were observed (*cf.* Figure 5.8(b)). Cracks were also observed when decreasing the heating rate to 50 K min^{-1} , as shown in Figure 5.8(c). This indicates that the chemical expansion results in cracks within the grains and not thermal expansion. In order to further investigate the influence of the rate of chemical expansion on the

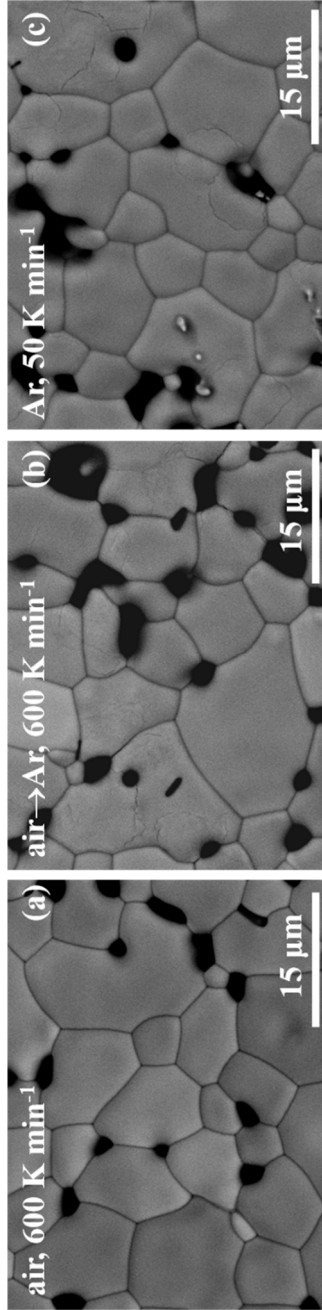


Figure 5.8. SEM of DS-RPCs with small pores in the μm -range ($0.4 - 12 \mu\text{m}$ pore former size): (a) heated in air with 600 K min^{-1} to $T_{\text{red,set}} = 1773 \text{ K}$; (b) heated in air with 600 K min^{-1} to $T_{\text{red,set}} = 1773 \text{ K}$, then isothermally reduced by switching from air to Ar; (c) reduced in Ar by heating with 50 K min^{-1} to $T_{\text{red,set}} = 1773 \text{ K}$.

cracking, a DS-RPC was cycled 20 times with a heating rate of 40 K min^{-1} to $T_{\text{red,set}} = 1773 \text{ K}$ followed by 25 cycles with a heating rate of 600 K min^{-1} . The reduction extent was kept approximately constant ($\delta_{\text{red}} \approx 0.027$) by adapting the time for the isotherm at $T_{\text{red,set}} = 1773 \text{ K}$. If the extent of grain cracking would increase with increasing rate of chemical expansion, one would expect the H_2 rates to be significantly faster at cycle 21 compared to cycle 1-20, due to an increased surface area. However, as shown in Figure 5.9, the H_2 rate stayed rather constant and was not affected by the increased heating rate, which indicates that rather the reduction extent dictates the amount of cracks and not the rate of reduction, at least for the conditions investigated.

Additionally, single-scale (SS) RPC structures with dense struts were cycled at $T_{\text{red,set}} = 1773 \text{ K}$ under identical conditions as the DS-RPCs shown above. The H_2 flow rate at $\delta = 0.025$ versus cycle number is shown in Figure 5.10.

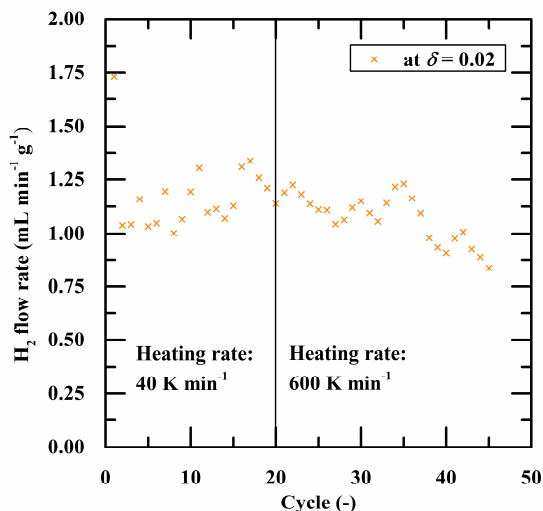


Figure 5.9. H_2 flow rate at $\delta = 0.02$ for the DS-RPC with small pores ($0.4 - 12 \mu\text{m}$ pore former size) versus cycle number. In cycle 1 – 20 the RPC was heated with 40 K min^{-1} to $T_{\text{red,set}} = 1773 \text{ K}$ whereas in cycle 21 – 45, the heating rate was 600 K min^{-1} .

Compared to the DS-RPCs, initially, the H_2 rate of the SS-RPC was approximately one order of magnitude lower. This can be explained by its dense struts and therefore lower specific surface area of $1.45 \times 10^{-4} \text{ m}^2 \text{ g}^{-1}$ compared to $0.066 \text{ m}^2 \text{ g}^{-1}$ for the DS-RPC.⁶⁷ The oxidation rate of the SS-RPC at $\delta = 0.025$ decreased by a factor of 10 from almost $0.4 \text{ mL min}^{-1} \text{ g}^{-1}$ in cycle 1 to $0.04 \text{ mL min}^{-1} \text{ g}^{-1}$ in cycle 59. After cycle 59, $\delta = 0.025$ was not even reached due to the very slow oxidation rates. Cycling was stopped after cycle 75. Figure 5.11 shows SEM images of: (a) a fresh SS-RPC; (b) a SS-RPC after 1 reduction and (c) after 75 cycles. The fresh SS-RPC exhibits a smooth grain structure without cracks. The average grain size is approximately 7 - 15 μm . After 1 reduction, the RPC grains show a lot of small cracks, which are even more pronounced than for the DS-RPC seen in Figure 5.7(b). After 75 cycles, the SS-RPC does not only show small cracks through the grains, but also large cracks all over the RPC struts, as shown in Figure 5.11(c). Similar to the observation of the DS-RPC, also the

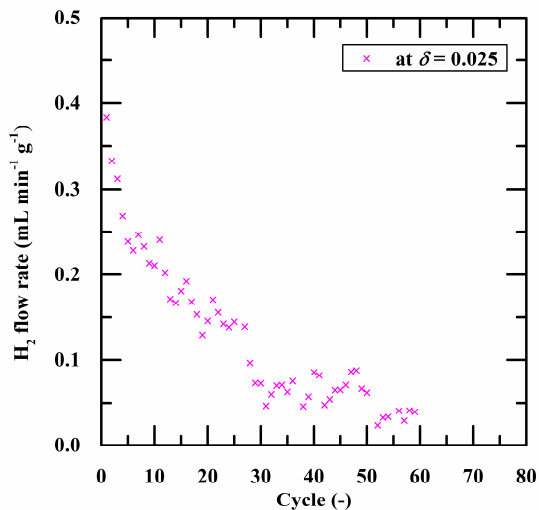


Figure 5.10. H_2 flow rate of the single-scale RPC at $\delta = 0.025$ versus cycle number for $T_{\text{red, set}} = 1773 \text{ K}$ with 600 K min^{-1} heating rate.

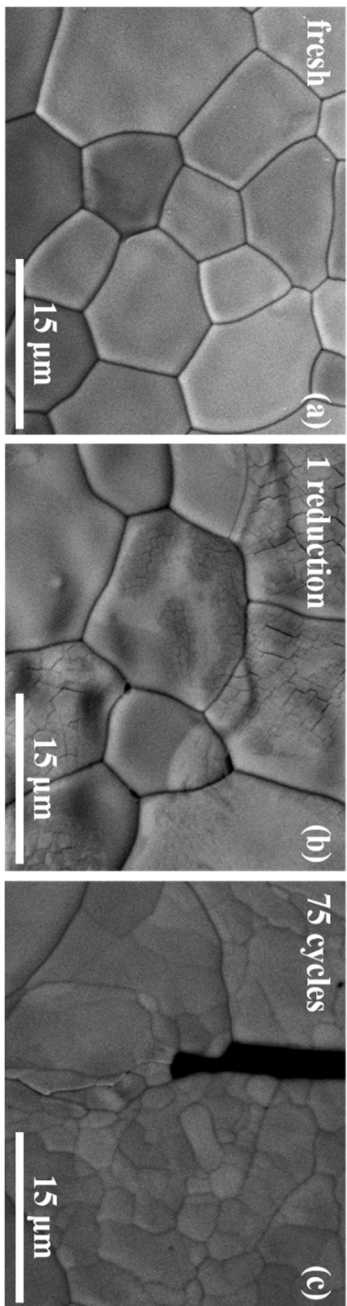


Figure 5.11. SEM images of SS-RPCs: (a) before redox cycling; (b) after 1 reduction; and (c) after 75 cycles at $T_{\text{red, set}} = 1773$ K.

grains of the SS-RPC split into smaller grains after some cycles. The average grain size of the small grains is only a few microns.

5.2.4 Long term cycling

A DS-RPC with small pores was cycled 500 times according to the procedure shown above whereat reduction time was decreased to 3.5 min and oxidation time with H₂O was increased to 5 min. Temperature was controlled with an Al₂O₃ shielded thermocouple located next to the RPC sample. Reduction temperature was set to 1673 K, however, $\delta > 0.035$ after reduction indicates an RPC temperature of > 1773 K when comparing the measured δ to thermodynamic data of ceria⁶⁴. The differences in temperatures might be explained by different optical properties of CeO₂ and Al₂O₃. O₂ and H₂ yield of the ceria RPC *versus* cycle number are shown in Figure 5.12(a). The corresponding H₂ rates at $\delta = 0.031$ are shown in Figure 5.12(b). H₂ production rate decreased by around 60% at $\delta = 0.031$ over the first 200 cycles but levels at 2 mL min⁻¹ g⁻¹. H₂ yield mirrors the decreasing H₂ rates whereas rather constant O₂ yield indicate chemical stability of the ceria RPC. H₂ yield decreased by 17% from 4.8 mL g⁻¹ in the first cycle to around 4 mL g⁻¹ in cycles 201-500. Figure 5.13 shows an SEM image of DS-RPCs after the 500 redox cycles. It can be seen that the surface structure is very similar to the samples shown in Figure 5.7.

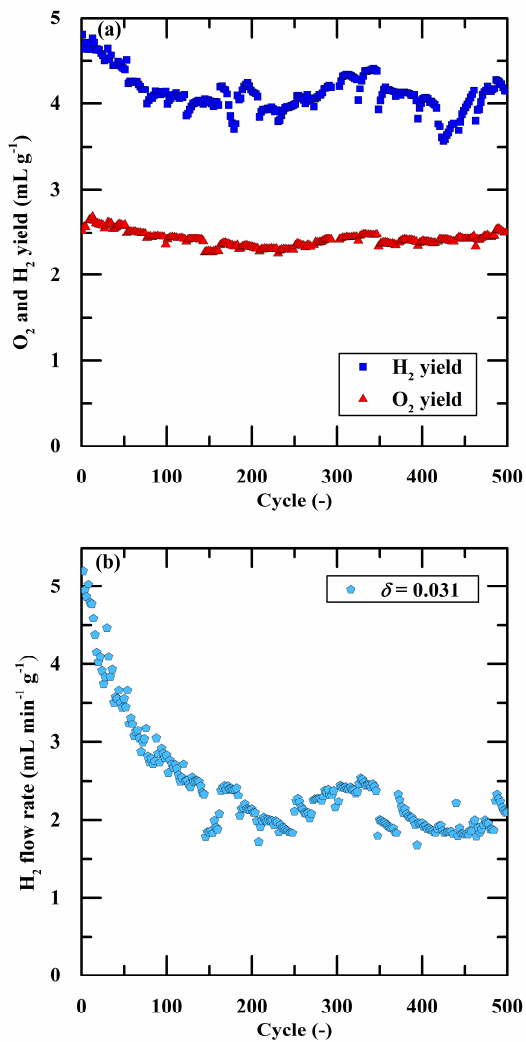


Figure 5.12. (a) O_2 and H_2 yield of the DS-RPC with small pores in the μm -range (0.4 – 12 μm pore former size) versus cycle number. (b) H_2 flow rate at $\delta = 0.031$ versus cycle number.

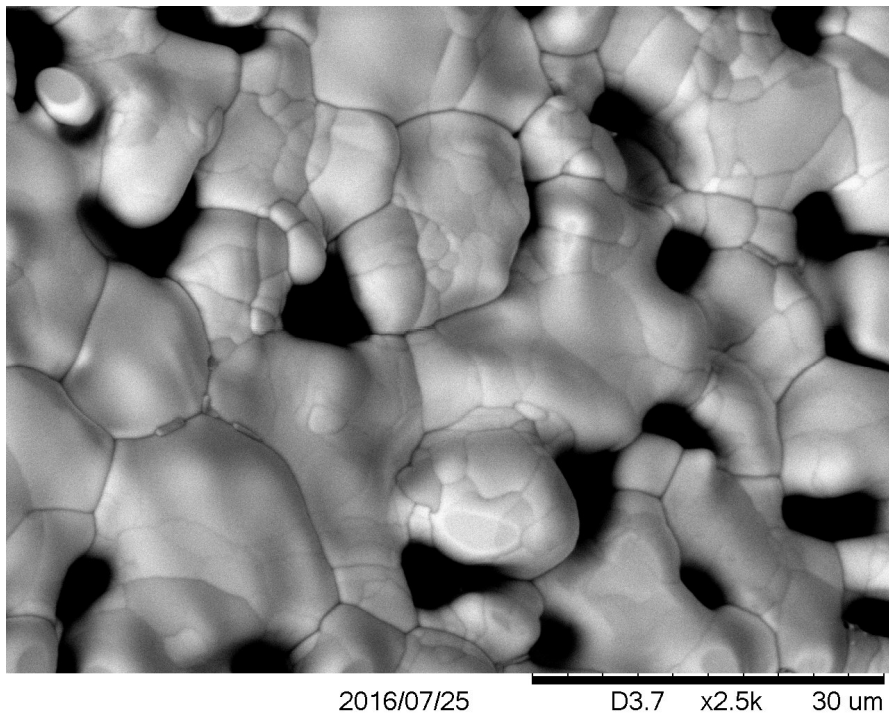


Figure 5.13. SEM image of DS-RPC with small pores in the μm -range ($0.4 - 12 \mu\text{m}$ pore former size) after 500 redox cycles at $T_{\text{red,set}} = 1773 \text{ K}$ ($\delta > 0.035$).

5.3 Conclusions

Long term chemical and morphological stability of reticulated porous ceramic (RPC) structures made of ceria (CeO_2) was tested in a fast heating infrared furnace setup. RPCs with single and dual-scale porosity were redox cycled for a varying number of times between reduction at temperatures $T = 1673$ and 1773 K and oxidation at $T = 873$ K with H_2O whereas heating and cooling rates were set to 600 K min^{-1} . It was shown by SEM images that cracks within ceria grains form within the first reduction at $T = 1773$ K due to chemical expansion of reduced ceria, resulting in relatively fast oxidation rates with H_2O due to the increased surface area. Then, over time, sintering of the cracks resulted in a decrease in surface area and hence slower H_2 production rates. For reduction at $T = 1773$ K, H_2 rates decreased by 75% over 100 cycles and 60% over 175 cycles for the dual-scale RPC with small and large μm sized pores, respectively, whereas it decreased by 90% over 59 cycles for the single-scale RPC. When reducing at $T = 1673$ K, morphology and H_2 rates were rather constant. Long term cycling of a dual-scale RPC revealed that H_2 production rate decreased by around 60% at $\delta = 0.031$ over the first 200 cycles but seems to level at $2 \text{ mL min}^{-1} \text{ g}^{-1}$ at $\delta = 0.031$ afterwards. H_2 yield mirrors the decreasing H_2 rates whereas rather constant O_2 yield indicate chemical stability of the ceria RPC.

Chapter 6

Outlook and research recommendations

The ultimate goal of the research on solar thermochemical H₂O and CO₂ splitting is to produce synthetic liquid fuels which are economically competitive with alternative renewable energy based fuels or even with fossil based fuels. An overall system efficiency of around 11% implying a reactor efficiency ($\eta_{\text{solar-to-fuel}}$) of 20% is expected to result in economically competitive fuels vis-à-vis other renewable energy based fuels.⁷⁹ It was theoretically shown in this work that reactor efficiency values exceeding 20% are unlikely to be reached with Zr⁴⁺ doped ceria, undoped ceria and the investigated lanthanum-manganese perovskites when not including heat recovery. The investigated doped ceria and lanthanum-manganese perovskites show more favorable reduction performance compared to ceria, however, show significantly worse oxidation behavior. This means that the goal of decreasing reduction temperatures or increasing reduction extents could be fulfilled by using these materials, however, on the cost that oxidation would have to be performed at lower temperatures or by flowing large amounts of excess oxidant gas, both implying an energy penalty to the process. Even though reduction temperatures could be lowered, 5 mol% Zr⁴⁺ doped ceria performs slightly worse compared to undoped ceria due to a larger temperature swing between oxidation and reduction and/or due to flowing more oxidant gas. This trade-off is even more pronounced for the

perovskites. Due to the unfavorable oxidation thermodynamics of the investigated materials, reaction rates, morphological and chemical stability as well as heat transfer characteristics were not investigated for Zr⁴⁺ doped ceria and the perovskites within this work. Coupled heat and mass transfer characteristics as well as morphological and chemical stability were mainly tested for undoped ceria.

A suitable nonstoichiometric metal oxide for efficient fuel production via two-step solar thermochemical H₂O and CO₂ splitting cycles must fulfill the following requirements:

- Favorable reduction and oxidation thermodynamics
- Fast oxygen diffusion within bulk
- Fast H₂O and CO₂ splitting kinetics
- Morphological stability
- Chemical stability
- Good heat transfer characteristics

Reduction and oxidation thermodynamics – It was shown that many materials exist that exhibit a more favorable reduction performance compared to ceria. However, the more favorable reduction performance comes on the costs of less favorable oxidation behavior. The goal must be to find a material having a more balanced redox performance meaning exhibiting a slightly improved reduction performance compared to ceria in order to lower the reduction temperature or increase the specific fuel yield but not having a significantly worse oxidation performance. Thermodynamically, the reason for the balanced redox performance of ceria is its relatively large partial molar entropy of $\Delta\bar{s}_0^\circ > 250 \text{ J mol}^{-1} \text{ K}^{-1}$ at low δ coupled with a relatively large partial molar enthalpy $\Delta\bar{h}_0^\circ > 450 \text{ kJ mol}^{-1}$. Additionally, the decrease of $\Delta\bar{h}_0^\circ$ with increasing δ favors the balanced thermodynamic performance of ceria. An improved redox material must not

have a partial molar entropy significantly lower compared to ceria, additionally, not have a much lower partial molar enthalpy and not have a much less steep decrease in enthalpy with increasing δ . It is not yet known whether such a perfect nonstoichiometric redox material exists, but in a first step it would be important to understand the fundamentals of the high partial molar entropy of undoped ceria. The fundamental understanding would allow to more efficiently screen for new redox materials and suitable dopants. Besides Zr^{4+} doped ceria, Hf^{4+} doped ceria also exhibits more favorable reduction performance compared to ceria.^{46, 47} The oxidation measurements of 10 mol% Hf^{4+} doped ceria shown by Scheffe *et al.*⁴⁷ indicate that oxidation performance of Hf^{4+} doped ceria might be slightly more favorable compared to Zr^{4+} doped ceria. However, from this data it cannot be distinguished whether oxidation rate is limited by thermodynamics or kinetics. The flexibility in tuning thermodynamic properties of ceria might be improved by using more than one sort of cations doped into the ceria lattice. However, due to the large amount of material combinations and dopant concentrations, a material screening with computational methods, such as density functional theory (DFT), is necessary before testing them experimentally. Regarding perovskites for H_2O and CO_2 splitting, this work focused on the influence of varying dopants, such as Sr^{2+} , Ca^{2+} and Al^{3+} on the resulting thermodynamic properties of the perovskite by keeping the dopant concentrations constant. In order to more efficiently screen for optimized redox materials, it is additionally important to evaluate the influence of the dopant concentrations on the resulting tunability of the thermodynamic properties and the influence on the material performance for solar H_2O and CO_2 splitting. In addition to material screening, a detailed thermodynamic efficiency model including realistic process assumptions coupled with a sensitivity analysis should be developed. Such a model should be able to optimize all the process conditions in terms of energy conversion efficiency for each redox material.

Additionally, it is crucial that such an efficiency model accounts for separation work for extracting fuel from the product gas. Especially for the oxidation with CO_2 in combination with materials exhibiting unfavorable oxidation performances, the energy penalty attributed to a low fuel concentration might significantly contribute to the overall energy input.

Oxygen diffusion within bulk and $\text{H}_2\text{O}/\text{CO}_2$ splitting kinetics –

Thermodynamically, the materials analyzed in this work did not improve the performance of undoped ceria under the conditions investigated. Therefore kinetic studies of these materials have not been performed. Once a thermodynamically better material compared to ceria is found, kinetic studies must be performed to evaluate the rates at which the redox material can be reduced and at which H_2 and CO can be produced. Slow reduction rates (e.g. oxygen diffusion within bulk) might result in an energy penalty due to longer reduction times under concentrated solar irradiation, whereas slower oxidation rates (H_2/CO production rate) could result in energy penalties because of low fuel concentrations in the product gas and because of larger temperature swings due to cooling of the reactor during oxidation.^{42,}

67, 70

Morphological and chemical stability – Morphological and chemical stability of ceria RPC structures was investigated in this work. Stability of Zr^{4+} doped ceria and the perovskites was not investigated due to their unfavorable thermodynamic properties. Ceria RPCs with different pore sizes (0.4 – 12 μm and 10 – 20 μm carbon pore former) were studied at reduction temperatures of 1773 and 1673 K and oxidation temperature of 873 K, whereas heating and cooling rates were fixed to 600 K min^{-1} . Morphological and chemical stability might not only depend on the varied parameters such as reduction temperature and pore size but also on heating and cooling rates, oxidant gas, oxidation temperature, reduction time and oxidation time. All these parameters were fixed for the cycling studies in this work. To get more

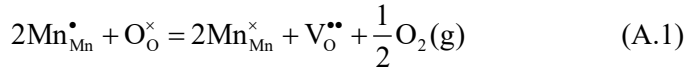
detailed information about the morphological and chemical stability, the influence of these parameters should also be addressed. Once new promising metal oxides are found, and thermodynamically and kinetically characterized, their chemical and morphological stability must be studied to ensure efficient fuel production over hundreds and thousands of cycles in an industrial solar plant.

Heat transfer characteristics – Combined heat and mass transfer characteristics of ceria and Zr^{4+} doped RPCs were investigated in the solar-TG. This device allows to test new redox materials and structures under similar heat and mass transfer characteristics as in solar towers and dishes. Therefore, once a new promising material is characterized in terms of thermodynamics, kinetics, chemical and morphological stability, its performance can be tested in the solar-TG where, compared to a solar reactor, much less material is needed to get first insights in its reduction and fuel production behavior under solar conditions. Additionally, material properties affecting the heat transfer, such as specific heat capacity, heat conductivity and optical reflectivity, should be determined over the operating range of the metal oxide.

Appendix

Appendix A: Derivation of defect model for perovskites

The reduction of LaMnO₃ perovskites with Sr/Ca A-site and Al B-site doping (La_{1-x}A_xMn_{1-y}B_yO₃) in the oxygen-deficient region might be described by



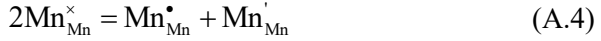
where tetravalent manganese ($\text{Mn}_{\text{Mn}}^{\bullet}$) on manganese lattice sites and oxygen atoms on oxygen lattice sites ($\text{O}_{\text{O}}^{\times}$) are in equilibrium with gaseous oxygen, trivalent manganese on manganese lattice sites ($\text{Mn}_{\text{Mn}}^{\times}$) and doubly ionized oxygen vacancies ($\text{V}_{\text{O}}^{\bullet\bullet}$). By applying the law of mass action, assuming activity coefficients equal 1 and a standard pressure $p^{\circ} = 1$ bar, the equilibrium constant for reaction (A.1) can be defined as:

$$K_1 = \frac{[\text{V}_{\text{O}}^{\bullet\bullet}][\text{Mn}_{\text{Mn}}^{\times}]^2}{[\text{O}_{\text{O}}^{\times}][\text{Mn}_{\text{Mn}}^{\bullet}]^2} (p_{\text{O}_2} / p^{\circ})^{1/2} \quad (\text{A.2})$$

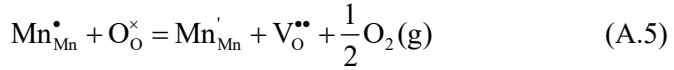
where square brackets denote concentrations taken as sublattice site fractions, *e.g.* for oxygen vacancies defined as:

$$[\text{V}_{\text{O}}^{\bullet\bullet}] = \frac{n_{\text{V}_{\text{O}}^{\bullet\bullet}}}{n_{\text{V}_{\text{O}}^{\bullet\bullet}} + n_{\text{O}_{\text{O}}^{\times}}} \quad (\text{A.3})$$

Trivalent manganese in Eq. (A.1) can further disproportionate to tetravalent and divalent manganese (Mn_{Mn}') according to:



By combining Eq. (A.4) with Eq. (A.1), the disproportionation reaction can be written as:



with the equilibrium constant

$$K_2 = \frac{[\text{V}_{\text{O}}^{\bullet\bullet}][\text{Mn}_{\text{Mn}}']}{[\text{O}_{\text{O}}^{\times}][\text{Mn}_{\text{Mn}}^{\bullet}]} \left(p_{\text{O}_2} / p^{\circ} \right)^{1/2} \quad (\text{A.6})$$

Site balances for manganese and oxygen

$$\begin{aligned} n_{\text{Mn}_{\text{Mn}}^{\bullet}} + n_{\text{Mn}_{\text{Mn}}^{\times}} + n_{\text{Mn}_{\text{Mn}}'} &= 1 - y \\ n_{\text{O}_{\text{O}}^{\times}} + n_{\text{V}_{\text{O}}^{\bullet\bullet}} &= 3 \end{aligned} \quad (\text{A.7})$$

and charge neutrality

$$2n_{\text{V}_{\text{O}}^{\bullet\bullet}} + n_{\text{Mn}_{\text{Mn}}^{\bullet}} = x + n_{\text{Mn}_{\text{Mn}}'} \quad (\text{A.8})$$

allow to write K_1 and K_2 in terms of δ , p_{O_2} and the sublattice site fraction $n_{\text{Mn}_{\text{Mn}}'}$, as shown by

$$K_1 = \frac{\delta(1 + 2\delta - 2n_{\text{Mn}_{\text{Mn}}'} - x - y)^2}{(3 - \delta)(-2\delta + n_{\text{Mn}_{\text{Mn}}'} + x)^2} \left(p_{\text{O}_2} / p^{\circ} \right)^{1/2} \quad (\text{A.9})$$

$$K_2 = \frac{\delta n_{\text{Mn}_{\text{Mn}}'}}{(3 - \delta)(-2\delta + n_{\text{Mn}_{\text{Mn}}'} + x)} \left(p_{\text{O}_2} / p^{\circ} \right)^{1/2} \quad (\text{A.10})$$

The sublattice site fraction $n_{\text{Mn}_{\text{Mn}}}$ can be eliminated by combining Eq. (A.9) and Eq. (A.10), resulting in

$$\begin{aligned}
 & \underbrace{\frac{(4\delta^4 - 3\delta x^2 - 4\delta^3(3+x) + \delta^2 x(12+x))}{(-3+\delta)^2}}_a (p_{\text{O}_2} / p^\circ)^{1/2} K_1 \\
 & + (-1+2\delta-x+y)^2 K_2^2 + \frac{2\delta(-1+2\delta-x+y)(-1-2\delta+x+y)}{(-3+\delta)} \\
 & \cdot (p_{\text{O}_2} / p^\circ)^{1/2} K_2 + \underbrace{\frac{(4\delta^4 - 4\delta^3(-1+x+y) + \delta^2(-1+x+y)^2)}{(-3+\delta)^2}}_b \\
 & \cdot (p_{\text{O}_2} / p^\circ) = 0 \text{ and } \delta \neq 3
 \end{aligned} \tag{A.11}$$

The terms a and b of Eq. (A.11) can be simplified to:

$$a = \frac{\delta(x-2\delta)^2}{(-3+\delta)} \tag{A.12}$$

$$b = \frac{\delta^2(x+y-2\delta-1)^2}{(-3+\delta)^2} \tag{A.13}$$

By using Eq. (A.12) and (A.13), Eq. (A.11) can be simplified to:

$$\begin{aligned}
 & \frac{\delta(x-2\delta)^2}{(-3+\delta)} (p_{O_2} / p^\circ)^{1/2} K_1 + \underbrace{(-1+2\delta-x+y)^2}_{\alpha^2} K_2^2 \\
 & + \underbrace{\frac{2\delta(-1+2\delta-x+y)(-1-2\delta+x+y)}{(-3+\delta)} (p_{O_2} / p^\circ)^{1/2}}_{2\alpha\beta} K_2 \\
 & + \underbrace{\frac{\delta^2(x+y-2\delta-1)^2}{(-3+\delta)^2}}_{\beta^2} (p_{O_2} / p^\circ) = 0 \text{ and } \delta \neq 3
 \end{aligned}
 \tag{A.14}$$

By applying the binomial $(\alpha+\beta)^2 = \alpha^2+2\alpha\beta+\beta^2$ to Eq. (A.14) and taking the square root of it, Eq. (A.15) can be obtained.

$$\underbrace{\frac{\delta^{1/2}(x+y-2\delta-1)(p_{O_2} / p^\circ)^{1/4}}{(x-2\delta)(3-\delta)^{1/2}}}_Y = \frac{(3-\delta)^{1/2}(2\delta-x+y-1)}{\underbrace{\delta^{1/2}(x-2\delta)(p_{O_2} / p^\circ)^{1/4}}_X} K_2 - K_1^{1/2}
 \tag{A.15}$$

By plotting the measured nonstoichiometry data in the form Y versus X (cf. Eq. (A.15) and Figure A.1), K_1 and K_2 can be determined by linear regression. $-K_1^{1/2}$ equals the Y -intercept and K_2 the slope of the linear fit.

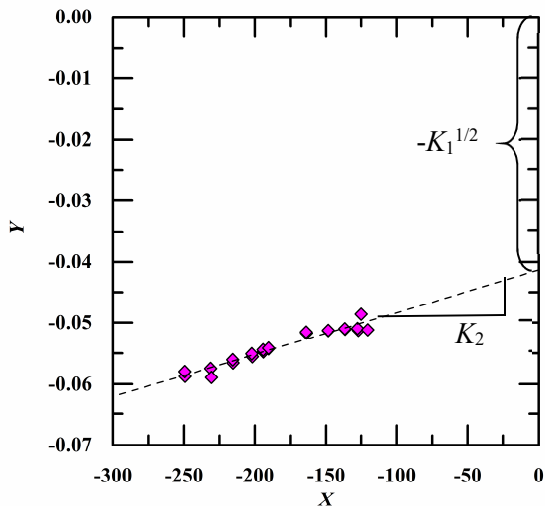


Figure A.1. Graphical representation of Eq. (A.15). X of LCM40 at $T=1673$ K is shown versus Y . The slope of the linear regression is equal to K_2 whereas the Y -intercept is equal to $-K_1^{1/2}$.

Appendix B: Solar-TG measurements

B.1 XRD patterns of samples for solar-TG measurements

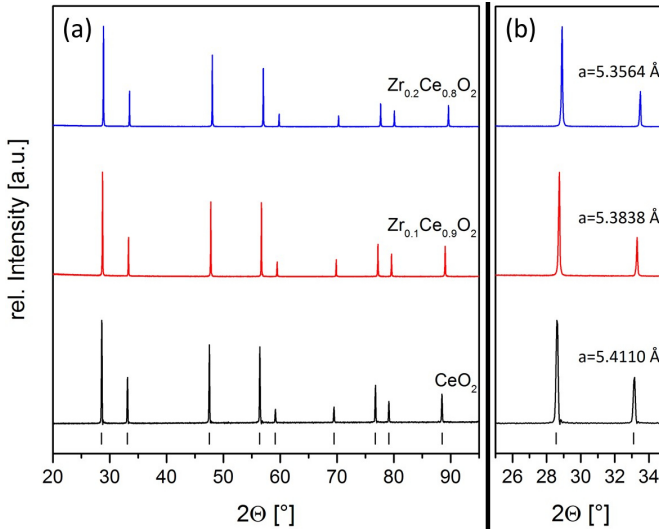


Figure B.1. (a) XRD patterns of $Zr_xCe_{1-x}O_2$ ($x = 0, 0.1, 0.2$) solid solutions after sintering at 1873 K and (b) zoom into the (111) and (200) reflections. Reflections are shifted towards higher angles for increasing Zr^{4+} -dopant concentration. Lattice parameters gained from Rietveld refinement are shown in (b). Vertical lines represent reflection positions of CeO_2 reference pattern (ICSD-Database).

XRD patterns of $Zr_xCe_{1-x}O_2$ ($x = 0, 0.1, 0.2$) solid solutions after sintering at 1873 K show the formation of single phase face centered cubic (fcc) structures for all compositions of $Zr_xCe_{1-x}O_2$ (*cf.* Figure B.1). A shift of the reflections indicates a contraction of the ceria lattice due to the substitution

of Ce^{4+} (0.97 Å) by isovalent Zr^{4+} (0.84 Å) (ionic radii from Shannon *et al.*¹¹²). The lattice parameters gained from Rietveld refinement match the values predicted by Vegard's law.¹²¹

B.2 Radiative flux distribution

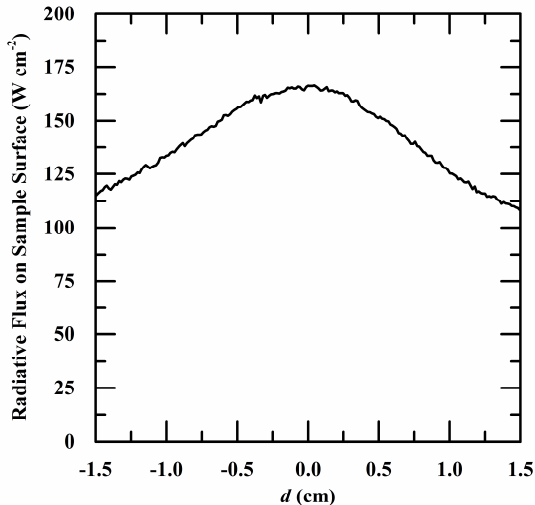


Figure B.2. Radiative flux distribution at the sample's irradiated top surface *versus* diameter of the sample.

The radiative flux distribution at the sample's irradiated top surface was measured with a CCD camera (BASLER, A 1021) focused on a water-cooled, Al_2O_3 -plasma-coated Lambertian (diffusely reflecting) target. Grey-scale calibration was performed with a water-calorimeter.

List of figures

Figure 1.1. Schematic of the two-step solar thermochemical cycle based on a generic reactive metal oxide MO. In the endothermic 1st step, the metal oxide is reduced from the oxidized state MO_{ox} to the reduced state MO_{red} by using concentrated solar energy as the process heat. In the exothermic 2nd step, the reduced metal oxide is oxidized with H₂O and/or CO₂ to its initial state and H₂ and/or CO is produced. The metal oxide is then recycled to the 1st step. 3

Figure 1.2. Equilibrium oxygen nonstoichiometry δ of ceria *versus* partial pressure of oxygen p_{O_2} for various temperatures between 1073 and 1773 K.⁶⁴ 7

Figure 1.3. $\log r$ as a function of $\log p_{O_2}$ for $T = 1073$ and 1773 K, whereas $r = p_{H_2}/p_{H_2O}$ and $r = p_{CO}/p_{CO_2}$ for a mixture of H₂/H₂O and CO/CO₂, respectively. Data is obtained from NIST-JANAF thermochemical tables. 8

Figure 1.4. Equilibrium oxygen nonstoichiometry δ of ceria⁶⁴ (circles) and 5 mol% Zr⁴⁺ doped ceria⁸⁰ (triangles) *versus* partial pressure of oxygen p_{O_2} for various temperatures. 13

Figure 2.1. (a) XRD patterns of CeO₂ and CZO_5 powder. (b) (111) reflection of CeO₂ in comparison with CZO_5..... 23

Figure 2.2. SEM images of the sintered CeO₂ pellet with (a) $\times 600$ and (b) $\times 1.2k$ magnification and of the sintered CZO_5 pellet with (c) $\times 600$ and (d) $\times 1.2k$ magnification. 24

- Figure 2.3. Schematic of the thermogravimetric analyzer (TGA) (Setaram Setsys Evolution). (a) shows an overview of the TGA whereas (b) shows a more detailed schematic of the furnace part. P and T denote pressure sensor and thermocouple, respectively. 25
- Figure 2.4. Photograph of the custom-made platinum hook suspending the dense ceria pellet to the TGA balance. 26
- Figure 2.5. (a) Mass change in wt% as a function of time for the reduction and oxidation of CeO₂ (black) and CZO_5 (blue) at $T = 1773$ K where p_{O_2} was changed between 3.0×10^{-4} bar and 2.3×10^{-4} bar (solid lines) and at $T = 1573$ K where p_{O_2} was changed between 8.2×10^{-4} bar and 2.3×10^{-4} bar (dotted lines). (b) Mass change in wt% as a function of time for the reduction and oxidation runs of CeO₂ (black) and CZO_5 (blue) at $T = 1673$ K and O₂ partial pressure range $p_{O_2} = 4.50 \times 10^{-3} - 2.3 \times 10^{-4}$ bar. (c) Mass change in wt% as a function of time for all the reduction and oxidation runs of CeO₂ and CZO_5 in the temperature range $T = 1573 - 1773$ K and O₂ partial pressure range $p_{O_2} = 4.56 \times 10^{-3} - 2.3 \times 10^{-4}$ bar. 28
- Figure 2.6. Measured δ (open symbols) of CeO₂ (a) and CZO_5 (b) for $T = 1573$ K to 1773 K and $p_{O_2} = 4.56 \times 10^{-3}$ bar to 2.3×10^{-4} bar and a comparison to literature data: Panlener *et al.*⁶⁴: closed symbols, Iwasaki *et al.*⁹²: crossed symbols. Lines indicate defect models used to describe δ 29
- Figure 2.7. Equilibrium constants *versus* inverse temperature for CeO₂ and CZO_5: (a) K_1 ; and (b) K_2 . Dashed lines indicate linear dependence of K_1 and K_2 on $1000/T$ ($R^2 > 0.99$). 33
- Figure 2.8. Partial molar enthalpy $\Delta \bar{h}_0^\circ$ of CeO₂ (open squares) and CZO_5 (open triangles) as a function of δ and a comparison to literature data of CeO₂ (Panlener *et al.*⁶⁴: closed squares, Campserveux *et al.*⁸³: diagonally crossed squares, Bevan *et al.*⁶⁵: half closed squares, Sørensen⁸²: crossed squares), CZO_5 (Kuhn *et al.*⁸⁰: closed triangles, Hao *et al.*⁴⁹: crossed triangles) and CZO_20 (Kuhn *et al.*⁸⁰: closed circles, Hao *et al.*⁴⁹: crossed circles). 36

Figure 2.9. Partial molar entropy $\Delta\bar{s}_o^\circ$ of CeO ₂ (open squares) and CZO_5 (open triangles) as a function of δ and a comparison to literature data of CeO ₂ (Panlener <i>et al.</i> ⁶⁴ : closed squares, Bevan <i>et al.</i> ⁶⁵ : half closed squares, Sørensen ⁸² : crossed squares), CZO_5 (Kuhn <i>et al.</i> ⁸⁰ : closed triangles, Hao <i>et al.</i> ⁴⁹ : crossed triangles) and CZO_20 (Kuhn <i>et al.</i> ⁸⁰ : closed circles, Hao <i>et al.</i> ⁴⁹ : crossed circles).	37
Figure 2.10. Standard partial molar Gibbs free energy $\Delta\bar{g}_o^\circ$ of CeO ₂ , CZO_5 and CZO_20 for $\delta = 0.05$, relevant for the reduction, and negative $\Delta\bar{g}_o^\circ$ for $\delta = 0.01$, relevant for the oxidation reaction. Dashed lines represent the Gibbs free energy change of the H ₂ oxidation reaction: H ₂ + 0.5O ₂ = H ₂ O ($-\Delta_r G_{H_2O}^\circ$, green) and of the CO oxidation reaction: CO + 0.5O ₂ = CO ₂ ($-\Delta_r G_{CO_2}^\circ$, orange). The metal oxide reduction reaction is at equilibrium in 1 bar p_{O_2} at $\delta = 0.05$ at the temperature where $\Delta\bar{g}_o^\circ(\delta = 0.05) = 0$. The oxidation with H ₂ O/CO ₂ to $\delta = 0.01$ is thermodynamically favorable at temperatures where $-\Delta\bar{g}_o^\circ(\delta = 0.01) = -\Delta_r G_{H_2O}^\circ$ or $-\Delta_r G_{CO_2}^\circ$, respectively	38
Figure 2.11. Molar amount of H ₂ produced by oxidation of CeO ₂ (black), CZO_5 (blue) and CZO_20 (red) with H ₂ O as a function of temperature assuming $n_{H_2O,i} = \delta_{red}$ (solid lines) and $100 \times \delta_{red}$ (dashed lines) where δ_{red} is the nonstoichiometry achieved after reduction at $T_{red} = 1773$ K and $p_{O_2} = 2.3 \times 10^{-4}$ bar ($\delta_{red} = 0.0328$ for CeO ₂ , $\delta_{red} = 0.0417$ for CZO_5, and $\delta_{red} = 0.0725$ for CZO_20).....	41
Figure 2.12. $\eta_{solar-to-fuel}$ shown as contour lines for CeO ₂ (a) and CZO_5 (b) as a function of δ_{red} and T_{ox} assuming reduction at $p_{O_2} = 10^{-6}$ bar and subsequent complete re-oxidation with steam.	44
Figure 2.13. Maximum $\eta_{solar-to-fuel}$ and T_{red} versus p_{O_2} for CeO ₂ (solid lines), CZO_5 (dashed lines) and CZO_20 (dotted lines) assuming $\delta_{red} = 0.1$ (a) and $\delta_{red} = 0.05$ (b).	45
Figure 3.1. XRD patterns of LSM40, LCM40, LSMA and LCMA powder.	52

Figure 3.2. SEM images of the pressed and sintered LSM40 (top) and LCM40 (bottom) pellet.....	53
Figure 3.3. SEM images of the pressed and sintered LSMA (top) and LCMA(bottom) pellet.....	54
Figure 3.4. Percent mass change as a function of time for all reduction and oxidation runs of LCM40, LSM40, LSMA and LCMA for: (a) temperature range $T = 1573\text{-}1773$ K and O_2 partial pressure range $p_{O_2} = 4.5066 \times 10^{-2}\text{-}2.387 \times 10^{-3}$ bar; and (b) $T = 1573\text{-}1673$ K and $p_{O_2} = 9.15 \times 10^{-4}\text{-}9.9 \times 10^{-5}$ bar.	56
Figure 3.5. Percent mass change as a function of time for all reduction and oxidation runs of LCM40 for: $T = 1573\text{-}1673$ K and O_2 partial pressure range $p_{O_2} = 9.15 \times 10^{-4}\text{-}9.9 \times 10^{-5}$ bar.....	57
Figure 3.6. Measured oxygen nonstoichiometry (symbols) of LSM40 (a) and LCM40 (b) <i>versus</i> p_{O_2} for $T = 1573$ K to 1773 K. Colored dashed and black solid lines indicate defect models used to describe experimental results. Black solid lines are calculated based on individual defect equilibrium constants whereas the colored dashed lines are calculated by using the inverse temperature dependence of $\ln K_1$ and $\ln K_2$ (<i>cf.</i> Figure 3.9 and Eq.(3.11))......	59
Figure 3.7. Measured oxygen nonstoichiometry (symbols) of LSMA (a) and LCMA (b) <i>versus</i> p_{O_2} for $T = 1573$ K to 1773 K. Colored dashed and black solid lines indicate defect models used to describe experimental results. Black solid lines are calculated based on individual defect equilibrium constants whereas the colored dashed lines are calculated by using the inverse temperature dependence of $\ln K_1$ and $\ln K_2$ (<i>cf.</i> Figure 3.9 and Eq.(3.11))......	60
Figure 3.8. Mass specific oxygen evolution for LSM40, LCM40, LSMA, LCMA and ceria <i>versus</i> temperature at $p_{O_2} = 10^{-3}$ bar.....	61

- Figure 3.9. Equilibrium constants *versus* inverse temperature for LSM40, LCM40, LSMA and LCMA: (a) K_1 ; and (b) K_2 . Lines indicate linear fits of $\ln K$ on $1000/T$ 65
- Figure 3.10. $-\ln(p_{\text{O}_2}/p^\circ)$ *versus* $1/T$ for LSM40 (a) and LCM40 (b) for the temperature range $T = 1573$ K to 1773 K and oxygen nonstoichiometry range $\delta = 0.0078$ – 0.0542 and $\delta = 0.0103$ – 0.0675 , respectively. 66
- Figure 3.11. $-\ln(p_{\text{O}_2}/p^\circ)$ *versus* $1/T$ for LSMA (a) and LCMA (b) for the temperature range $T = 1573$ K to 1773 K and oxygen nonstoichiometry range $\delta = 0.0177$ – 0.0907 and $\delta = 0.0232$ – 0.1041 , respectively. 67
- Figure 3.12. Standard partial molar enthalpy $\Delta \bar{h}_\circ^\circ$ for LSM40, LCM40, LSMA and LCMA as a function of δ . Symbols represent measured values calculated based on δ values shown by the black solid lines in Figure 3.6 and Figure 3.7 whereas dashed lines represent modeled values calculated based on δ values shown by the colored dashed lines in Figure 3.6 and Figure 3.7. 69
- Figure 3.13. Standard partial molar entropy $\Delta \bar{s}_\circ^\circ$ for LSM40, LCM40, LSMA and LCMA as a function of δ . Symbols represent measured values calculated based on δ values shown by the black solid lines in Figure 3.6 and Figure 3.7 whereas dashed lines represent modeled values calculated based on δ values shown by the colored dashed lines in Figure 3.6 and Figure 3.7. 71
- Figure 3.14. Standard partial molar Gibbs free energy $\Delta \bar{g}_\circ^\circ$ for LSM40, LCM40, LSMA, LCMA and CeO_2 for $\delta = 0.10$, relevant for the reduction, and negative $\Delta \bar{g}_\circ^\circ$ for $\delta = 0.01$, relevant for the oxidation reaction. Dashed lines represent the Gibbs free energy change of the H_2 oxidation reaction: $\text{H}_2 + 0.5\text{O}_2 = \text{H}_2\text{O}$ ($-\Delta_r G_{\text{H}_2\text{O}}^\circ$, blue) and of the CO oxidation reaction: $\text{CO} + 0.5\text{O}_2 = \text{CO}_2$ ($-\Delta_r G_{\text{CO}_2}^\circ$, red). The metal oxide reduction reaction is at equilibrium in 1 bar p_{O_2} at $\delta = 0.10$ at the temperature where $\Delta \bar{g}_\circ^\circ(\delta = 0.10) = 0$. The oxidation with $\text{H}_2\text{O}/\text{CO}_2$ to $\delta = 0.01$ is thermodynamically favorable at temperatures where $-\Delta \bar{g}_\circ^\circ(\delta = 0.01) = -\Delta_r G_{\text{H}_2\text{O}}^\circ$ or $-\Delta_r G_{\text{CO}_2}^\circ$, respectively. 72

Figure 3.15. (a) H_2 yield ($\xi_1 = \delta_{red} - \delta_{ox}$) upon oxidation of LCMA (black dashed lines), total equilibrium amount of H_2 (n_{H_2}) (red solid lines) and equilibrium amount of H_2 considering direct thermolysis only (blue dotted lines) *versus* temperature. (b) Corresponding equilibrium partial pressures of H_2 (red solid lines), of O_2 (green solid lines) upon oxidation of LCMA. In (a) and (b), squares represents results for $n_{H_2O,i} = 1$ mol, triangles for $n_{H_2O,i} = 100$ mol, circles for $n_{H_2O,i} = 1000$ mol and + symbols for $n_{H_2O,i} \rightarrow \infty$, all at $p_{tot} = 1$ bar. p_{H_2} and p_{O_2} shown by the + symbols ($n_{H_2O,i} \rightarrow \infty$) represents the minimum p_{H_2} and maximum p_{O_2} and are equal to the equilibrium partial pressures of the H_2O thermolysis reaction. 77

Figure 3.16. (a) H_2 yield ($\xi_1 = \delta_{red} - \delta_{ox}$) upon oxidation of LCMA (black dashed lines) as a function of temperature and 3 different operating pressures. Total equilibrium yields of H_2 (n_{H_2}) (red solid lines) and equilibrium amount of H_2 considering direct thermolysis only (blue dotted lines) are also shown. (b) Corresponding equilibrium partial pressures of H_2 (red solid lines), of O_2 (green solid lines) upon oxidation of LCMA. Blue and black dotted lines indicate the equilibrium partial pressure of H_2 and O_2 for thermolysis only, which is equivalent to the partial pressures when $n_{H_2O,i} \rightarrow \infty$. In (a) and (b), squares represents results for $p_{tot} = 100$ bar, triangles for $p_{tot} = 1$ bar and circles for $p_{tot} = 0.01$ bar, all for $n_{H_2O,i} = 100$ mol. 79

Figure 3.17. (a) Calculated H_2 yield upon oxidation of LCMA, LSMA, LCM40, LSM40 and CeO_2 *versus* temperature for $n_{H_2O,i} = 1$ mol (squares) and $n_{H_2O,i} = 1000$ mol (circles) at $p_{tot} = 1$ bar. (b) Calculated H_2 yield upon oxidation of LCMA, LSMA, LCM40, LSM40 and CeO_2 *versus* $n_{H_2O,i}$ for $T = 1200$ K at $p_{tot} = 1$ bar. In (a) and (b), the oxygen nonstoichiometry before oxidation (δ_{red}) is shown by the solid lines and was determined for $T_{red} = 1673$ K and $p_{O_2} = 10^{-4}$ bar for all materials and additionally for $T_{red} = 1873$ K and $p_{O_2} = 10^{-4}$ bar for CeO_2 (open symbols). H_2 yields close to their

maximum are not shown because partial molar thermodynamic data was only calculated for $\delta \geq 0.001$	81
Figure 3.18. $\Delta \bar{g}_o^\circ$ for all the materials investigated for $\delta = 0.10$, relevant for the reduction, and negative $\Delta \bar{g}_o^\circ$ for $\delta = 0.01$, relevant for the oxidation reaction. Dashed lines represent the Gibbs free energy change of (a): the H_2 oxidation reaction: $(-\Delta_r G_{H_2O}^\circ)$ and of (b): the CO oxidation reaction: $(-\Delta_r G_{CO_2}^\circ)$ for varying equilibrium fuel ratios. The metal oxide reduction reaction is at equilibrium at $\delta = 0.10$ at T where $\Delta \bar{g}_o^\circ(\delta = 0.10)$ crosses the corresponding p_{O_2} line (solid line). The oxidation with H_2O/CO_2 to $\delta = 0.01$ is thermodynamically favorable at T where $-\Delta \bar{g}_o^\circ(\delta = 0.01)$ crosses the corresponding line of $-\Delta_r G_{H_2O}^\circ$ or $-\Delta_r G_{CO_2}^\circ$, respectively.....	85
Figure 4.1. Photographs of ceria DS-RPC structures with 8, 10 and 35 ppi in the mm-scale and 18% porosity within the struts in the μm -scale. Also shown is the ceria fiber sample with 88% porosity in the μm -scale.....	89
Figure 4.2. Schematic of the solar-driven thermogravimetric analyzer. Concentrated radiation delivered by the High-Flux Solar Simulator (HFSS) is redirected by a 45° -tilted mirror, enters the setup through a transparent quartz dome, and is incident on the RPC sample whose weight change and gas evolution are temporally monitored.....	91
Figure 4.3. Solar-TG measurements for the 10 ppi ceria DS-RPC: (a) temperature as a function of time at $z = 2$ mm (dotted lines), 7 mm (dashed lines), and 12 mm (solid lines) below the top surface during 3 consecutive redox cycles; (b) corresponding %-mass change; and (c) corresponding mass specific O_2 and CO evolution rates as well as the integrated mass specific O_2 and CO evolved.....	94
Figure 4.4. Solar-TG measurements of the 8 ppi, 10 ppi and 35 ppi ceria DS-RPC and the ceria fiber sample: (a) bottom temperature as a function of time during reduction; (b) specific weight change during reduction.	96
Figure 4.5. Percent weight change of the 8 ppi, 10 ppi and 35 ppi ceria DS-RPC during oxidation with CO_2	97

Figure 4.6. Temperatures along the centerline of the 10 ppi and 35 ppi ceria DS-RPC and the ceria fiber sample <i>versus</i> distance z below the top surface, measured at the end of the reduction step of the 2 nd cycle for a radiative mean flux of 1280 suns.	98
Figure 4.7. SEM images of the 10 ppi ceria DS-RPC (1 st row) and of the ceria fiber sample (2 nd row): (a) locations where the SEM images were taken; (b,f) before redox cycling; (c,g) after redox cycling at the edge of the bottom surface; (d,h) after redox cycling at the edge of the top surface; and (e,i) after redox cycling at the center of the irradiated top surface.	100
Figure 4.8. (a) Volume-specific flow rate of O ₂ and CO as well as the bottom temperature of the RPC with single-scale porosity (SS-RPC) (dashed lines) and of the RPC with dual-scale porosity (DS-RPC) (solid lines) during the second redox cycle. Additionally, integrated mass specific O ₂ release and CO yield are shown in (a). (b) Mass-specific and (c) volume-specific CO yield of both RPCs during the second oxidation.	102
Figure 4.9. (a) Percent mass change and bottom temperature of the CeO ₂ , CZO_10 and CZO_20 DS-RPC sample with 10 ppi during the three redox cycles. Mass specific O ₂ release (b) and CO productivity (c) during reduction steps 1, 2 and 3 <i>versus</i> Zr ⁴⁺ -dopant concentration x	105
Figure 5.1. Schematic of the infrared furnace setup. The RPC sample is placed in the quartz tube located inside the IR furnace. Temperature is controlled and measured with two type-B thermocouples (TC). Sweep and oxidant gases are delivered with electronic mass flow controllers. Excess steam is condensed in a glass condenser and product gases are cooled in a gas cooler. The product gas composition is analyzed with a mass spectrometer. The overpressure inside the quartz tube, maintained by the check valve, is monitored with a pressure sensor (P) located at the product gas exit of the furnace.	109

- Figure 5.2. Photographs of the infrared furnace setup. Top: Open furnace with view on the ceria RPC sample and the thermocouples. Bottom: Infrared furnace in operation. 110
- Figure 5.3. Typical specific O₂ evolution and H₂ production of the DS-RPC with the small pores (0.4 – 12 μm pore former size) as well as controlling temperature (solid line) and measured reference temperature (dashed line) of the RPC during 2 redox cycles between minute 110 and 140. 113
- Figure 5.4. H₂ flow rate at $\delta = 0.01, 0.0075, \text{ and } 0.005$ of the DS-RPC with large pores *versus* oxidation temperature. δ before oxidation was approximately $\delta = 0.016$, obtained after reduction at $T_{\text{red,set}} = 1673 \text{ K}$ 114
- Figure 5.5. (a) O₂ yield (symbols) of the DS-RPC with large pores in the μm-range (10 – 20 μm pore former size) *versus* cycle number as well as the maximum mean reduction temperature \bar{T}_{red} during each cycle (lines). (b) H₂ yield (symbols) and minimum mean oxidation temperature \bar{T}_{ox} (lines) *versus* cycle number. In (a) and (b), open symbols and solid lines correspond to the cycles with set reduction temperature $T_{\text{red,set}} = 1773 \text{ K}$, whereas closed symbols and dashed lines correspond to the cycles at $T_{\text{red,set}} = 1673 \text{ K}$. (c) Corresponding H₂ flow rate at $\delta = 0.01$ for $T_{\text{red,set}} = 1673 \text{ K}$ (open circles) and $\delta = 0.02$ for $T_{\text{red,set}} = 1773 \text{ K}$ (×-symbols)..... 116
- Figure 5.6. (a) O₂ yield (symbols) of the DS-RPC with small pores in the μm-range (0.4 – 12 μm pore former size) *versus* cycle number as well as the maximum mean reduction temperature \bar{T}_{red} during each cycle (lines). (b) H₂ yield (symbols) and minimum mean oxidation temperature \bar{T}_{ox} (lines) *versus* cycle number. In (a) and (b), open symbols and solid lines correspond to the cycles with set reduction temperature $T_{\text{red,set}} = 1773 \text{ K}$, whereas closed symbols and dashed lines correspond to the cycles at $T_{\text{red,set}} = 1673 \text{ K}$. (c) Corresponding H₂ flow rate at $\delta = 0.01$ for $T_{\text{red,set}} = 1673 \text{ K}$ (open circles) and $\delta = 0.02$ for $T_{\text{red,set}} = 1773 \text{ K}$ (×-symbols)..... 117
- Figure 5.7. SEM images of DS-RPCs with small pores in the μm-range (0.4 – 12 μm pore former size): (a) before redox cycling; (b) after 1 reduction;

(c) after reduction of the 2 nd cycle; (d) after 25 cycles at $T_{\text{red,set}} = 1773 \text{ K}$; (e) after 100 cycles at $T_{\text{red,set}} = 1773 \text{ K}$ ($\delta \approx 0.026$); and (f) after 100 cycles at $T_{\text{red,set}} = 1673 \text{ K}$ ($\delta \approx 0.017$).....	119
Figure 5.8. SEM of DS-RPCs with small pores in the μm -range (0.4 – 12 μm pore former size): (a) heated in air with 600 K min^{-1} to $T_{\text{red,set}} = 1773 \text{ K}$; (b) heated in air with 600 K min^{-1} to $T_{\text{red,set}} = 1773 \text{ K}$, then isothermally reduced by switching from air to Ar; (c) reduced in Ar by heating with 50 K min^{-1} to $T_{\text{red,set}} = 1773 \text{ K}$	121
Figure 5.9. H_2 flow rate at $\delta = 0.02$ for the DS-RPC with small pores (0.4 – 12 μm pore former size) <i>versus</i> cycle number. In cycle 1 – 20 the RPC was heated with 40 K min^{-1} to $T_{\text{red,set}} = 1773 \text{ K}$ whereas in cycle 21 – 45, the heating rate was 600 K min^{-1}	122
Figure 5.10. H_2 flow rate of the single-scale RPC at $\delta = 0.025$ <i>versus</i> cycle number for $T_{\text{red,set}} = 1773 \text{ K}$ with 600 K min^{-1} heating rate.	123
Figure 5.11. SEM images of SS-RPCs: (a) before redox cycling; (b) after 1 reduction; and (c) after 75 cycles at $T_{\text{red,set}} = 1773 \text{ K}$	124
Figure 5.12. (a) O_2 and H_2 yield of the DS-RPC with small pores in the μm -range (0.4 – 12 μm pore former size) <i>versus</i> cycle number. (b) H_2 flow rate at $\delta = 0.031$ <i>versus</i> cycle number.....	126
Figure 5.13. SEM image of DS-RPC with small pores in the μm -range (0.4 – 12 μm pore former size) after 500 redox cycles at $T_{\text{red,set}} = 1773 \text{ K}$ ($\delta > 0.035$)......	127
Figure A.1. Graphical representation of Eq. (A.15). X of LCM40 at $T = 1673 \text{ K}$ is shown <i>versus</i> Y . The slope of the linear regression is equal to K_2 whereas the Y -intercept is equal to $-K_1^{1/2}$	139
Figure B.1. (a) XRD patterns of $\text{Zr}_x\text{Ce}_{1-x}\text{O}_2$ ($x = 0, 0.1, 0.2$) solid solutions after sintering at 1873 K and (b) zoom into the (111) and (200) reflections. Reflections are shifted towards higher angles for increasing Zr^{4+} -dopant concentration. Lattice parameters gained from Rietveld refinement are	

shown in (b). Vertical lines represent reflection positions of CeO ₂ reference pattern (ICSD-Database).....	141
Figure B.2. Radiative flux distribution at the sample's irradiated top surface <i>versus</i> diameter of the sample.....	142

List of tables

Table 3.1. Metal nitrates used for sample preparation.	50
Table 3.2. ICP-OES analysis of $\text{La}_{0.6}\text{Sr}_{0.4}\text{Mn}_{0.6}\text{Al}_{0.4}\text{O}_3$ (LSMA) and $\text{La}_{0.6}\text{Ca}_{0.4}\text{Mn}_{0.6}\text{Al}_{0.4}\text{O}_3$ (LCMA) shown in mole fraction.....	51
Table 3.3. Linear fitting parameters of $\ln K_i$ versus $1000/T$ (<i>cf.</i> Eq.(3.11)) of all four perovskites represented by the enthalpy Δh_i° and entropy Δs_i° of the two single defect reactions.	64
Table 4.1. Mass and density of the porous ceria samples.	95

Bibliography

- [1] IEA. World Energy Outlook 2015, OECD Publishing.
- [2] D. Mignard, C. Pritchard. Processes for the Synthesis of Liquid Fuels from CO₂ and Marine Energy, *Chemical Engineering Research and Design* 84 (2006) 828-836.
- [3] M.E. Dry. The Fischer–Tropsch process: 1950–2000, *Catalysis Today* 71 (2002) 227-241.
- [4] G.P. Smestad, A. Steinfeld. Review: Photochemical and Thermochemical Production of Solar Fuels from H₂O and CO₂ Using Metal Oxide Catalysts, *Industrial & Engineering Chemistry Research* 51 (2012) 11828-11840.
- [5] C. Graves, S.D. Ebbesen, M. Mogensen, K.S. Lackner. Sustainable hydrocarbon fuels by recycling CO₂ and H₂O with renewable or nuclear energy, *Renewable and Sustainable Energy Reviews* 15 (2011) 1-23.
- [6] J.A. Villoria, R.M. Navarro Yerga, S.M. Al-Zahrani, J.L.G. Fierro. Photocatalytic Hydrogen Production on Cd_{1-x}Zn_xS Solid Solutions under Visible Light: Influence of Thermal Treatment, *Industrial & Engineering Chemistry Research* 49 (2010) 6854-6861.
- [7] H. Kazuhito, I. Hiroshi, F. Akira. TiO₂ Photocatalysis: A Historical Overview and Future Prospects, *Japanese Journal of Applied Physics* 44 (2005) 8269.
- [8] J.-M. Lehn, R. Ziesel. Photochemical generation of carbon monoxide and hydrogen by reduction of carbon dioxide and water under visible light irradiation, *Proceedings of the National Academy of Sciences* 79 (1982) 701-704.
- [9] C. Bailleux, A. Damien, A. Montet. Alkaline electrolysis of water-EGF activity in electrochemical engineering from 1975 to 1982, *International Journal of Hydrogen Energy* 8 (1983) 529-538.
- [10] I. Abe, T. Fujimaki, M. Matsubara. Hydrogen production by high temperature, high pressure water electrolysis, results of test plant operation, *International Journal of Hydrogen Energy* 9 (1984) 753-758.
- [11] A. Steinfeld, R. Palumbo. Solar Thermochemical Process Technology. *Encyclopedia of Physical Science and Technology*, vol. 15, 2001. p.237-256.

- [12] A. Steinfeld. Solar thermochemical production of hydrogen - a review, *Solar Energy* 78 (2005) 603 - 615.
- [13] S.Z. Baykara. Experimental solar water thermolysis, *International Journal of Hydrogen Energy* 29 (2004) 1459-1469.
- [14] J. Lédé, F. Lapicque, J. Villiermaux. Production of hydrogen by direct thermal decomposition of water, *International Journal of Hydrogen Energy* 8 (1983) 675-679.
- [15] A. Kogan. Direct solar thermal splitting of water and on-site separation of the products I. Theoretical evaluation of Hydrogen yield, *Int. J. Hydrogen Energy* 22 (1997) 481 - 486.
- [16] J.A. Wurzbacher, C. Gebald, A. Steinfeld. Separation of CO₂ from air by temperature-vacuum swing adsorption using diamine-functionalized silica gel, *Energy & Environmental Science* 4 (2011) 3584-3592.
- [17] C. Gebald, J.A. Wurzbacher, P. Tingaut, T. Zimmermann, A. Steinfeld. Amine-Based Nanofibrillated Cellulose As Adsorbent for CO₂ Capture from Air, *Environmental Science & Technology* 45 (2011) 9101-9108.
- [18] S. Choi, M.L. Gray, C.W. Jones. Amine-Tethered Solid Adsorbents Coupling High Adsorption Capacity and Regenerability for CO₂ Capture From Ambient Air, *ChemSusChem* 4 (2011) 628-635.
- [19] K.S. Lackner. Capture of carbon dioxide from ambient air, *The European Physical Journal Special Topics* 176 (2009) 93-106.
- [20] V. Nikulshina, C. Gebald, A. Steinfeld. CO₂ capture from atmospheric air via consecutive CaO-carbonation and CaCO₃-calcination cycles in a fluidized-bed solar reactor, *Chemical Engineering Journal* 146 (2009) 244-248.
- [21] J.E. Miller, M.D. Allendorf, R.B. Diver, L.R. Evans, N.P. Siegel, J.N. Stuecker. Metal oxide composites and structures for ultra-high temperature solar thermochemical cycles, *Journal of Materials Science* 43 (2008) 4714-4728.
- [22] J.E. Miller, A.H. McDaniel, M.D. Allendorf. Considerations in the Design of Materials for Solar-Driven Fuel Production Using Metal-Oxide Thermochemical Cycles, *Advanced Energy Materials* 4 (2014) n/a-n/a.
- [23] J.R. Scheffe, A. Steinfeld. Oxygen exchange materials for solar thermochemical splitting of H₂O and CO₂: a review, *Materials Today* 17 (2014) 341-348.
- [24] M. Romero, A. Steinfeld. Concentrating solar thermal power and thermochemical fuels, *Energy & Environmental Science* 5 (2012) 9234-9245.
- [25] T. Nakamura. Hydrogen production from water utilizing solar heat at high temperatures, *Solar Energy* 19 (1977) 467-475.
- [26] E.N. Coker, A. Ambrosini, M.A. Rodriguez, J.E. Miller. Ferrite-YSZ composites for solar thermochemical production of synthetic fuels: in operando characterization of CO₂ reduction, *Journal of Materials Chemistry* 21 (2011) 10767-10776.

- [27] P. Charvin, S. Abanades, G. Flamant, F. Lemort. Two-step water splitting thermochemical cycle based on iron oxide redox pair for solar hydrogen production, *Energy* 32 (2007) 1124 - 1133.
- [28] T. Kodama, Y. Nakamuro, T. Mizuno. A Two-Step Thermochemical Water Splitting by Iron-Oxide on Stabilized Zirconia, *J. Solar Energy Eng.* 128 (2006) 3 - 7.
- [29] N. Gokon, H. Murayama, J. Umeda, T. Hatamachi, T. Kodama. Monoclinic zirconia-supported Fe₃O₄ for the two-step water-splitting thermochemical cycle at high thermal reduction temperatures of 1400–1600 °C, *International Journal of Hydrogen Energy* 34 (2009) 1208-1217.
- [30] T. Kodama, Y. Kondoh, R. Yamamoto, H. Andou, N. Satou. Thermochemical hydrogen production by a redox system of ZrO₂-supported Co(II)-ferrite, *Solar Energy* 78 (2005) 623 - 631.
- [31] J.R. Scheffe, A.H. McDaniel, M.D. Allendorf, A.W. Weimer. Kinetics and mechanism of solar-thermochemical H₂ production by oxidation of a cobalt ferrite-zirconia composite, *Energy & Environmental Science* 6 (2013) 963-973.
- [32] M.D. Allendorf, R.B. Diver, N.P. Siegel, J.E. Miller. Two-Step Water Splitting Using Mixed-Metal Ferrites: Thermodynamic Analysis and Characterization of Synthesized Materials, *Energy & Fuels* 22 (2008) 4115-4124.
- [33] A. Steinfeld. Solar hydrogen production via a two-step water splitting thermochemical cycle based on Zn/ZnO redox reactions, *Int. J. Hydrogen Energy* 27 (2002) 611 - 619.
- [34] C. Perkins, P.R. Lichty, A.W. Weimer. Thermal ZnO dissociation in a rapid aerosol reactor as part of a solar hydrogen production cycle, *International Journal of Hydrogen Energy* 33 (2008) 499-510.
- [35] P.G. Loutzenhiser, A. Meier, A. Steinfeld. Review of the Two-Step H₂O/CO₂-Splitting Solar Thermochemical Cycle Based on Zn/ZnO Redox Reactions, *Materials* 3 (2010) 4922-4938.
- [36] W. Villasmil, M. Brkic, D. Wuillemin, A. Meier, A. Steinfeld. Pilot Scale Demonstration of a 100-kW_{th} Solar Thermochemical Plant for the Thermal Dissociation of ZnO, *Journal of Solar Energy Engineering* 136 (2013) 011016-011016.
- [37] D. Weibel, Z.R. Jovanovic, E. Gálvez, A. Steinfeld. Mechanism of Zn Particle Oxidation by H₂O and CO₂ in the Presence of ZnO, *Chemistry of Materials* 26 (2014) 6486-6495.
- [38] W.C. Chueh, S.M. Haile. A thermochemical study of ceria: exploiting an old material for new modes of energy conversion and CO₂ mitigation, *Philosophical Transactions of the Royal Society A: Mathematical, Physical and Engineering Sciences* 368 (2010) 3269-3294.

- [39] W.C. Chueh, C. Falter, M. Abbott, D. Scipio, P. Furler, S.M. Haile, A. Steinfeld. High-Flux Solar-Driven Thermochemical Dissociation of CO₂ and H₂O Using Nonstoichiometric Ceria, *Science* 330 (2010) 1797-1801.
- [40] P. Furler, J. Scheffe, M. Gorbar, L. Moes, U. Vogt, A. Steinfeld. Solar Thermochemical CO₂ Splitting Utilizing a Reticulated Porous Ceria Redox System, *Energy & Fuels* 26 (2012) 7051-7059.
- [41] Y. Hao, C.-K. Yang, S.M. Haile. High-temperature isothermal chemical cycling for solar-driven fuel production, *Physical Chemistry Chemical Physics* 15 (2013) 17084-17092.
- [42] D. Marxer, P. Furler, J. Scheffe, H. Geerlings, C. Falter, V. Batteiger, A. Sizmann, A. Steinfeld. Demonstration of the Entire Production Chain to Renewable Kerosene via Solar Thermochemical Splitting of H₂O and CO₂, *Energy & Fuels* 29 (2015) 3241-3250.
- [43] J.R. Scheffe, M. Welte, A. Steinfeld. Thermal Reduction of Ceria within an Aerosol Reactor for H₂O and CO₂ Splitting, *Industrial & Engineering Chemistry Research* 53 (2014) 2175-2182.
- [44] S. Abanades, A. Legal, A. Cordier, G. Peraudeau, G. Flamant, A. Julbe. Investigation of reactive cerium-based oxides for H₂ production by thermochemical two-step water-splitting, *Journal of Materials Science* 45 (2010) 4163-4173.
- [45] A. Le Gal, S. Abanades, N. Bion, T. Le Mercier, V. Harlé. Reactivity of Doped Ceria-Based Mixed Oxides for Solar Thermochemical Hydrogen Generation via Two-Step Water-Splitting Cycles, *Energy & Fuels* 27 (2013) 6068-6078.
- [46] Q.-L. Meng, C.-i. Lee, T. Ishihara, H. Kaneko, Y. Tamaura. Reactivity of CeO₂-based ceramics for solar hydrogen production via a two-step water-splitting cycle with concentrated solar energy, *International Journal of Hydrogen Energy* 36 (2011) 13435-13441.
- [47] J.R. Scheffe, R. Jacot, G.R. Patzke, A. Steinfeld. Synthesis, Characterization, and Thermochemical Redox Performance of Hf⁴⁺, Zr⁴⁺, and Sc³⁺ Doped Ceria for Splitting CO₂, *The Journal of Physical Chemistry C* 117 (2013) 24104-24114.
- [48] F. Call, M. Roeb, M. Schmücker, H. Bru, D. Curulla-Ferre, C. Sattler, R. Pitz-Paal. Thermogravimetric Analysis of Zirconia-Doped Ceria for Thermochemical Production of Solar Fuel, *American Journal of Analytical Chemistry* 4 (2013) 37.
- [49] Y. Hao, C.-K. Yang, S.M. Haile. Ceria–Zirconia Solid Solutions (Ce_{1-x}Zr_xO_{2-δ}, x ≤ 0.2) for Solar Thermochemical Water Splitting: A Thermodynamic Study, *Chemistry of Materials* 26 (2014) 6073-6082.
- [50] J.R. Scheffe, D. Weibel, A. Steinfeld. Lanthanum–Strontium–Manganese Perovskites as Redox Materials for Solar Thermochemical Splitting of H₂O and CO₂, *Energy & Fuels* 27 (2013) 4250-4257.

- [51] A.H. McDaniel, E.C. Miller, D. Arifin, A. Ambrosini, E.N. Coker, R. O'Hayre, W.C. Chueh, J. Tong. Sr-and Mn-doped $\text{LaAlO}_{3-\delta}$ for solar thermochemical H_2 and CO production, *Energy & Environmental Science* 6 (2013) 2424-2428.
- [52] C.-K. Yang, Y. Yamazaki, A. Aydin, S.M. Haile. Thermodynamic and kinetic assessments of strontium-doped lanthanum manganite perovskites for two-step thermochemical water splitting, *Journal of Materials Chemistry A* 2 (2014) 13612-13623.
- [53] S. Dey, B.S. Naidu, A. Govindaraj, C.N.R. Rao. Noteworthy performance of $\text{La}_{1-x}\text{Ca}_x\text{MnO}_3$ perovskites in generating H_2 and CO by the thermochemical splitting of H_2O and CO_2 , *Physical Chemistry Chemical Physics* 17 (2015) 122-125.
- [54] S. Dey, B.S. Naidu, C.N.R. Rao. $\text{Ln}_{0.5}\text{A}_{0.5}\text{MnO}_3$ (Ln=Lanthanide, A= Ca, Sr) Perovskites Exhibiting Remarkable Performance in the Thermochemical Generation of CO and H_2 from CO_2 and H_2O , *Chemistry – A European Journal* 21 (2015) 7077-7081.
- [55] A. Demont, S. Abanades, E. Beche. Investigation of Perovskite Structures as Oxygen-Exchange Redox Materials for Hydrogen Production from Thermochemical Two-Step Water-Splitting Cycles, *The Journal of Physical Chemistry C* 118 (2014) 12682-12692.
- [56] A.H. Bork, M. Kubicek, M. Struzik, J.L.M. Rupp. Perovskite $\text{La}_{0.6}\text{Sr}_{0.4}\text{Cr}_{1-x}\text{Co}_x\text{O}_{3-\delta}$ solid solutions for solar-thermochemical fuel production: strategies to lower the operation temperature, *Journal of Materials Chemistry A* 3 (2015) 15546-15557.
- [57] T. Cooper, J.R. Scheffe, M.E. Galvez, R. Jacot, G. Patzke, A. Steinfeld. Lanthanum Manganite Perovskites with Ca/Sr A-site and Al B-site Doping as Effective Oxygen Exchange Materials for Solar Thermochemical Fuel Production, *Energy Technology* 3 (2015) 1130-1142.
- [58] M.E. Galvez, R. Jacot, J. Scheffe, T. Cooper, G. Patzke, A. Steinfeld. Physico-chemical changes in Ca, Sr and Al-doped La-Mn-O perovskites upon thermochemical splitting of CO_2 via redox cycling, *Physical Chemistry Chemical Physics* 17 (2015) 6629-6634.
- [59] S. Ackermann, L. Sauvin, R. Castiglioni, J.L.M. Rupp, J.R. Scheffe, A. Steinfeld. Kinetics of CO_2 Reduction over Nonstoichiometric Ceria, *The Journal of Physical Chemistry C* 119 (2015) 16452-16461.
- [60] S. Ackermann, J.R. Scheffe, A. Steinfeld. Diffusion of Oxygen in Ceria at Elevated Temperatures and Its Application to $\text{H}_2\text{O}/\text{CO}_2$ Splitting Thermochemical Redox Cycles, *The Journal of Physical Chemistry C* (2014).
- [61] N. Knoblauch, L. Dorrer, P. Fielitz, M. Schmucker, G. Borchardt. Surface controlled reduction kinetics of nominally undoped polycrystalline CeO_2 , *Physical Chemistry Chemical Physics* 17 (2015) 5849-5860.

- [62] M. Takacs, J.R. Scheffe, A. Steinfeld. Oxygen nonstoichiometry and thermodynamic characterization of Zr doped ceria in the 1573-1773 K temperature range, *Physical Chemistry Chemical Physics* 17 (2015) 7813-7822.
- [63] J.R. Scheffe, A. Steinfeld. Thermodynamic Analysis of Cerium-Based Oxides for Solar Thermochemical Fuel Production, *Energy & Fuels* 26 (2012) 1928-1936.
- [64] R.J. Panlener, R.N. Blumenthal, J.E. Garnier. A thermodynamic study of nonstoichiometric cerium dioxide, *Journal of Physics and Chemistry of Solids* 36 (1975) 1213-1222.
- [65] D.J.M. Bevan, J. Kordis. Mixed oxides of the type MO_2 (fluorite)- M_2O_3 -I Oxygen dissociation pressures and phase relationships in the system CeO_2 - Ce_2O_3 at high temperatures, *Journal of Inorganic and Nuclear Chemistry* 26 (1964) 1509-1523.
- [66] S. Abanades, G. Flamant. Thermochemical hydrogen production from a two-step solar-driven water-splitting cycle based on cerium oxides, *Solar Energy* 80 (2006) 1611-1623.
- [67] P. Furler, J. Scheffe, D. Marxer, M. Gorbar, A. Bonk, U. Vogt, A. Steinfeld. Thermochemical CO_2 splitting via redox cycling of ceria reticulated foam structures with dual-scale porosities, *Physical Chemistry Chemical Physics* 16 (2014) 10503-10511.
- [68] L.J. Venstrom, N. Petkovich, S. Rudisill, A. Stein, J.H. Davidson. The Effects of Morphology on the Oxidation of Ceria by Water and Carbon Dioxide, *Journal of Solar Energy Engineering* 134 (2012) 011005-011001-011008.
- [69] W.T. Gibbons, L.J. Venstrom, R.M. De Smith, J.H. Davidson, G.S. Jackson. Ceria-based electrospun fibers for renewable fuel production via two-step thermal redox cycles for carbon dioxide splitting, *Physical Chemistry Chemical Physics* 16 (2014) 14271-14280.
- [70] P. Furler, J.R. Scheffe, A. Steinfeld. Syngas production by simultaneous splitting of H_2O and CO_2 via ceria redox reactions in a high-temperature solar reactor, *Energy & Environmental Science* 5 (2012) 6098-6103.
- [71] S. Haussener, P. Coray, W. Lipiński, P. Wyss, A. Steinfeld. Tomography-Based Heat and Mass Transfer Characterization of Reticulate Porous Ceramics for High-Temperature Processing, *Journal of Heat Transfer* 132 (2009) 023305-023305.
- [72] N.R. Rhodes, M.M. Bobek, K.M. Allen, D.W. Hahn. Investigation of long term reactive stability of ceria for use in solar thermochemical cycles, *Energy* 89 (2015) 924-931.
- [73] R.B. Diver, J.E. Miller, N.P. Siegel, T.A. Moss. Testing of a CR5 solar thermochemical heat engine prototype. ASME 2010 4th International Conference on Energy Sustainability: American Society of Mechanical Engineers, 2010. p.97-104.

- [74] I. Ermanoski, N.P. Siegel, E.B. Stechel. A New Reactor Concept for Efficient Solar-Thermochemical Fuel Production, *Journal of Solar Energy Engineering* 135 (2013) 031002-031001 - 031002-031010.
- [75] R. Bader, L.J. Venstrom, J.H. Davidson, W. Lipiński. Thermodynamic Analysis of Isothermal Redox Cycling of Ceria for Solar Fuel Production, *Energy & Fuels* 27 (2013) 5533-5544.
- [76] L.J. Venstrom, R.M. De Smith, Y. Hao, S.M. Haile, J.H. Davidson. Efficient Splitting of CO₂ in an Isothermal Redox Cycle Based on Ceria, *Energy & Fuels* 28 (2014) 2732-2742.
- [77] I. Ermanoski, J.E. Miller, M.D. Allendorf. Efficiency maximization in solar-thermochemical fuel production: challenging the concept of isothermal water splitting, *Physical Chemistry Chemical Physics* 16 (2014) 8418-8427.
- [78] J. Lapp, J.H. Davidson, W. Lipiński. Efficiency of two-step solar thermochemical non-stoichiometric redox cycles with heat recovery, *Energy* 37 (2012) 591-600.
- [79] J. Kim, T.A. Johnson, J.E. Miller, E.B. Stechel, C.T. Maravelias. Fuel production from CO₂ using solar-thermal energy: system level analysis, *Energy & Environmental Science* 5 (2012) 8417-8429.
- [80] M. Kuhn, S.R. Bishop, J.L.M. Rupp, H.L. Tuller. Structural characterization and oxygen nonstoichiometry of ceria-zirconia (Ce_{1-x}Zr_xO_{2-δ}) solid solutions, *Acta Materialia* 61 (2013) 4277-4288.
- [81] P.R. Shah, T. Kim, G. Zhou, P. Fornasiero, R.J. Gorte. Evidence for Entropy Effects in the Reduction of Ceria-Zirconia Solutions, *Chemistry of Materials* 18 (2006) 5363-5369.
- [82] O.T. Sørensen. Thermodynamic studies of the phase relationships of nonstoichiometric cerium oxides at higher temperatures, *Journal of Solid State Chemistry* 18 (1976) 217-233.
- [83] J. Campserveux, P. Gerdanian. High-temperature microcalorimetric measurements of the partial molar enthalpy of solution of O₂ in cerium oxides: CeO_{1.5} to CeO₂, *The Journal of Chemical Thermodynamics* 6 (1974) 795-800.
- [84] J. Mizusaki, N. Mori, H. Takai, Y. Yonemura, H. Minamiue, H. Tagawa, M. Dokiya, H. Inaba, K. Naraya, T. Sasamoto, T. Hashimoto. Oxygen nonstoichiometry and defect equilibrium in the perovskite-type oxides La_{1-x}Sr_xMnO_{3+δ}, *Solid State Ionics* 129 (2000) 163-177.
- [85] T. Cooper, J.R. Scheffe, M.E. Galvez, R. Jacot, G. Patzke, A. Steinfeld. Lanthanum Manganite Perovskites with Ca/Sr A-site and Al B-site Doping as Effective Oxygen Exchange Materials for Solar Thermochemical Fuel Production, *Energy Technology* (2015).
- [86] J. Kašpar, P. Fornasiero, N. Hickey. Automotive catalytic converters: current status and some perspectives, *Catalysis Today* 77 (2003) 419-449.

- [87] M. Sugiura, M. Ozawa, A. Suda, T. Suzuki, T. Kanazawa. Development of Innovative Three-Way Catalysts Containing Ceria-Zirconia Solid Solutions with High Oxygen Storage/Release Capacity, *Bulletin of the Chemical Society of Japan* 78 (2005) 752-767.
- [88] T. Kobayashi, S. Wang, M. Dokiya, H. Tagawa, T. Hashimoto. Oxygen nonstoichiometry of $Ce_{1-y}Sm_yO_{2-0.5y-x}$ ($y=0.1, 0.2$), *Solid State Ionics* 126 (1999) 349-357.
- [89] M. Katsuki, S. Wang, K. Yasumoto, M. Dokiya. The oxygen transport in Gd-doped ceria, *Solid State Ionics* 154-155 (2002) 589-595.
- [90] L.O. Schunk, A. Steinfeld. Kinetics of the thermal dissociation of ZnO exposed to concentrated solar irradiation using a solar-driven thermogravimeter in the 1800-2100 K range, *AIChE Journal* 55 (2009) 1497-1504.
- [91] G. Levêque, S. Abanades. Design and operation of a solar-driven thermogravimeter for high temperature kinetic analysis of solid-gas thermochemical reactions in controlled atmosphere, *Solar Energy* 105 (2014) 225-235.
- [92] B. Iwasaki, T. Katsura. The Thermodynamic Properties of the Nonstoichiometric Ceric Oxide at Temperatures from 900 to 1300°C, *Bulletin of the Chemical Society of Japan* 44 (1971) 1297-1301.
- [93] T. Otake, H. Yugami, K. Yashiro, Y. Nigara, T. Kawada, J. Mizusaki. Nonstoichiometry of $Ce_{1-x}Y_xO_{2-0.5x-\delta}$ ($X=0.1, 0.2$), *Solid State Ionics* 161 (2003) 181-186.
- [94] S.R. Bishop, K.L. Duncan, E.D. Wachsman. Defect equilibria and chemical expansion in non-stoichiometric undoped and gadolinium-doped cerium oxide, *Electrochimica Acta* 54 (2009) 1436-1443.
- [95] M. Mogensen, N.M. Sammes, G.A. Tompsett. Physical, chemical and electrochemical properties of pure and doped ceria, *Solid State Ionics* 129 (2000) 63-94.
- [96] L.J. Gauckler, M. Gödickemeier, D. Schneider. Nonstoichiometry and Defect Chemistry of Ceria Solid Solutions, *Journal of Electroceramics* 1 (1997) 165-172.
- [97] S. Wang, H. Inaba, H. Tagawa, T. Hashimoto. Nonstoichiometry of $Ce_{0.8}Gd_{0.2}O_{1.9-x}$, *Journal of The Electrochemical Society* 144 (1997) 4076-4080.
- [98] S. Wang, H. Inaba, H. Tagawa, M. Dokiya, T. Hashimoto. Nonstoichiometry of $Ce_{0.9}Gd_{0.1}O_{1.95-x}$, *Solid state ionics (Print)* 107 (1998) 73-79.
- [99] Z. Yang, T.K. Woo, K. Hermansson. Effects of Zr doping on stoichiometric and reduced ceria: A first-principles study, *The Journal of Chemical Physics* 124 (2006) 224704.
- [100] Y.S. Touloukian. Thermophysical Properties of High Temperature Solid Materials. Volume 4. Oxides and Their Solutions and Mixtures. Part I. Simple Oxygen Compounds and Their Mixtures. DTIC Document, 1966.

- [101] J.H. Kuo, H.U. Anderson, D.M. Sparlin. Oxidation-reduction behavior of undoped and Sr-doped LaMnO_3 nonstoichiometry and defect structure, *Journal of Solid State Chemistry* 83 (1989) 52-60.
- [102] J.A.M. Van Roosmalen, E.H.P. Cordfunke. A new defect model to describe the oxygen deficiency in perovskite-type oxides, *Journal of Solid State Chemistry* 93 (1991) 212-219.
- [103] J. Nowotny, M. Rekas. Defect Chemistry of $(\text{La,Sr})\text{MnO}_3$, *Journal of the American Ceramic Society* 81 (1998) 67-80.
- [104] M. Oishi, K. Yashiro, K. Sato, J. Mizusaki, T. Kawada. Oxygen nonstoichiometry and defect structure analysis of B-site mixed perovskite-type oxide $(\text{La, Sr})(\text{Cr, M})\text{O}_{3-\delta}$ ($\text{M}=\text{Ti, Mn and Fe}$), *Journal of Solid State Chemistry* 181 (2008) 3177-3184.
- [105] A.Y. Zuev, D.S. Tsvetkov. Oxygen nonstoichiometry, defect structure and defect-induced expansion of undoped perovskite $\text{LaMnO}_{3+\delta}$, *Solid State Ionics* 181 (2010) 557-563.
- [106] S. Sengodan, J. Kim, J. Shin, G. Kim. Thermodynamic Properties, Defect Analysis, and Electrical Conductivity of the $\text{La}_{0.8}\text{Sr}_{0.2}\text{Sc}_x\text{Mn}_{1-x}\text{O}_{3-\delta}$ Infiltrated into YSZ Scaffolds, *Journal of The Electrochemical Society* 158 (2011) B1373-B1379.
- [107] F.A. Kröger, H.J. Vink. Relations between the Concentrations of Imperfections in Crystalline Solids. in: Frederick S, David T, (Eds.). *Solid State Physics*, vol. Volume 3. Academic Press, 1956. pp. 307-435.
- [108] S. Tanasescu, C. Marinescu, F. Maxim, A. Sofronia, N. Totir. Evaluation of manganese and oxygen content in $\text{La}_{0.7}\text{Sr}_{0.3}\text{MnO}_{3-\delta}$ and correlation with the thermodynamic data, *J Solid State Electrochem* 15 (2011) 189-196.
- [109] S. Tanasescu, F. Maxim, F. Teodorescu, L. Giurgiu. Influence of Composition and Particle Size on Spin Dynamics and Thermodynamic Properties of Magnetoresistive Perovskites, *Journal of Nanoscience and Nanotechnology* 8 (2008) 914-923.
- [110] J.M. Smith, H.C. Van Ness, M.M. Abbott. *Introduction to chemical engineering thermodynamics*. 7th ed., McGraw-Hill, Boston, 2005.
- [111] K. Schwartzwalder, A.V. Somers. Method of making porous ceramic articles. U.S. Patent 3090094, 1963.
- [112] R. Shannon. Revised effective ionic radii and systematic studies of interatomic distances in halides and chalcogenides, *Acta Crystallographica Section A* 32 (1976) 751-767.
- [113] J. Petrasch, P. Coray, A. Meier, M. Brack, P. Häberling, D. Wuillemin, A. Steinfeld. A Novel 50kW 11,000 suns High-Flux Solar Simulator Based on an Array of Xenon Arc Lamps, *Journal of Solar Energy Engineering* 129 (2006) 405-411.
- [114] A. Bonk, A.C. Maier, M.V.F. Schlupp, D. Burnat, A. Remhof, R. Delmelle, A. Steinfeld, U.F. Vogt. The effect of dopants on the redox performance,

microstructure and phase formation of ceria, *Journal of Power Sources* 300 (2015) 261-271.

[115] A. Bonk, A. Remhof, A.C. Maier, M. Trottmann, M.V.F. Schlupp, C. Battaglia, U.F. Vogt. Low-Temperature Reducibility of $MxCe_{1-x}O_2$ ($M = Zr, Hf$) under Hydrogen Atmosphere, *The Journal of Physical Chemistry C* 120 (2016) 118-125.

[116] H. Hayashi, M. Kanoh, C.J. Quan, H. Inaba, S. Wang, M. Dokiya, H. Tagawa. Thermal expansion of Gd-doped ceria and reduced ceria, *Solid State Ionics* 132 (2000) 227-233.

[117] S. Sameshima, T. Ichikawa, M. Kawaminami, Y. Hirata. Thermal and mechanical properties of rare earth-doped ceria ceramics, *Materials Chemistry and Physics* 61 (1999) 31-35.

[118] D. Marrocchelli, S.R. Bishop, H.L. Tuller, B. Yildiz. Understanding Chemical Expansion in Non-Stoichiometric Oxides: Ceria and Zirconia Case Studies, *Advanced Functional Materials* 22 (2012) 1958-1965.

[119] H.-W. Chiang, R.N. Blumenthal, R.A. Fournelle. A high temperature lattice parameter and dilatometer study of the defect structure of nonstoichiometric cerium dioxide, *Solid State Ionics* 66 (1993) 85-95.

[120] G. Brauer, K.A. Gingerich, U. Holtzschmidt. Über die oxyde des cers—IV Die Sauerstoffzersetzungsdrucke im System der Ceroxyde, *Journal of Inorganic and Nuclear Chemistry* 16 (1960) 77-86.

[121] D.-J. Kim. Lattice Parameters, Ionic Conductivities, and Solubility Limits in Fluorite-Structure MO_2 Oxide [$M = Hf^{4+}, Zr^{4+}, Ce^{4+}, Th^{4+}, U^{4+}$] Solid Solutions, *Journal of the American Ceramic Society* 72 (1989) 1415-1421.

Curriculum vitae

Name	Michael Takacs
Nationality	Swiss
Citizen of	Goldach (SG)
Date of birth	March 30, 1988
2013-2016	Doctoral studies, Professorship of Renewable Energy Carries, Department of Mechanical and Process Engineering, ETH Zurich. Supervisor: Prof. Dr. Aldo Steinfeld
2011-2013	Master studies, Institute of Energy Technology, Department of Mechanical and Process Engineering, ETH Zurich
2010	Internship, Elektrizitätswerk der Stadt Zürich (ewz), Sils i.D., Switzerland
2007-2011	Bachelor studies, Department of Mechanical and Process Engineering, ETH Zurich
2007	Eidgenössische Maturität, Kantonsschule Chur, Chur, Switzerland

List of publications

Journal articles

M. Takacs, M. Hoes, M. Caduff, T. Cooper, J.R. Scheffe and A. Steinfeld, “Oxygen nonstoichiometry, defect equilibria, and thermodynamic characterization of LaMnO₃ perovskites with Ca/Sr A-site and Al B-site doping”, *Acta Materialia*, vol. 103, pp. 700-710, 2016

M. Takacs, J.R. Scheffe and A. Steinfeld, “Oxygen nonstoichiometry and thermodynamic characterization of Zr doped ceria in the 1573-1773 K temperature range”, *Physical Chemistry Chemical Physics*, vol. 17, no. 12, pp. 7813-7822, 2015

M. Takacs, S. Ackermann, A. Bonk, M. Neises-von Puttkamer, Ph. Haueter, J.R. Scheffe, U. Vogt and A. Steinfeld, “Splitting CO₂ with a Ceria-Based Redox Cycle in a Solar-Driven Thermogravimetric Analyzer”, *AIChE Journal*, 2016, doi:10.1002/aic.15501

S. Ackermann, M. Takacs, J.R. Scheffe, A. Steinfeld, “Reticulated porous ceria undergoing thermochemical reduction with high-flux irradiation”, *International Journal of Heat and Mass Transfer*, vol. 107, pp. 439-449, 2017

M. Ezbiri, M. Takacs, D. Theiler, R. Michalsky, A. Steinfeld, “Tunable thermodynamic activity of La_xSr_{1-x}Mn_yAl_{1-y}O_{3-δ} (0 ≤ x ≤ 1, 0 ≤ y ≤ 1)

perovskites for solar thermochemical fuel synthesis”, *Journal of Materials Chemistry A*, 2017, doi: 10.1039/c6ta06644e

Conference presentations (oral)

M. Takacs, J.R. Scheffe and A. Steinfeld, “Oxygen Nonstoichiometry and Thermodynamic Characterization of Zr-Doped Ceria at Elevated Temperatures”, *Proceedings of the ASME 9th International Conference on Energy Sustainability*, San Diego, CA, United States, 2015

M. Takacs, M. Hoes, M. Caduff, T. Cooper, J.R. Scheffe and A. Steinfeld, “Oxygen nonstoichiometry and thermodynamic characterization of doped $\text{LaMnO}_{3-\delta}$ perovskites in the 1573 – 1773 K temperature range”, *11th International Conference on Ceramic Materials and Components for Energy and Environmental Applications*, Vancouver BC, Canada, 2015